UNIVERSITY OF MANITOBA

A 3-Degree-of-Freedom Low Power and Large Displacement MEMS Lorentz Force Micro-Mirror

by

Elnaz Afsharipour

A Thesis submitted to the Faculty of Graduate Studies of

The University of Manitoba

in partial fulfillment of the requirements of the degree of

DOCTOR OF PHILOSOPHY

Department of Electrical and Computer Engineering
University of Manitoba
Winnipeg, MB

Copyright © 2019 by Elnaz Afsharipour

Abstract

Optical equipment such as spectrometers, imaging systems, micro-projectors, and optical telecommunication devices often include a mechanically moving mirror to direct light beams. The performance of an optical system can be therefore limited by the mirror's scanning area, its overall size, and power consumption to enable motion. Micro-mirrors moved by MEMS actuators have been developed by various groups to improve the directing of light beams. In this thesis, the development of a micro-mirror that can move and direct a light beam in 3 dimensions is presented. This micro-mirror has a large range of motion and consumes lower electrical power compared to its counterparts.

The micro-mirror presented in this thesis is actuated by electromagnetic force. It is able to tilt about two axes and has linear motion along a third axis. The size of the mirror is 2 mm × 2 mm and the structure is of gimbal-less type. The performance is first evaluated using finite element simulation. After confirming the design, the fabrication process of the structure is explained, followed by experimental testing of static and dynamic responses. In a magnetic field of 0.1 T and by applying 20 mA of current to the actuators (2.6 mW) during resonant operation, the micro-mirror demonstrated a tilt angle of 13.3° at 292.7 Hz about the *x-axis*, and 22.8° at 247.5 Hz about the *y-axis*. With a total dc-drive current of 27.5 mA per actuator, 232-µm linear motion in the *z-axis* direction was achieved. The results are discussed and compared with simulation results. To explain the dynamic behaviour of the system, Lagrange's equations were solved, which described the frequency response of the system. Finally, the performance of the presented micro-mirror was compared with micro-mirrors reported in the other works. It is shown that this micro-mirror has a large range of motion and consumes relatively low electrical power, compared to other works in literature.

In a secondary study, a process for fabricating Distributed Bragg Reflectors (DBR) is presented. The fabrication process includes predicting the required conditions for depositing a thin layer of SiO_x with a specified refractive index by using reactive sputtering technique. Using the developed method, a DBR was fabricated which showed a high reflection of 95% in a wide range of 270 nm bandwidth.

Acknowledgments

I would like to express my sincere gratitude to Dr. Cyrus Shafai for giving me the opportunity to study and work at the University of Manitoba and NSFL (Nano System Fabrication Laboratory). I am sincerely grateful for his continuous support of my Ph.D. study and related research, for his patience, motivation, and immense knowledge. His guidance helped me in all the time of research and writing of this thesis.

I am very grateful to Dr. Arkady Major for his advice, scientific support and sharing his laboratory equipment with us. A special thanks to him for presenting our paper at SPIE conference. I appreciate all the effort that he puts in developing the optics and photonics field.

I would like to acknowledge Dr. Jitendra Paliwal for his advice and also taking time for reviewing my research all through this work.

I would like to thank Dr. Douglas Buchanan and Dr. Sherif Sheriff for their helpful advice and the great courses that they offered. I learned a lot from them. I am also very thankful to Mr. Daniel Card for his kind advice.

My sincere thanks also go to Dwayne Chrusch for teaching me practical skills in the cleanroom. I am very thankful to Glen Kolansky, Ken Biegun, Sinisa Janjic, Mount-First Ng, Guy Jonatschick, Daryl Hamelin and Cory Smit for their technical support. I also thank Amy Dario and Keverly Malawski for their guidance and support.

I would like to express my appreciation to a senior member of our group Dr. Byoungyoul Park for his countless support and advice during my Ph.D. Working and discussing with him was a great chance of learning many skills for me. I also would like to thank my labmates Pawel Glowacki, Sampath Liyanage, Yu Zhou and Meiting Li for supporting my research.

Last but not the least, I would like to thank my family, my husband (Ramin), my mother (Zohreh), my father (Ala), my brother (Adel) and all my friends for their mental and emotional supports and creating many great memories.

This thesis is about directing light. So, it is dedicated to all the people who are inherently working with light. The people, who are light sources, light reflectors, light detectors, and light directors.

Contents

Contents vi

List of Tables x

List of Figures xi

Notations and Abbreviations xv

1 Introduction 1

1.1 MEMS Micro-Mirror Systems 1

1.2 Bragg Mirrors 3

1.3 Research Contributions 4

1.3.1 Three Degree-of-Freedom Micro-Mirror: 4

1.3.2 Bragg reflector technologies: 5

1.3.3 Contributed research publications: 6

1.4 Thesis Overview 9

2 Micro-Mirror Background 10

2.1 Introduction 10

2.2 MEMS Mirror Actuation forces and mechanical structures 12

2.2.1 Electrostatic 12

2.2.2 Piezoelectric 14

2.2.3 Electro-thermal 15

2.2.4 Electromagnetic 16

2.3 Summary and conclusions 19

3 Design of the MEMS Mirror 20

3.1 Introduction 20

3.2 MEMS mirror design and working principle 21

3.2.1 Geometry 21

3.2.2. Actuation Force 24

3.2.3 The orientation of the flexures 26

3.3 Enabling 3 DOF motion 27

3.3.1 Enabling tilt about *x-axis* 28

3.3.2 Enabling tilt about *y-axis* 29

3.3.3 Enabling translational motion in *z-axis* 30
3.4 Lorentz force calculation 31
3.5 Summary and conclusions 31
4 FEM Simulation of the MEMS Mirror 32
4.1 Introduction 33
4.2 Electrical Current Limit Criteria 34
4.2.1 Mirror curvature 34
4.2.2 Electromigration Effect 35
4.3 Displacement and stress simulation 35
4.3.1 Tilt about *y-axis*: 35
4.3.2 Tilt about *x*-axis 37
4.3.3 Translational motion along *z-axis* 39
4.4 Serpentine spring parameters 40
4.4.1 Bending spring constant: 41
4.4.2 Torsional spring constant: 42
4.5 Thermal analysis 43
4.5.1 Joule heating 43
4.5.2 Laser heating 44
4.6 Frequency domain analysis 45
4.7 Summary and conclusions 47
5 Analytical Modeling of the MEMS Mirror 48
5.1 Introduction 48
5.2 Mass-spring model 49
5.2.1 Lumped Element Model 50
5.2.2 Transfer function of the system 51
5.3 Frequency Domain Analysis 52
5.3.1 Euler-Lagrange’s Equation 53
5.3.2 Resonance frequency 56
5.3.3 Mode coupling effect 57
5.4 Summary and conclusions 59
6 Microfabrication 60
6.1 Introduction 60
6.2 Fabrication process 62
6.3 Static deformation of the mirror 74
6.4 Summary and conclusions 74

7 Experiments and Results **75**

7.1 Introduction 75
7.1.1 Variation of the magnetic field 76
7.1.2 Optical angle calculation 77
7.2 Static response 79
7.2.1 Static tilting 80
7.2.2 Step response 82
7.3 Dynamic response 84
7.3.1 Resonance frequency 84
7.3.2 Dynamic deformation of the mirror 88
7.3.3 Mode coupling effect 90
7.3.4 Raster Scan 91
7.4 Comparison with other works 92
7.5 Summary and conclusions 93

8 Fabrication Method for Distributed Bragg Reflectors **95**

8.1 Introduction 95
8.2 Background of depositing materials with a specific refractive index 97
8.3 Experimental details 99
8.4 Statistical model for refractive index determination 103
8.4.1 Surface fitting 104
8.4.2 Implementing the GA 107
8.4.3 Experimental verification of the GA results 111
8.5 Distributed Bragg Reflector 112
8.5.1 DBR background and design 112
8.5.2 DBR fabrication by reactive sputtering of silicon 114
8.6 Summary and conclusions 117

9 Conclusions & Future Work **118**

9.1 Summary 118
9.2 Concluding remarks 120
9.3 Future work 121

Appendices **123**

Appendix 1 - Calculation of the spring constants 124
A.1.1 Calculation of the bending spring constant (k_s and k_m) 124
A.1.2 Calculating Equivalent Young's modulus 125
Appendix 2 - Calculation of moment of inertia (J_s and J_m) 127

A.2.1 Mass moment of inertia of one flexure (J_s) 127
A.2.2 Mass moment of inertia of half-mirror (J_m) 127

Appendix 3 - Calculation of damping coefficient (B) 128

Bibliography 129

List of Tables

Table 2.1: Examples of micro-mirrors actuated by electrostatic force. 13

Table 2.2: Examples of micro-mirrors actuated by piezoelectric force. 14

Table 2.3: Examples of micro-mirrors actuated by electro-thermal force. 16

Table 2.4: Examples of micro-mirrors actuated by electromagnetic force. 19

Table 3.1: geometrical values of the structure. 23

Table 3.2: The enabling of the input voltages needed to generate the *x-axis* tilting shown in Fig. 3.8. 28

Table 3.3: The enabling of the input voltages needed to generate the *y-axis* tilting shown in Fig. 3.9. 29

Table 3.4: The enabling of the input voltages needed to generate the motion shown in Fig. 3.10. 30

Table 4.1: Material properties used for finite element simulation. 33

Table 5.1: Values of the parameters used in the equations of bending and torsional potential energy. 55

Table 6.1: Properties of the deposited aluminum layer. 67

Table 6.2: Anisotropic plasma etching properties used for thinning the silicon wafer. 71

Table 6. 3: Isotropic plasma etching properties used for releasing the silicon wafer. 72

Table 6. 4: properties of oxygen plasma etching process used for etching the thick layer of photoresist. 73

Table 7.1: Comparing the calculated values with the experimentally measured values for the tilt-about-*y-axis* motion. 84

Table 7.2: Mechanical tilt angle and displacement of *y-axis* and *x-axis* tilt motions. 88

Table 7.3: Comparing characteristics of the electromagnetically actuated MEMS mirrors in the literature. 92

Table 8.1: Deposition parameters and measured refractive index of sputtered SiO_x films for 18 different samples. 101

Table 8.2: Coefficients of polynomial of equation (1), found by minimizing the sum of squared errors. 105

Table 8.3: The fitted models using polynomials of various degrees for oxygen partial flow (x) and pressure (y), showing the SSE and R^2. 107

Table 8.4: GA parameters for three population size of 10, 15 and 20, with the objective being an SiO_x film with n = 1.45. 110

Table 8.5: Sputtering parameters and measured refractive index of deposited samples with GA predicted oxygen partial flow and pressure. 112

Table 8.6: Fabrication conditions of the DBR. 115

Table 8.7: Summary of DBR's characteristics fabricated by sputtering method. 116

List of Figures

Fig. 1.1: a) DLP 9000, a commercial device used in display projectors, which works based on tilting of the micro-mirrors. b) A magnified schematic of one micro-mirror. 2
Fig. 1.2: Schematic of a Bragg mirror. 3
Fig. 1.3: Picture of 4 fabricated 3-DOF micro-mirrors. 5
Fig. 2.1: a) A micro-mirror fabricated by Texas instrument. b) An array of micro-mirrors [5]. 11
Fig. 2.2: Schematic of a gimbal-less structure. 15
Fig. 2.3: Schematic of a gimballed structure. 17
Fig. 3.1: a) A 2×2 array of micro-mirrors. b) Picture of one mirror-mirror showing the location of mirror and flexures. 22
Fig. 3.2: Schematic of the current path and terminals. Arrow *B* shows the direction of the magnetic field. 22
Fig. 3.3: Geometry of a serpentine spring. 23
Fig. 3.4: a) Schematic of the micro-mirror. b) Schematic of the four current paths separately. 24
Fig. 3.5: Photo of a micro-mirror with focusing on the wires on a flexure and a mirror corner. 25
Fig. 3.6: Simplified schematic of the initial design of the mirror and flexures. Vector *B* shows the orientation of the magnetic field. a) Current and force directions for the tilting motion about the horizontal axis. b) Current and force directions for the tilting motion about the vertical axis. c) Current and force directions for the translational out-of-plane motion. 26
Fig. 3.7: Simplified schematic of the micro-mirror with flexures 45° angled with respect to the mirror sides. Vector *B* shows the orientation of the magnetic field. a) Current and force directions for the first tilting motion about the dashed-yellow axis. b) Current and force directions for the second tilting motion about the dashed-yellow axis. c) Current and force directions for the translational out-of-plane motion. 27
Fig. 3.8: Schematic of the mirror tilting about *x-axis*; Directions of currents are shown by the red arrows, the direction of magnetic field *B* is shown by the blue arrow, directions of forces are shown by green circles. 28
Fig. 3.9: Schematic of the mirror tilting about *y-axis*; Directions of currents are shown by the red arrows, the direction of the magnetic field *B* is shown by the blue arrow, directions of the forces are shown by green circles. 29

Fig. 3.10: Schematic of the mirror moving in *z-axis*; Directions of current are shown by the red arrows, the direction of the magnetic field *B* is shown by the blue arrow, directions of the forces are shown by green circles. 30
Fig. 4.1: FEM simulation of the optical tilt angle about *y-axis* vs. current. ···· 36
Fig. 4.2: A simulated picture of mirror tilting about *y-axis*.···· 37
Fig. 4.3: FEM simulation of optical tilt angle about *x-axis* vs. current.···· 38
Fig. 4.4: A simulated picture of mirror tilting about *x-axis*.···· 38
Fig. 4.5: FEM simulation of translational motion along *z-axis* vs. current. ···· 39
Fig. 4.6: A simulated picture of mirror moving along *z*-axis.···· 40
Fig. 4.7: Schematic of the structure. a) The blue path shows where the force was applied, and the red arrows show the direction of the force. b) Schematic of a tilted mirror, the deflection of point 1 was measured.···· 41
Fig. 4.8: Schematic of a bent spring. The green arrows show the direction of the force. ···· 42
Fig. 4.9: Closer view of a twisted spring. ···· 43
Fig. 4.10: Temperature rise on the mirror and flexures. ···· 44
Fig. 4.11: Maximum temperature rise on the structure versus applied current···· 44
Fig. 4.12: FEM simulation of the frequency response of the micro-mirror tilting about *x-axis*. ···· 46
Fig. 4.13: FEM simulation of the frequency response of the micro-mirror tilting about *y-axis*. ···· 46
Fig. 4.14: FEM simulation of the frequency response of the micro-mirror moving along *z-axis*. ···· 47
Fig. 5.1: Mass-spring model of the structure. a) The current passing through the flexures and forces on the mirror sides. b) The torque on springs and mirror sides. ···· 49
Fig. 5.2: Equivalent electrical circuit of the structure.....50
Fig. 5.3: Labelling of corners for potential energy. 54
Fig. 5.4: Trajectory of the motion functions derived by solving Lagrange's equations. Mode shapes can be seen in this figure. 58
Fig. 6.1: Fabrication process steps diagram. ···· 62
Fig. 6.2: Cutting lines of a 4-inch wafer. ···· 63
Fig. 6.3: Schematic of the *backside etching* pattern showing the backside opening and alignment marks.65
Fig. 6.4: a) Side view of the etched sample. b) Front view of a back-etched sample.···· 66
Fig. 6.5: The masking pattern of the aluminum wires and mirror.···· 68
Fig. 6.6: Pattern used for covering the flexures and mirror. The red area will remain as part of the final structure.···· 70
Fig. 6.7: Al pattern covered with SPR 220 photoresist.···· 70
Fig. 6. 8: Variation of the thickness of the structure across the springs···· 72

Fig. 6.9: a) Photo of a released sample. b) A sample mounted on a prototype board for testing. 73
Fig. 7.1: Experimental setup used for characterizing the structure. 76
Fig. 7.2: Schematic of a magnet and the mirror on top of it, for calculating the magnetic field strength at different distances from the magnet surface. 77
Fig. 7.3: Schematic of the light beams when the mirror is tilted. 78
Fig. 7.4: Schematic of the setup for measuring the optical tilt angle. 79
Fig. 7.5: Flowchart of actuating the mirror. 79
Fig. 7.6: Schematic of the setup used for generating dc current. 80
Fig. 7.7: Graph of the static optical tilt angle about the *y-axis* vs. applied current. 81
Fig. 7.8: Graph of the static optical tilt angle about the *x-axis* vs. applied current. 81
Fig. 7.9: Graph of the static optical tilt angle along the *z-axis* vs. applied current. 82
Fig. 7.10: Open-loop step response of the tilt about the *y-axis* motion. 83
Fig. 7.11: Block diagram of the experimental setup for measuring the resonance frequency. 85
Fig. 7.12: Frequency response of the tilt about the x-axis motion. The experimental resonance frequency was at 292.7 Hz. 85
Fig. 7.13: Frequency response of the tilt about the y-axis motion. The experimental resonance frequency was at 247.5 Hz. 86
Fig. 7.14: Frequency response of the translational motion along the *z-axis*. The experimental resonance frequency was at 140 Hz. 86
Fig. 7.15: The pattern of the reflected light from the mirror, when the mirror was tilting at its resonance frequency: a) 292.7 Hz for the *x-axis*. b) 247.5 Hz for the *y-axis*. 88
Fig. 7.16: (a) Pattern caused by driving θ_x at its resonance of 292.7 Hz. (b) Pattern caused by driving θ_x at θ_y*'s* resonance of 247.5 Hz. 90
Fig. 7.17: Pattern caused by driving θ_y at 140 Hz. 91
Fig. 7.18: Raster scan pattern generated by vertical axis tilting at 40 Hz and horizontal axis resonating at its resonance frequency 292.7 Hz. 91
Fig. 7.19: Radar plot of the micro-mirrors reported in Table 7.3. 93
Fig. 8.1: Measured refractive index of sputtered SiO_x versus deposition pressure for different oxygen partial flows (O_2/ (O_2+Ar) = 1% to 11%). 102
Fig. 8.2: Measured refractive index of sputtered SiO_x versus oxygen partial flow in three different pressure levels. 103
Fig. 8.3: Plotted fitness function of Equation (8.11). Blue dots show the experimental data points of Table 8.1 106

Fig. 8.4: The Stochastic Universal Sampling technique, for selecting the population members as crossover parents for next generation. 109

Fig. 8.5:a) Genes of all population members at each generation. b) Evolution of fitness value of population members through the generations for the population size of 20. Blue stars show the value of the fitness function of each member, converging to the objective value (red line). 111

Fig. 8.6: Schematic of a distributed Bragg reflector consisting of a quarter-wavelength-thick of high and low refractive index SiO_x layers, λ is the central reflected wavelength. 113

Fig. 8.7: Calculated (dotted) and measured (solid) spectrum of SiO_x DBR. The graph shows a reflectivity of 95 % in reflection-band of more than 270 nm. 115

Notations and Abbreviations

The following notations and abbreviations are used in the thesis:

List	Description
ac	Alternating Current
Al	Aluminum
Ar	Argon
BOE	Buffered Oxide Etchant
dc	Direct Current
DI Water	De-Ionized Water
DSP	Double-side Polished
f	Frequency (Unit: *Hz*)
F	Force (Unit: N)
HMDS	Hexamethyldisilane
HF	Hydrofluoric acid
i	Current (Unit: A)
ICP	Inductively Coupled Plasma
j	Current Density (Unit: A/cm^3)
KOH	Potassium Hydroxide
l	Length
MEMS	Micro-Electro-Mechanical System
N_2	Nitrogen
NSFL	Nano System Fabrication Laboratory
p	Pressure (Unit: Torr)
Poisson's Ratio (ν)	The ratio of lateral strain and axial strain. ν = lateral strain / axial strain (Unitless)
PR	Photoresist
RIE	Reactive Ion Etching
Si	Silicon
SiO_2	Silicon Dioxide
t	Thickness (Unit: μm)
T	Temperature (Unit: K)
Thermal Conductivity	The amount of heat per unit time per unit area that can be conducted through a plate of unit thickness of a given material. (unit = W/m·K)
Ti	Titanium
w	Width
Yield Strength	Maximum stress that can be developed in a material without causing plastic deformation (unit = Pa)
Young's modulus (E)	The ratio of stress and strain in the linear range of the stress and strain curve of the material. E = stress / strain (unit = Pa)

1

Introduction

Contents

1.1 MEMS Micro-Mirror Systems 1
1.2 Bragg Mirrors 3
1.3 Research Contributions 4
1.3.1 Three Degree-of-Freedom Micro-Mirror: 4
1.3.2 Bragg Reflector Technologies: 5
1.3.3 Contributed Research Publications: 6
1.4 Thesis Overview 9

1.1 MEMS Micro-Mirror Systems

A Micro-Electro-Mechanical-System (MEMS) is a mechanical structure on the scale of micrometer. They have been used as sensors by converting a mechanical motion to an electrical signal or as actuators by converting different forms of energy to each other. Some popular examples of MEMS devices include accelerometers [1], gyroscopes [2], pressure sensors [3], and RF switches [4]. Optical MEMS devices like MEMS mirrors are an important type of MEMS devices which have been developed to improve the display technologies in the last 20 years [5]. They have also been used in many other technologies such as medical imaging [6] and 3D printers [7].

A MEMS micro-mirror is a microstructure in which a mirror can tilt or linearly move. The main task of a micro-mirror is to direct a light beam in a specified direction. The beam reflected from the micro-mirror could be used to light up an area, act as a pixel on a screen to make an image or other uses. Micro-mirrors have been used in optical systems including displays or projectors [5], imaging systems [6], sensors [8], and optical telecom [9]. In terms of power consumption and size, micro-mirrors are usually compatible with electronic circuits. This fact along with their high accuracy has attracted a lot of attention. The most popular example of a commercial micro-mirror system is the Digital Light Processors (DLP) produced by Texas Instruments [10]. Fig. 1.1 shows a DLP 9000 which contains more than 4 million mirrors and driving electronics [11]. It is widely used in projector displays.

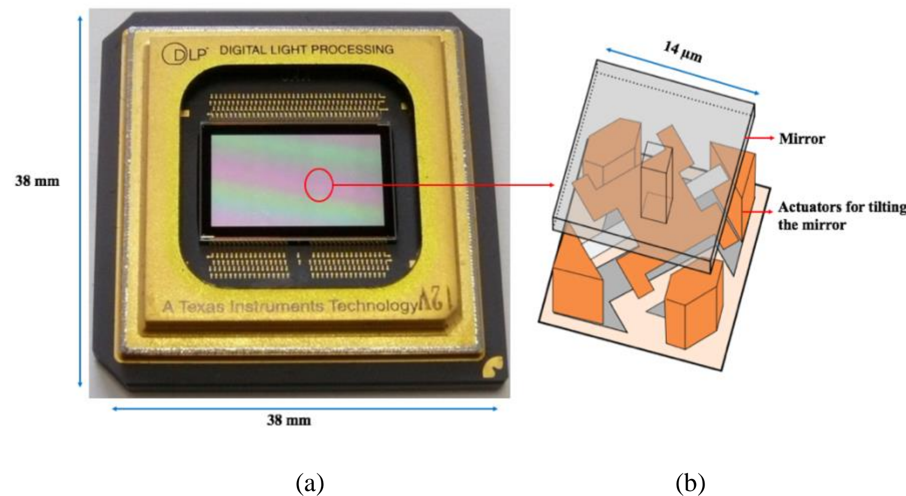

(a) (b)

Fig. 1.1: a) DLP 9000, a commercial device used in display projectors, which are based on tilting of the micro-mirrors. b) A magnified schematic of one micro-mirror.

In some applications of MEMS mirrors, a large tilt angle in various directions is needed. Some examples include medical imaging tools like catheters for Optical Coherence Tomography (OCT) [12, 13], [14, 15] and Michelson interferometer of a Fourier transform microscope [16, 17, 18]. For example, a micro-mirror in an OCT catheter moves around to scan the medium around it. The larger the angle it can move, the wider area will be scanned and more data will be collected. In addition, if the mirror is able to move in various axial directions, horizontal and vertical scanning can also be done. If a curved mirror is

used, there is an opportunity to change the focal length of the mirror using MEMS actuators (varifocal micro-mirrors). This can adjust the imaging resolution at different depths [19]. In the case of Michelson interferometers, a large stroke micro-mirror would enable a more stable splitting ratio over a larger range of wavelengths [17]. Improving the design of micro-mirrors to provide a larger amplitude of motion and to be able to move in various directions while consuming less power, would be valuable for many applications.

1.2 Bragg Mirrors

A Bragg mirror or a Distributed Bragg Reflector (DBR) is basically a mirror that can reflect light in a wide range of wavelengths with a high reflectivity of more than 95%. It consists of a stack of alternating high and low refractive index materials. A schematic of a Bragg mirror is shown in Fig. 1.2. High reflectivity over a wide range of wavelengths has made DBRs an important device in waveguides and laser cavities.

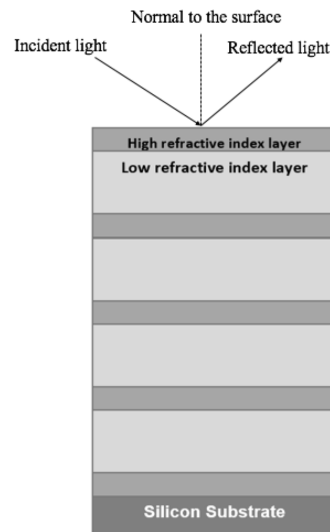

Fig. 1.2: Schematic of a Bragg mirror.

Titanium dioxide (TiO_2) and silicon dioxide (SiO_2) are two common materials which are used for fabricating DBRs [20]. They are usually fabricated using thermal evaporation, sputtering or chemical vapor deposition techniques. The optical thickness of each layer is defined as the multiplication of the layer's

thickness by its refractive index. In regular DBRs, the optical thickness of each layer is equal to a quarter of the central wavelength that is designed to be reflected. This design is usually known as quarter-wave mirror.

1.3 Research Contributions

In this thesis, contributions were made in the areas of micro-mirror technologies (chapters 2-7) and Bragg reflector technologies (chapter 8). Publications were contributed in both areas.

1.3.1 Three Degree-of-Freedom Micro-Mirror:

Micro-mirrors have been reported using different types of actuation and mechanical structures including electrostatic [21], piezoelectric [22], electro-thermal [23, 24] and electromagnetic [25, 26, 27] forces. There are benefits and drawbacks to each type of actuation. Electrostatically actuated MEMS mirrors are commonly designed for high resonance frequency and small footprint, but require a large input voltage for tilting. Piezoelectric-actuated MEMS mirrors are less common due to the complexity in fabricating PZT material, compared to the other types of structures. Electro-thermally actuated micro-mirrors are more often used when multiple directions of motion are needed, however, they suffer from high heat generated on their flexures and large power consumption. Electromagnetic actuators can provide large tilt angles but their motion is usually limited to two directions. This limit comes from the difficulty of aligning the magnetic field orientation with different directions of current. The details of the micro-mirrors actuated by different forces are discussed in Chapter 2.

In this thesis, a micro-mirror is presented which addresses the limitations of other devices. A low voltage electromagnetically actuated micro-mirror with a large range of motion was designed that can move in 3 directions (3 Degree-Of-Freedom, 3-DOF). This micro-mirror is able to work in both static and dynamic modes of motion and can be used in scanning applications. The micro-mirror (shown in Fig. 1.3) is a gimbal-less structure consisting of four serpentine springs connecting a squared shape mirror to the

frame. The micro-mirror uses Lorentz force for actuation and has two tilt modes about the *x-* and *y-axes* and one linear motion in the *z-axis*. An external magnetic field (from a permanent magnet) is aligned to make 45° with all 4 sides of the mirror to equalize the force. Individual control over each side of the mirror is possible which enables the different motions. Experiments showed a tilt angle of 22.8° about the *y-axis* and 13.3° about the *x-axis* while consuming a root-mean-square (RMS) power of 2.6 mW in an external magnetic field of 0.1 T. Vertical motion along the *z-axis* was measured to be 232 μm with 27.5 mA applied to each side of the mirror.

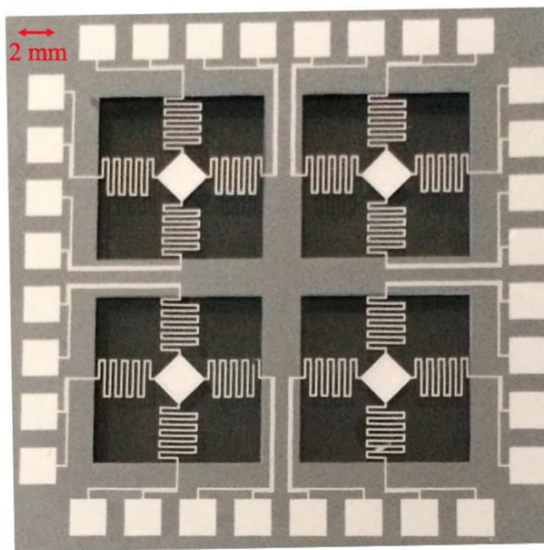

Fig. 1.3: Picture of 4 fabricated 3-DOF micro-mirrors.

1.3.2 Bragg reflector technologies:

Fabricating DBRs requires materials with two different refractive indices. The refractive indices of the DBR's constituent material layers are determining factors in the performance of the DBR [28]. However, since many parameters affect the refractive index of a deposited layer, fabricating materials with specified refractive indices has always been challenging. Co-sputtering [29] and glancing-angle deposition [30] techniques have been employed to deposit materials with different refractive indices. However, they need two or more different material sources (or variable material density) to obtain the two specified refractive

indices needed for the layers in the DBR. In addition, it is very challenging to monitor the refractive index of a layer while it is being deposited. Therefore, developing a method to predict the refractive index of a deposited material can help improve the fabrication of optical devices that need layers with specified refractive indices.

In chapter 8 of this thesis, a method was developed to specifically fabricate thin film materials by reactive sputtering that possess a specified refractive index. The method is based on statistical study and employing a genetic algorithm to calculate the required deposition conditions (pressure and oxygen partial flow) for depositing a film of SiO_x with an arbitrary refractive index. Using this method, layers with specified refractive indices were successfully deposited. This method eliminates the need of employing multiple materials to make layers with different refractive indices. A DBR was fabricated to demonstrate the validity of the method. The DBR showed a high reflection of 95% in a wide range of 270 nm bandwidth.

1.3.3 Contributed research publications:

The above efforts were published in conference proceedings and journals. Below is a summary of the publications of my Ph.D. research.

[Journal Papers]

1. **Elnaz Afsharipour**, Ramin Soltanzadeh, Byoungyoul Park, Dwayne Chrusch, Cyrus Shafai, "Low-power three-degree-of-freedom Lorentz force microelectromechanical system mirror for optical applications," *Journal of Micro/Nanolithography, MEMS, and MOEMS*, 18(1), 015001, pp. 1-11 (2019).

2. **Elnaz Afsharipour**, Byoungyoul Park, and Cyrus Shafai, "Determination of Reactive RF-Sputtering Parameters for Fabrication of SiOx Films Specified Refractive Index, for Highly Reflective SiOx Distributed Bragg Reflector," *IEEE Photonics Journal*, 9(1), pp. 1-16 (2017).

[Conference Proceedings]

3. **Elnaz Afsharipour**, Byoungyoul Park, Ramin Soltanzadeh, and Cyrus Shafai, "An electromagnetically actuated 3-axis gimbal-less micro-mirror for beam steering," *IEEE International Conference on Optical MEMS and Nanophotonics (OMN)*, Lausanne, Switzerland, 2 pages, 29 July - 2 August (2018).

4. **Elnaz Afsharipour**, Byoungyoul Park, Ramin Soltanzadeh, and Cyrus Shafai, "A 3-Degree-of-Freedom MEMS Mirror with Controllable Static and Dynamic Motion for Beam Steering," Eurosensors - European Conference on Solid-State Sensors, Graz, Austria, 4 pages, 9-12 September (2018).

5. **Elnaz Afsharipour**, Byoungyoul Park, and Cyrus Shafai, "Large Tilt Angle Lorentz Force Actuated Micro-Mirror with 3 DOF for Optical Applications," *Eurosensors - European Conference on Solid-State Sensors*, Paris, France, 4 pages, 3-6 September (2017).

6. **Elnaz Afsharipour**, Pawel Glowacki, and Cyrus Shafai, "A MEMS-controllable Fresnel zone plate for miniaturized UV spectrometer," *Eurosensors - European Conference on Solid-State Sensors*, Paris, France, 4 pages, 3-6 September (2017).

The following publications are indirectly related to the topic of this thesis:

[Journal Papers]

7. Byoungyoul Park, **Elnaz Afsharipour**, Dwayne Chrusch, Cyrus Shafai, David Andersen and Greg Burley, "A Low Voltage and Large Stroke Lorentz Force Continuous Deformable Polymer Mirror for Wavefront Control," *Sensors and Actuators A: Physical,* 280, pp. 197-204 (2018).

8. Byoungyoul Park, **Elnaz Afsharipour**, Dwayne Chrusch, Cyrus Shafai, David Andersen and Greg Burley, "Large Displacement Bi-Directional Out-Of-Plane Lorentz Actuator Array for Surface Manipulation," *Journal of Micromechanics and Microengineering*, 27(8), 085005, pp. 1-9 (2017). *Cover Page*

9. Ramin Soltanzadeh, **Elnaz Afsharipour**, Cyrus Shafai, Neda Anssari, Behzad Mansouri, and Zahra Moussavi, "Molybdenum coated SU-8 microneedle electrodes for transcutaneous electrical nerve stimulation," *Biomedical Microdevices*, 20(1), pp. 1-10 (2018).

[Conference Proceedings]

10. **Elnaz Afsharipour**, Cyrus Shafai, "Tailoring the refractive index of ITO thin films by genetic algorithm optimization of the reactive DC-sputtering parameters," In *Oxide-based Materials and Devices VIII*, San Francisco, California, United States, vol. 10105, p. 101050I. International Society for Optics and Photonics, 6 pages, 28 January - 2 February (2017).

11. Byoungyoul Park, **Elnaz Afsharipour**, Dwayne Chrusch, Cyrus Shafai, David Andersen, and Greg Burley, "Aluminum-Polymer Deformable Mirror using Electromagnetic Actuators for Spatial Light Modulation," *IEEE International Conference on Optical MEMS and Nanophotonics (OMN)*, Lausanne, Switzerland, 2 pages, 29 July - 2 August (2018).

12. Byoungyoul Park, **Elnaz Afsharipour**, and Cyrus Shafai, "A Lorentz Force Actuated Continuous Deformable Polymer Mirror for Wavefront Control," *Eurosensors - European Conference on Solid-State Sensors*, Paris, France, 4 pages, 3-6 September (2017).

1.4 Thesis Overview

The thesis is divided into 8 chapters with the following breakdown of topics.

- Chapter 2 presents the background of the research including various technologies employed in building micro-mirrors and their applications.
- Chapter 3 describes the details of the design of the micro-mirror including geometry and actuation force.
- The Finite Element Simulation (FEM) of the device is presented in Chapter 4. The FEM simulation was done to analyze the motion, mechanical stress, thermal stress and frequency response of the system. The results of this chapter were published in the conference proceedings number 5 and 6 of the above list.
- In Chapter 5, the analytical modeling of the micro-mirror including its mass-spring model and frequency domain analysis is described. The results of this chapter were published in the journal paper number 1 of the above list.
- Chapter 6 focuses on the fabrication process of the device. Several fabrication methods were developed and optimized to meet the requirements of the device.
- The development of the experimental setup is described in chapter 7. This chapter includes the experimental test results. The experimental results are discussed and compared with the analytical modeling. The results of this chapter were published in the journal paper number 1 and conference proceedings number 3 and 4 of the above list.
- Chapter 8 presents a method for fabricating Bragg mirrors from reactive sputtering of materials with controlled refractive index. This chapter first introduces the methodology used to determine the process needed to deposit a thin film with a specified refractive index. Then, this method is used to fabricate a Bragg mirror. The results of this chapter were published in the journal paper number 2 of the above list.
- Chapter 9 concludes the thesis by summarizing the work and discussing the contributions.

2

Micro-Mirror Background

Contents

2.1 Introduction 10
2.2 MEMS Mirror Actuation Forces and Mechanical Structures 12
2.2.1 Electrostatic 12
2.2.2 Piezoelectric 14
2.2.3 Electro-thermal 15
2.2.4 Electromagnetic 16
2.3 Summary and Conclusions 19

2.1 Introduction

The first micro-mirror was reported by International Business Machines Corporation (IBM) in 1980 [31]. That primary version of the micro-mirror was designed to reduce the size of devices with movable head structures and make them more compatible with electronic circuits. The development of the micro-mirrors continued and in 1987 Texas Instruments (TI) introduced the first Digital Micro-mirror Device (DMD). The DMD produced by TI included an array of micro-mirrors along with electronic circuits to drive the mirrors. Further development of DMDs along with essential electronics resulted in commercial Digital Light Processors (DLP) in 1996 [10]. Fig. 2.1a shows a schematic of a double electrostatic DMD.

The array of DMDs consisting of many individually controlled mirrors can be seen in Fig. 2.1b. Currently, DMD arrays include up to 8 million micro-mirrors and are available in different display resolutions including 1080p (1920 × 1080) and WQXGA (2560 × 1600) [32]. Each mirror can rotate up to ±17 degrees where the minimum pitch of mirrors is 5.4 μm [33]. Various models can reflect wavelengths from 363 nm to 2500 nm.

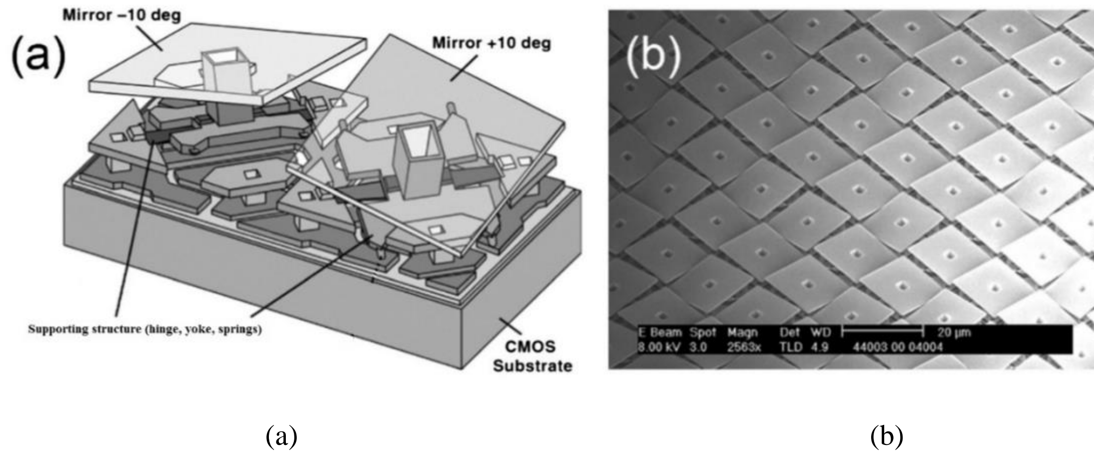

(a) (b)

Fig. 2.1: a) A micro-mirror fabricated by Texas instrument. b) An array of micro-mirrors [5], with the permission of Elsevier.

Characteristics of micro-mirrors depend on the application for which they are designed. For example, a micro-mirror which is designed to be used as part of a display system needs to reflect the light beam in a wide angle. Generally, micro-mirrors are characterized based on their Degree-Of-Freedom (DOF) in motion, the range of displacement, size, response time and power consumption. The performance of each characteristic depends on micro-mirror's intrinsic factors such as mechanical and geometrical properties as well as its extrinsic factors such as actuation and reaction forces. In the following sections, the structure and the mechanism of motion for micro-mirrors are discussed.

2.2 MEMS Mirror Actuation forces and mechanical structures

The four main actuation forces to move micro-mirrors are briefly discussed in the following sections. The common forms of mechanical structures with respect to the type of actuation force are discussed under each topic.

2.2.1 Electrostatic

By applying a potential difference between two electrically conductive plates which are facing each other, the electrostatic force of Equation 2.1 will be generated between them [34]. This force pulls the two plates toward each other.

$$\mathrm{F_{Es}} = \frac{\mathrm{A\varepsilon V^2}}{\mathrm{2d^2}} \tag{2.1}$$

where *V* is the potential difference between the plates, *A* is the area between the plates, *d* is the distance between the plates, and ε is the permittivity or dielectric constant of air which is defined as Equation 2.2:

$$\varepsilon = \varepsilon_0 \times \varepsilon_r = 8.85 \times 10^{-12} \times 1 = 8.85 \times 10^{-12} \frac{F}{m} \tag{2.2}$$

By reducing the gap between the plates, or by increasing the overlap area, a large force can be generated. However, since the dielectric constant of air is small, the generated force and consequently the displacement is usually very small. Therefore, a large input voltage per unit area is required to increase the displacement.

The advantage of electrostatic force is that it works based on static charges and there is no continual current flow, so the power consumption and generated heat is usually not a concern. The most popular example of micro-mirrors actuated by electrostatic force was shown earlier in Fig. 2.1, which was used in Digital Light Processor (DLP) devices produced by Texas Instruments [5].

Electrostatically actuated micro-mirrors have been built in two common structures; parallel plate and comb drive. Parallel plate structures are suitable for bi-stable tilting mirrors like the one shown in Fig 2.1.

While comb drive structures are good for lateral movements. Micro-mirrors with three Degrees of Freedom (DOF) are not very common with this type of actuation. Table 2.1 shows some examples of electrostatically actuated micro-mirrors. Micro-mirrors presented in references [35] and [36] are of 3 DOF, in which tilt angles of 8° and 5.2° are achieved by input voltages of 80 V and 160 V. Other examples can move in two or one dimensions using an average input voltage of 100 V.

Table 2.1: Examples of micro-mirrors actuated by electrostatic force.

Ref. No.	Mirror Size	Actuation	DOF	Optical angle	Voltage/ Power
Yang et al. [35]	500×500×20 μm	ES (PP)	3	8°, 8°, 0.6 μm	80 V
Jung et al. [36]	360 μm (radius)	ES (comb)	3	1.2°, 5.2°, 60 nm	160 V
Ma et al. [5] Texas Instruments [37]	10μm × 10μm	ES (PP)	2	±24°, ±34°	DLP chips power range from 240 mW to 11185 mW for arrays of more than 1 million mirror
Milanovic et al. [38]	600 μm (radius)	ES (comb)	2	20 °	140 V
Aksyuk et al. [39]	500 μm (radius)	ES (PP)	2	±18 °	>150 V
Lin et al. [40]	200 μm (radius)	ES (SDA)	1	45°	±100 V
Li et al. [41]	1.8 mm (radius)	EC (PP)	1	400 μm	80 V
ES: Electrostatic, DOF: Degree of Freedom, PP: Parallel Plate, Comb: Comb drive structure					

In summary, some advantages of electrostatically actuated micro-mirrors include having a small footprint, high resonance frequency, and no heat generation. The disadvantage of this type of actuation is that it needs a relatively large voltage for making a small motion.

2.2.2 Piezoelectric

The piezoelectric property of certain materials is the ability to generate mechanical stress when an electric potential is applied to them. By applying an electric potential, positive and negative charges start to move inside the material. In certain types of crystals that show piezoelectric effect, the movement of charges makes the atoms of the crystal to vibrate back and forth which results in stretching and compressing of the atoms [42]. This property has been used to actuate micro-mirrors. Piezoelectrically actuated micro-mirrors are usually of compact size (compared to the other actuation methods). A piezoelectric thin film can also be used as a position sensor which measures the amount of displacement of the mirror. Piezoelectric actuation is the least popular type of actuation for micro-mirrors since the generated force is low and so is the amplitude of motion. In addition, fabrication of piezoelectric material requires a certain mixture of lead (Pb), zirconate (Z) and titanate (T) known as PZT which is not straightforward in fabrication laboratories. Table 2.2 shows some micro-mirrors actuated by piezoelectric force. A 3-DOF micro-mirror was reported by Maeda et al. [22] which has a 25° for 20 V of input. Other reported micro-mirrors were of one degree of freedom.

Table 2.2: Examples of micro-mirrors actuated by piezoelectric force.

Ref. No.	Mirror Size	Actuation	DOF	Optical angle	Voltage/ power
Maeda et al. [22]	1 mm x 1 mm	PZ	3	25°	20 V
Baran et al. [43]	1.4 mm (radius)	PZ	1	38.5^{o}	24 V, 30 mW
Gu-Stoppel et al. [44]	1 mm x 1 mm	PZ	1	42.5^{o}	7 V
PZ: Piezoelectric, DOF: Degree of Freedom					

In summary, some advantages of piezoelectrically actuated micro-mirrors include having a compact footprint and position sensing. The major disadvantage of this type of actuation is the complexity of fabrication.

2.2.3 Electro-thermal

Thermal expansion effect which is caused by Joule heating of a conductor has been used to actuate micro-mirrors. A very common method for making electro-thermally actuated large tilt angle mirrors is making gimbal-less structures using bimorph flexures. Bimorph flexures are made of two material layers with different thermal conductivity properties [45]. A gimbal-less structure consists of a mirror which is located at the center of the structure and connected to the frame using flexures. Fig. 2.2 shows a simple schematic of a gimbal-less structure. In an electro-thermal actuator, the flexures are made of two materials with different thermal expansion coefficients.

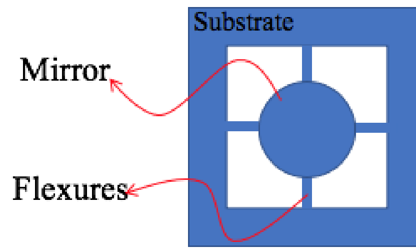

Fig. 2.2: Schematic of a gimbal-less structure.

By making gimbal-less structures with bimorph flexures, large displacement in various directions are possible. Therefore, multi DOF structures are very common with this type of actuation. The major problem with electro-thermal actuators is the large generated heat and the high-temperature rise on the flexures. The power consumption of these actuators is larger than for the other types of actuation. In addition, the direction of motion is not rapidly reversible (compared to the other actuation methods) unless a cooling system is used. The resonance frequency and response time of the system is slower than the other methods.

Electro-thermal actuators have been improved and can possess reduced temperature rise on the flexures. In the actuator reported by Torres et al. [46] the common polysilicon/metal structure of the actuator has been replaced with vanadium dioxide (VO_2). At a certain temperature, a phase transition occurs in VO_2 which changes its physical properties. This method reduced the needed actuation temperature from 300°C to 90°C, potentially making possible temperature-sensitive applications like Optical Coherence

Tomography (OCT) catheters. Some examples of electro-thermally actuated micro-mirrors are presented in Table 2.3. As can be seen, very high tilt angles of about 40° have been reported [23]. However, the power consumption and temperature of the flexures is also high.

Table 2.3: Examples of micro-mirrors actuated by electro-thermal force.

Ref. No.	Mirror Size	Actuation	DOF	Optical angle	Voltage/ power/ temp.
Morrison et al. [23]	400 µm (radius)	ET	3	±40°, 300 µm	90 mW
Xu et al. [13]	400 µm (radius)	ET	2	45°	1.4 V, 25 mA, 90 ℃
Han et al. [47]	1.2 mm x 1.3 mm	ET	2	0.4°, 480 µm	6 V, <270 ℃
Jia et al. [48]	1.5 mm x 1.5 mm	ET	2	±25°, 310 µm	8 V, 240 mW
ET: Electro-thermal, DOF: Degree of Freedom					

In summary, electro-thermal actuators can make a large amplitude of motion in multiple directions. However, they suffer from a high temperature rise on the flexures.

2.2.4 Electromagnetic

An electromagnetic actuator works based on the force applied to a current-carrying wire in a magnetic field. This kind of actuation can generate a large force and so a large displacement. The generated Lorentz force is governed by Equation 2.3:

$$\vec{F} = \vec{I}l \times \vec{B} \tag{2.3}$$

where I is the magnitude of current passing through the wire, l is the length of wire and B is the magnetic flux density. According to Equation 2.3, the strength of the force is a function of magnetic flux density. Therefore, a large force can be produced by consuming a low electrical power. By changing the direction of current with respect to the magnetic field, the direction of force can be changed. The needed magnetic field could be produced by a permanent magnet or by electrical coils.

Multi-DOF micro-mirrors with large amplitude of motion have been reported using electromagnetic actuation. A common method for making electromagnetically actuated multi-DOF micro-mirrors is using

gimballed structures. A gimballed structure is made of two cascaded frames as shown in Fig. 2.3. The internal and external frames enable tilting motions about different axes.

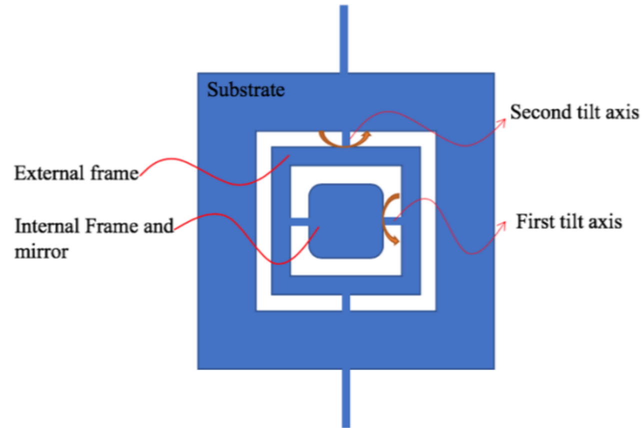

Fig. 2.3: Schematic of a gimballed structure.

According to Equation 2.3, in order to maximize the force, the orientation of the magnetic field with respect to the current must be normal. In a gimballed structure, since the two axes of tiltings are perpendicular to each other, in order to get the maximum force, two perpendicular orientations of the magnetic field are required. Changing the orientation of the magnetic field requires multiple pairs of coils located in different places. For example, a two-DOF micro-mirror with a large tilt angle of 118° was reported by Makishi et al. [49]. This device consisted of a gimballed structure with 4 electromagnets and 4 permanent magnets. This large tilt angle (118°) has been achieved by applying 250 mA of current. The direction of motion was set by configuring the orientation of the magnetic field generated by coils. However, the coils enlarged the final footprint of the structure. Another example of using coils to generate a magnetic field is the micro-mirror reported by Ataman et al. [50] which was able to tilt about two axes for ±16° by consuming 5.1 W. This amount of power is relatively large in electronic devices.

In many cases, a permanent magnet has been employed using the gimballed structure of Fig. 2.3. In the following, some examples of these devices are presented. These works are categorized into two types. The first type of these devices can have multi-dimensional motion in static and dynamic actuations. While the second type can have multi-dimensional motion only in the dynamic actuation. Static actuation is

defined as using a direct current (dc) as input signal of the actuators, and dynamic actuation is defined as using an alternating current (ac) as input signal of the actuators.

Examples of micro-mirrors which can have multi-dimensional motion with both static and dynamic actuations are works done by Cho et al. [26], Makishi et al. [49], Ataman et al. [50] and Ji et al. [51]. Cho et al. [26] reported a gimballed, 3-DOF electromagnetically actuated micro-mirror. This design can tilt up to ±4.2° about the *x-axis* and ±9.2° about the *y-axis* with consuming a power of 345 mW to 360 mW. In this structure, the orientation of the magnetic field was fixed. While this device can move in 3 directions, its power consumption is high. Ji et al. [51] demonstrated a gimballed micro-mirror which can tilt about two axes up to 8.8° about the *x-axis* and 8.3° about the *y-axis* with consuming 16-26 mW of power. This device consumes a lower power, however, it can only move in 2 directions. Raboud et al. [52] reported a device which has a high tilt angle of 25º, however, it moves in only one direction. Devices reported by Makishi et al. [49] and Ataman et al. [50] have been discussed earlier in this section.

The second type of the multi-DOF micro-mirrors can tilt about two axes only by actuating two cascaded perpendicular frames at their resonance (dynamic) mode. These types of micro-mirrors are able to generate patterns of light, but cannot focus the light beam on one spot with a static motion. For example, a large tilt angle gimballed-structure micro-mirror was demonstrated by Yalcinkaya et al. [53] which can tilt up to 53° and 65° in two dimensions only in dynamic mode and by applying 150 mA of current. Other examples of micro-mirrors working only in dynamic mode are works reported by Jeong et al. [54] and Sung et al. [55] which can tilt 30° by consuming 60 mW and 20° by consuming 10 mW of power. The multi-DOF electromagnetically actuated micro-mirrors discussed in this section are summarized in Table 2.4.

In summary, electromagnetically actuated micro-mirrors have been demonstrated to have a large tilt angle in 2 directions, and translation motion in the third dimension. The requirement for a relatively larger package and magnetic field interference are the downsides of electromagnetic actuators.

Table 2.4: Examples of micro-mirrors actuated by electromagnetic force.

Ref. No.	Mirror size	Actuation force	DOF static/ dynamic	Optical tilt angle / displacement	Power / current
Cho et al. [26]	900 µm × 900 µm	EM (MC) B = 0.16 T	3 S-D	±4.2°, ±9.2° z = ±42 µm	345-360 mW
Makishi et al. [49]	8 mm × 4 mm	EM (MM)	2 S-D	118°	250 mA
Ataman et al. [50]	4 mm × 4 mm	EM (MM)	2 S-D	±16°	5.12 W
Ji et al. [51]	1.5 mm (radius)	EM (MC)	22 S-D	8.8°, 8.3° at resonance	16.7-26.3 mW
Yalcinkaya et al. [53]	1.5 mm (radius)	EM (MC)	2 D	65°, 53° at resonance	150 mA
Sung et al. [55]	~ 1 mm (radius)	EM (MM & MC)	2 D	20° at resonance	10 mW
Jeong et al. [54]	3 mm × 1.5 mm	EM (MC)	2 D	30° at resonance	60 mW
Raboud et al. [52]	1 mm × 1 mm	EM (MC)	1 S-D	25° at resonance	10 mW
EM: Electromagnetic, MC: Moving coil, MM: Moving magnet, DOF: Degree of freedom, S: Static, D: Dynamic, frequency, B= Magnetic Field					

2.3 Summary and conclusions

In this chapter, various structures and actuation forces used for building micro-mirrors were investigated and their advantages and disadvantages were discussed. Electromagnetically actuated micro-mirrors were found to have a better performance in terms of amplitude and directions of motion. Designs of the electromagnetically actuated micro-mirrors have evolved toward improving its performance factors.

3

Design of the MEMS Mirror

Contents

3.1 Introduction 20

3.2 MEMS Mirror Design and Working Principle 21

3.2.1 Geometry 21

3.2.2. Actuation Force 24

3.2.3 The Orientation of the Flexures 26

3.3 Enabling 3 DOF Motion 27

3.3.1 Enabling Tilt About the *x-axis* 28

3.3.2 Enabling Tilt About the *y-axis* 29

3.3.3 Enabling Translational Motion along the *z-axis* 30

3.4 Lorentz Force Calculation 31

3.5 Summary and Conclusions 31

3.1 Introduction

The main motivation of this research was to develop a micro-mirror that features:

- Three degrees of freedom in motion

- Large tilt angle and translational displacement
- Low temperature rise
- Low input voltage
- Low power consumption
- Not-complex fabrication process and material

To develop a micro-mirror that possesses all these features, various mechanical, geometrical, electrical and material properties should be considered. In this chapter, first, the geometric design and the actuation force of the structure is explained. Then, the enabling of the three different types of motion is explained.

3.2 MEMS mirror design and working principle

The design of the MEMS mirror requires consideration of its geometry and actuation force which are explained in this section.

3.2.1 Geometry

The overall geometry of the micro-mirror consists of a mirror and 4 flexures as shown in Fig. 3.1. The structure of the micro-mirror developed in this work is of gimbal-less type. In a gimbal-less structure, the mirror is directly connected to a fixed frame using flexures. Fig. 3.1b shows the location of the mirror and flexures.

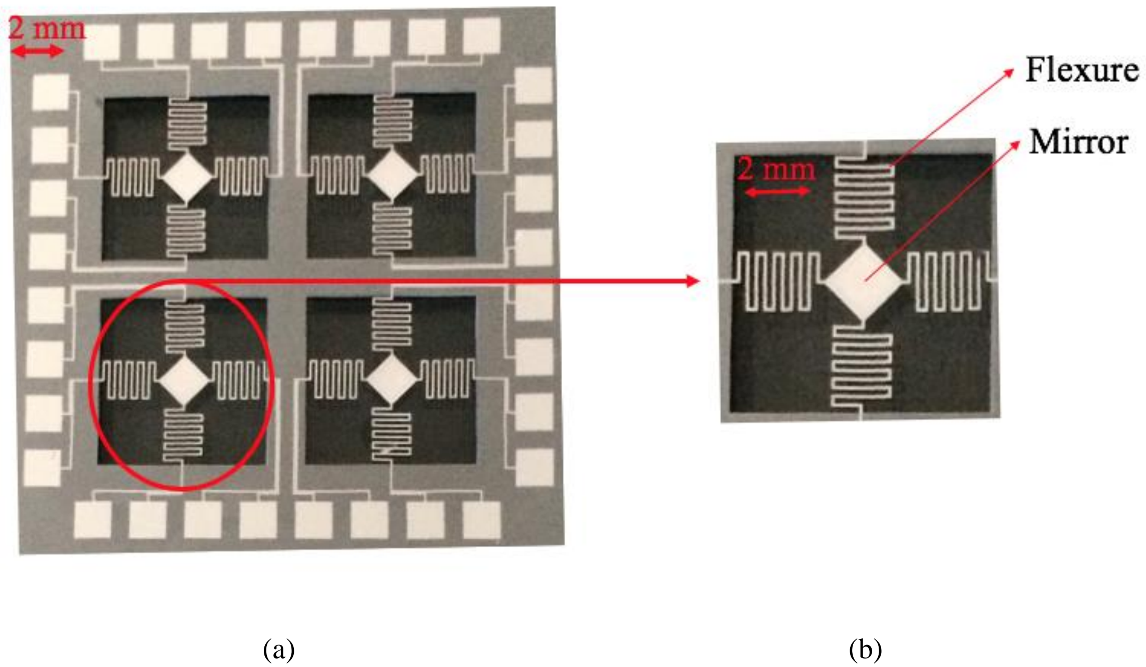

Fig. 3.1: a) A 2×2 array of micro-mirrors. b) Picture of one mirror-mirror showing the location of mirror and flexures.

The mirror is of a square shape geometry and tilts about its two diagonal axes as shown in Fig. 3.2. A square-shape mirror was selected to have the symmetry about the two diagonal axes. The flexures (also called as springs) connect the mirror to a fixed frame. In this structure, the flexures are of serpentine shape.

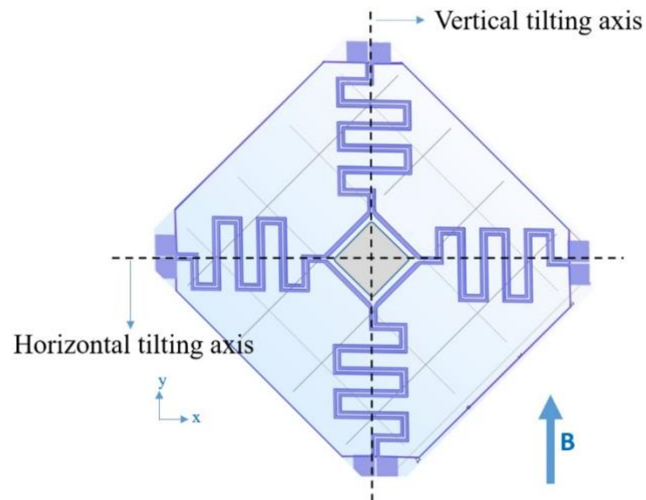

Fig. 3.2: Schematic of the current paths and terminals. Arrow *B* shows the direction of the magnetic field.

The geometrical parameters of the springs were adjusted in the way to get a low spring constant and also low electrical resistivity. Schematic of Fig. 3.3 shows the components of a serpentine spring. The effect of spring parameters on the spring constant and resistivity were studied by running finite element simulations in COMSOL Multiphysics software. The values of the geometrical parameters are presented in Table 3.1. The details of the spring constant of the serpentine spring are discussed further in Appendix A.

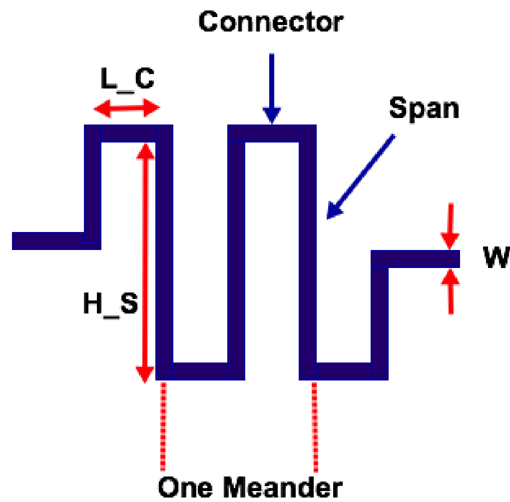

Fig. 3.3: Geometry of a serpentine spring.

Table 3.1: geometrical values of the structure.

Parameter	Value
Mirror	2 mm × 2 mm × 5 µm
Connector length (L_C)	200 µm
Span height (H_S)	2 mm
Width (W) (connector and span)	110 µm
Width of wires	45 µm
Thickness of wires (t)	1.5 µm
Thickness of substrate	5 µm
Number of meanders	4

3.2.2. Actuation Force

Fig. 3.4 shows the schematic of the micro-mirror. A permanent magnet was used to generate an external magnetic field. The magnetic field orientation makes an angle of 45° with all the mirror sides.

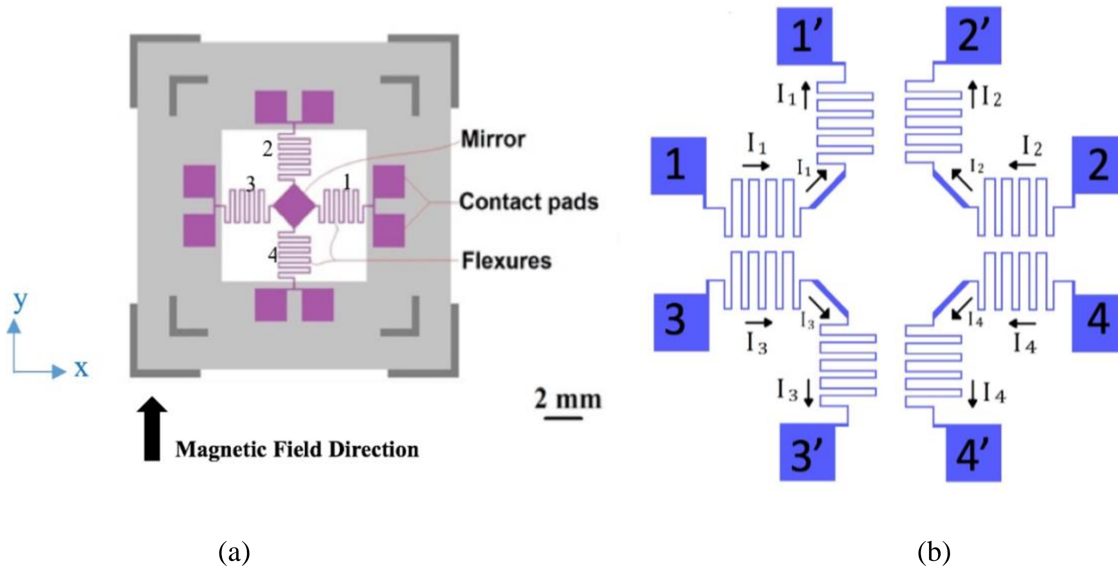

(a) (b)

Fig. 3.4: a) Schematic of the micro-mirror. b) Schematic of the four current paths separately.

There are four sets of wires on one micro-mirror which make the current paths for actuation. Fig. 3.4b shows the schematic of the four current paths separately. Each set is composed of three sections in series, which pass on top of the two springs and one mirror side. Microscopic photo of Fig. 3.5 shows a magnified picture of these wires.

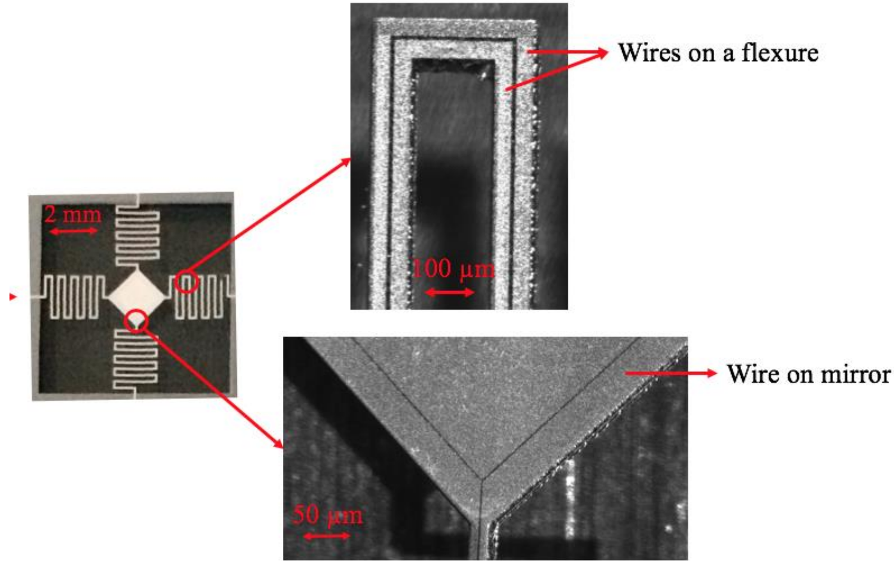

Fig. 3.5: Photo of a micro-mirror with focusing on the wires on a flexure and a mirror corner.

By applying a potential difference between terminals number 1 and 1', current I_1 passes through the springs number 2 and 3 and side 1 of the mirror. In the presence of an external magnetic field, Lorentz force of Equation 3.1 is exerted on the wires [34].

$$\vec{f} = \vec{I}l \times \vec{B} \tag{3.1}$$

where B is the magnetic flux density, l is the length of the wire, I is the current. The direction of the force is determined by the right-hand law. In section 3.3, the enabling of the applied voltages and directions of the forces are shown to achieve different motions.

To calculate the Lorentz force on a wire, we need to know the total effective length of the wire and the magnetic field density at the location of the wire. The electrical currents flowing in the springs number 1 and 3 of Fig. 3.4a are perpendicular to the direction of the magnetic field when it passes through the connectors. The wire conductor on each spring has a path length of 2200 µm. In this work, a permanent magnet was used and the intensity of the magnetic field at the location of the mirror was measured to be 0.1 T.

3.2.3 The orientation of the flexures

The first iteration of the mirror design had the springs parallel to the two sides of the mirror and the direction of the magnetic field was 45° to the mirror sides, as shown in Fig. 3.6. This design was later discarded because of the following reasons. Fig. 3.6a, Fig. 3.6b, and Fig. 3.6c show the direction of current and forces for three motion types. The first motion is tilt about the horizontal axis shown by the yellow line in Fig. 3.6a. As can be seen in Fig. 3.6a, the direction of forces on the springs oppose each other which creates an unwanted twisting motion about the vertical axis. This problem also happens in the third type of motion shown in Fig. 3.6c. Another disadvantage of this design was that the amplitude of motion was very limited due to the large spring constant of the mirror-flexures system.

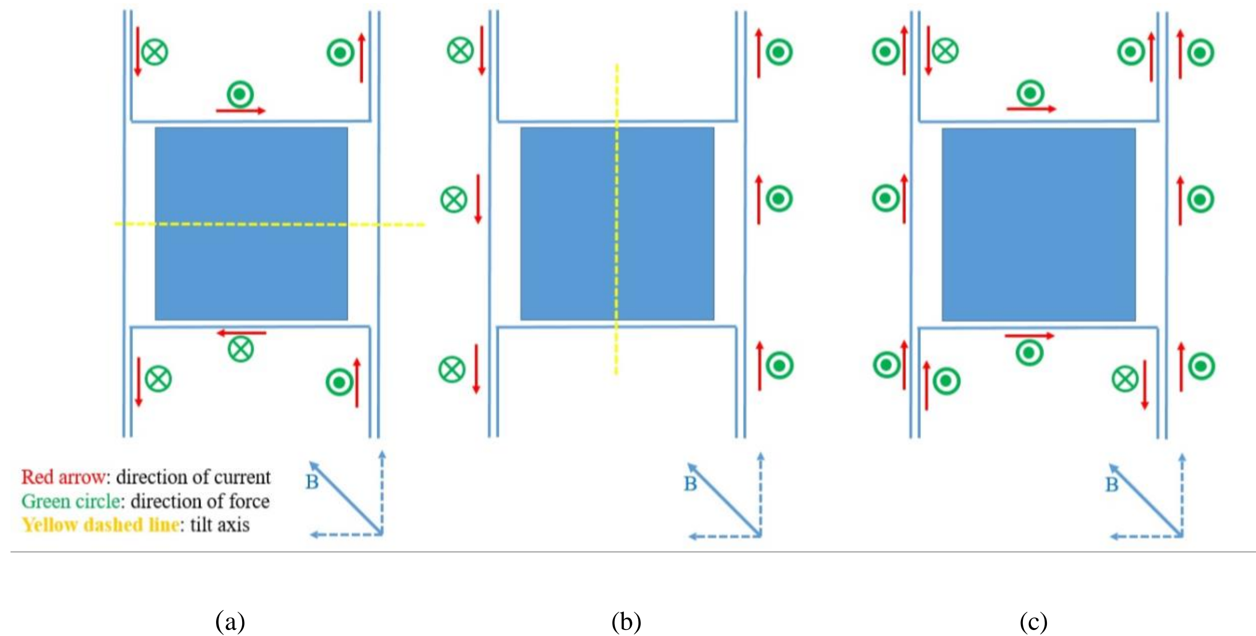

(a) (b) (c)

Fig. 3.6: Simplified schematic of the initial design of the mirror and flexures. Vector *B* shows the orientation of the magnetic field. a) Current and force directions for the tilting motion about the horizontal axis. b) Current and force directions for the tilting motion about the vertical axis. c) Current and force directions for the translational out-of-plane motion.

In order to overcome the twisting motion and displacement problems, the springs were rotated 45°. This geometry is shown in Fig. 3.7 springs number 1 and 2 are perpendicular to the magnetic field and springs number 3 and 4 are parallel to the magnetic field. In the first type of motion shown in Fig. 3.7a, the

twists of the springs number 1 and 2 help tilting about the axis shown by the yellow line. In the second type of motion, the forces on springs number 1 and 2 help amplify the tilting motion. All four sides of the mirror also contribute in the tilting and translational motion. Therefore, this design was considered for development. In the developed structure, the spring bars were replaced with serpentine springs. Compared to a simple bar, a serpentine spring has a lower spring constant, and so is more flexible.

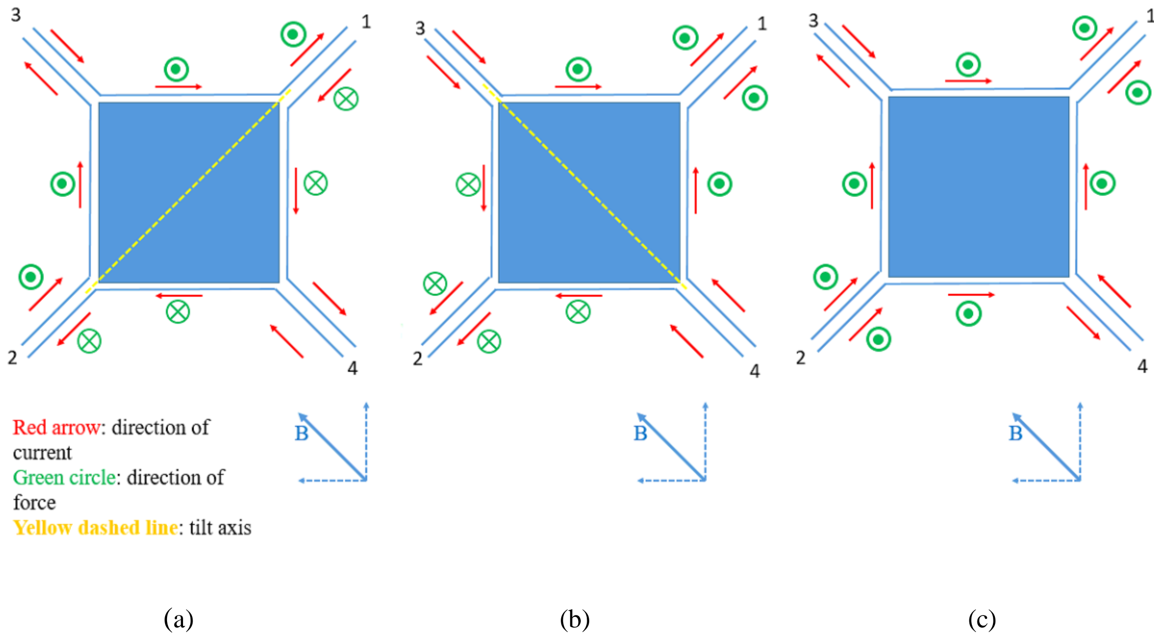

Fig. 3.7: Simplified schematic of the micro-mirror with flexures 45º angled with respect to the mirror sides. Vector *B* shows the orientation of the magnetic field. a) Current and force directions for the first tilting motion about the dashed-yellow axis. b) Current and force directions for the second tilting motion about the dashed-yellow axis. c) Current and force directions for the translational out-of-plane motion.

3.3 Enabling 3 DOF motion

How each motion is achieved depends on the direction of current on the various springs and mirror sides. In the following, the enabling of the three types of motion (tilting about the *x-axis*, tilting about the *y-axis* and translational motion along the *z-axis*) is explained.

3.3.1 Enabling tilt about the *x-axis*

Tilt about the *x-axis* is achieved when two sides of the mirror are lifted up, and the other two sides are dropped down. Fig. 3.8 shows a schematic of the mirror while tilting about the *x-axis*. Red arrows of Fig. 3.8 show the directions of currents which are required to generate this motion. Table 3.2 shows the state of the voltage which should be applied to each terminal of Fig. 3.4b to create the required currents and consequently the proper force. As can be seen the motion of springs connected to 1 and 3, as well as 2 and 4 are in the opposite direction which helps amplify the twisting motion of the springs about the *x-axis*.

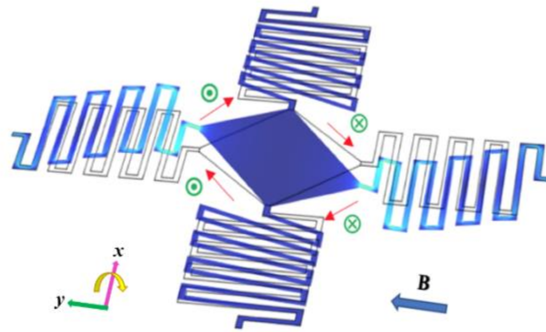

Fig. 3.8: Schematic of the mirror tilting about the *x-axis*; Directions of currents are shown by the red arrows, the direction of magnetic field *B* is shown by the blue arrow, directions of forces are shown by green circles.

Table 3.2: The enabling of the input voltages needed to generate the *x-axis* tilting.

Terminal No.	Voltage	Motion direction of the mirror side between the two corresponding terminals	Motion direction of the spring connected to the corresponding terminal
1	High	Upwards motion	Out-of-Plane
1’	Low		No motion
2	Low	Upwards motion	Out-of-Plane
2’	High		No motion
3	Low	Downwards motion	Inward-Plane
3’	High		No motion
4	High	Downwards motion	Inward-Plane
4’	Low		No motion

3.3.2 Enabling tilt about the *y-axis*

Tilt about the *y-axis* is achieved in a similar way as was explained for the tilting about the *x-axis* motion. Fig. 3.9 shows a schematic of the mirror tilting about the *y-axis*. The directions of currents and forces required to generate this tilting are summarized in Table 3.3. As can be seen the motion of springs connected to 1 and 3, as well as 2 and 4 are in the same direction of each other which helps improve the tilting motion about the *y-axis*.

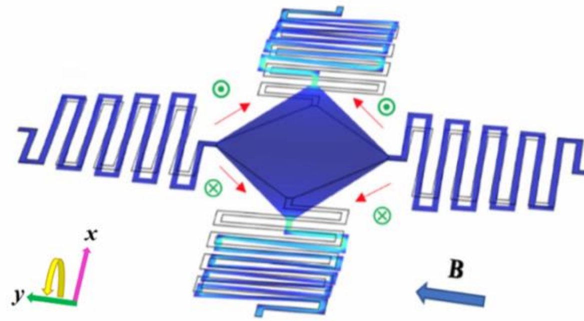

Fig. 3.9: Schematic of the mirror tilting about the *y-axis*; Directions of currents are shown by the red arrows, the direction of the magnetic field *B* is shown by the blue arrow, directions of the forces are shown by green circles.

Table 3.3: The enabling of the input voltages needed to generate the *y-axis* tilting.

Terminal No.	Voltage	Motion direction of the mirror side between the two corresponding terminals	Motion direction of the spring connected to the corresponding terminal
1	High	Upwards motion	Out-of-Plane
1’	Low		No motion
2	High	Downwards motion	Inward-Plane
2’	Low		No motion
3	High	Upwards motion	Out-of-Plane
3’	Low		No motion
4	High	Downwards motion	Inward-Plane
4’	Low		No motion

3.3.3 Enabling translational motion in the *z-axis*

When all the four sides of the mirror move in the same direction, a translational motion in the *z-axis* is generated. Fig. 3.10 shows a schematic of the mirror moving upward along the *z-axis*. This motion can be upward or downward along the *z-axis*. The needed current directions and forces are presented in Table 3.4. In this motion, the force is generated on all the 4 sides of the mirror and also the springs connected to the flexures 1', 2', 3' and 4', therefore this motion has a large amplitude.

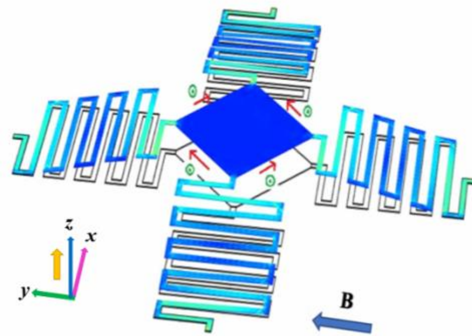

Fig. 3.10: Schematic of the mirror moving along the *z-axis*; Directions of current are shown by the red arrows, the direction of the magnetic field *B* is shown by the blue arrow, directions of the forces are shown by green circles.

Table 3.4: The enabling of the input voltages needed to generate the motion shown in Fig. 3.10.

Terminal No.	Voltage	Motion direction of the mirror side between the two corresponding terminals	Motion direction of the spring connected to the corresponding terminal
1	High	Upwards motion	Out-of-Plane
1'	Low		No motion
2	Low	Upwards motion	Out-of-Plane
2'	High		No motion
3	High	Upwards motion	Out-of-Plane
3'	Low		No motion
4	Low	Upwards motion	Out-of-Plane
4'	High		No motion

3.4 Lorentz force calculation

Using Equation 3.1, the force on the mirror system can be calculated. The magnetic field measured at the mirror due to the permanent magnets was 0.1 T. The sides of the mirror are oriented at 45° to the field. Flexures 1 and 2 are perpendicular to the field, while 3 and 4 are parallel to the field. For example, assuming a current of 20 mA on flexure 1, the Lorentz force on one spring would be:

$$\vec{f} = \vec{I}l \times \vec{B} = 20\ mA \times 2200\ \mu m \times 0.1\ T = 4.4\ \mu N$$

On the mirror side, the Lorentz force would be:

$$\vec{f} = \vec{I}l \times \vec{B} = 20\ mA \times 2000\ \mu m \times 0.1\ T \times \sin 45° = 2.8\ \mu N$$

Therefore, the amplitude of current determines the strength of the Lorentz force which then determines the displacement of the mirror.

3.5 Summary and conclusions

In this chapter, the geometry of the micro-mirror and the orientation of the flexures and the magnetic field were explained. The enabling of the three types of motion was explained and the amount of Lorentz force on one spring and the mirror side was calculated. Therefore, in the following chapters, where a specific type of motion is meant to be enabled, the settings of section 3.3 are used.

4

FEM Simulation of the MEMS Mirror

Contents

4.1 Introduction 33

4.2 Electrical Current Limit Criteria 34
4.2.1 Mirror Curvature 34
4.2.2 Electromigration Effect 35

4.3 Displacement and Stress Simulation 35
4.3.1 Tilt About the *y-axis*: 35
4.3.2 Tilt About the *x*-axis 37
4.3.3 Translational Motion Along the *z-axis* 39

4.4 Serpentine Spring Parameters 40
4.4.1 Bending Spring Constant: 41
4.4.2 Torsional Spring Constant: 42

4.5 Thermal Analysis 43
4.5.1 Joule Heating 43
4.5.2 Laser Heating 44

4.6 Frequency Domain Analysis 45

4.7 Summary and Conclusions 47

4.1 Introduction

The micro-mirror was simulated using COMSOL Multiphysics software. The purpose of simulation was to verify the presented model and to find the value of some parameters needed for modeling. COMSOL software includes many physics and Multiphysics modules, which makes it easy to work with multiple physics concepts at one time. It provides a user-friendly CAD environment and a variety of materials and meshing methods.

COMSOL breaks down a problem into smaller parts called finite elements. Then, the partial differential equations that describe the environment are solved for all the elements. These equations are all assembled together to form a large set of equations that model the entire geometry. The large set of equations are then numerically solved by iteration toward minimizing a converging error function [56].

The following steps were taken for running the simulations of the micro-mirror. First, the geometry of the structure was drawn in the CAD environment of the COMSOL software and the variables and functions were defined. Silicon was assigned to the substrate layer and aluminum was assigned to the mirror and wires. The substrate layer and wires were separated using a layer of silicon dioxide. Table 4.1 shows the properties of the material used for simulation.

Table 4.1: Material properties used for finite element simulation.

	Density (kg/m^3)	Young's modulus (Pa)	Poisson's ratio	Layer thickness
Aluminum	2700	70×10^9	0.33	1.5 (μm)
Silicon dioxide	2200	70×10^9	0.17	0.1 (μm)
Silicon	2329	170×10^9	0.28	5 (μm)

The four physics modules added to the project were *Magnetic Fields, Electric Currents, Solid Mechanic,* and *Heat Transfer in Solids*. A fine mesh was then created for the structure. Finally, a *stationary* study and a *Frequency Domain* study were performed to analyze the model.

The amplitude of the background magnetic field was set to be 0.1 T and a current of 1 mA to 20 mA was applied to the terminals. 20 mA is approximately the maximum current that could be applied to the actuators, and this is discussed in section 4.2. The Lorentz force generated by the corresponding input current was calculated and applied on the springs and mirror sides by the software.

The first study that was run was to explore the mechanical tilt angle of the mirror and mechanical stress on the structure. The second study was to find the spring constant of the serpentine spring. A thermal analysis was done to investigate the temperature rise on the flexures. Finally, a frequency domain analysis was run to explore the frequency response of the system and calculate the resonance frequency.

4.2 Electrical Current Limit Criteria

Throughout the simulations and the experiments, the electrical current is limited to a maximum of 20 mA. In this section, the reason of this limit is explained. There are two factors that limit the maximum current passing through the wires. The first factor is the thermal stress on the mirror and the second factor is electromigration effect. These factors are discussed below.

4.2.1 Mirror curvature

The generated heat or temperature rise on the mirror can cause a curvature on the mirror. With a 20 mA of input current, the temperature rise is ~7.7 °C. This causes a deformation of ~22 µm on the mirror which is equal to ~0.8% of the mirror size or a Radius of Curvature (ROC) of 4.5 cm. In most of the experiments, the input current was stopped at 20 mA to keep the mirror curvature below 1% of the mirror size.

4.2.2 Electromigration Effect

Electromigration is another factor that limits the input current. When electrons move in a conductor, some momentum is transferred to metal atoms that can gradually move them. Over time this can deform the conductor [57]. To avoid electromigration effect, the current density must be lower than the electromigration limit, which is 10^5 A/cm^2 for aluminum wires. Using the dimensions of the conductor wires as given in Table 3.1, the maximum current was calculated to be:

$$J_{max} = \frac{I_{max}}{crosssection\ area} = \frac{I_{max}}{w*t} \tag{4.1}$$

$$J_{max} \times w \times t = I_{max}$$

$$10^5 \left(\frac{A}{cm^2}\right) \times 45 \times 10^{-4}(cm) \times 1.5 \times 10^{-4}(cm) = 67.5\ mA$$

Therefore, an applied current of 20 mA was selected to be well below the electromigration limit which is 67.5 mA.

4.3 Displacement and stress simulation

To simulate the motion of the mirror, the voltage settings which were explained in chapter 3 were applied to the terminals of the micro-mirror. Individual simulations were done to analyze different types of motions.

4.3.1 Tilt about the *y-axis*:

By sweeping the input dc current between 1 mA to 20 mA on the appropriate flexure conductors (as given in Table 3.3), the optical *y-axis* tilt angle of the mirror was calculated. The graph of optical tilt angle vs. current is shown in Fig. 4.1. An input current of 20 mA resulted in 11° tilting about the *y-axis*.

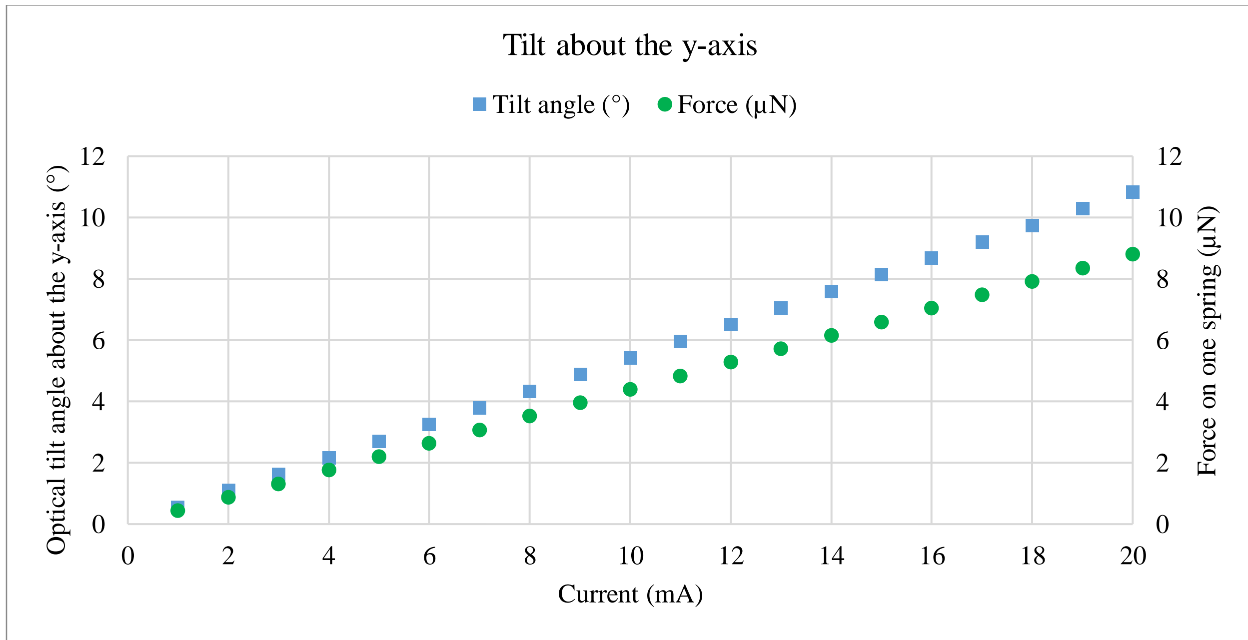

Fig. 4.1: FEM simulation of the optical tilt angle about the *y-axis* vs. current.

The color diagram of Fig. 4.2 demonstrates the stress on the structure. The maximum stress can be found at the location where the spring connects to the frame. The maximum stress value for an input current of 20 mA, which makes a tilt angle of 11°, was 2.17 MPa. To prevent the failure of the structure, the maximum stress should not exceed the yield stress of the material. The yield stress of a material is the amount of stress at which the material permanently deforms. The yield stress of silicon at 20°C is 3.8 GPa. Therefore, the structure can operate without failure, since 2.17 MPa is much lower than the yield stress.

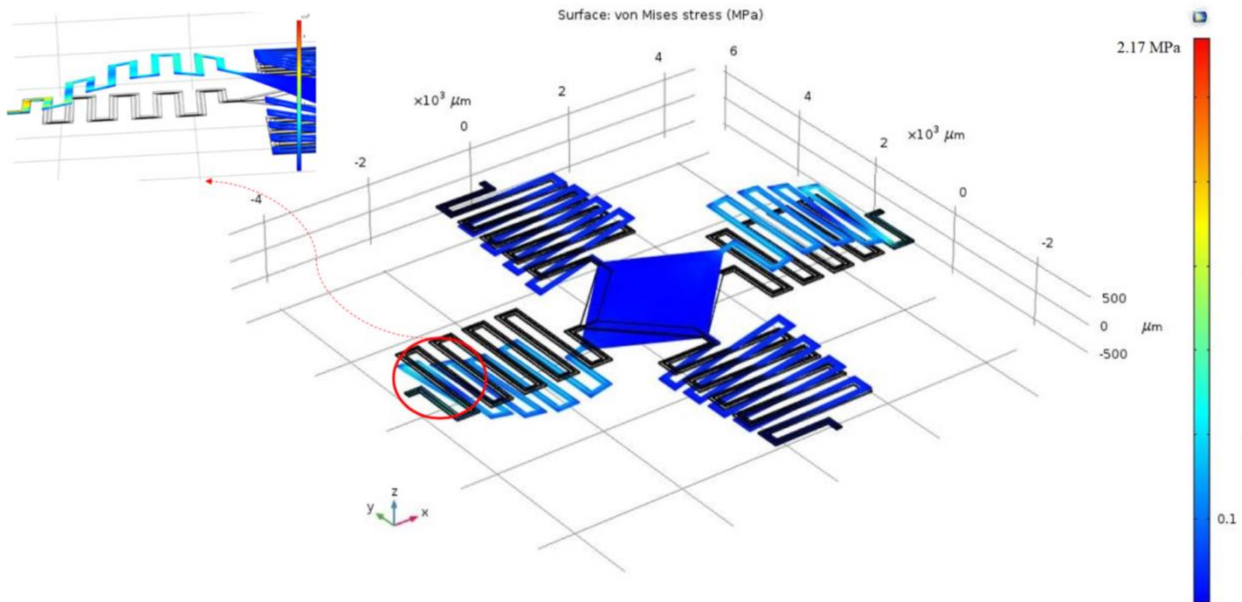

Fig. 4.2: A simulated picture of mirror tilting about the *y-axis*.

4.3.2 Tilt about the *x*-axis

By sweeping the input dc current between 1 mA to 20 mA on the appropriate flexure conductors (as given in Table 3.2), the optical *x-axis* tilt angle of the mirror was calculated. The graph of optical tilt angle vs. current is shown in Fig. 4.3. An input current of 20 mA resulted in 5.6° tilting about the *x-axis*. The color diagram of Fig. 4.4 demonstrates the stress on the structure, and the maximum stress value for a tilt angle of 5.6° was 0.33 MPa.

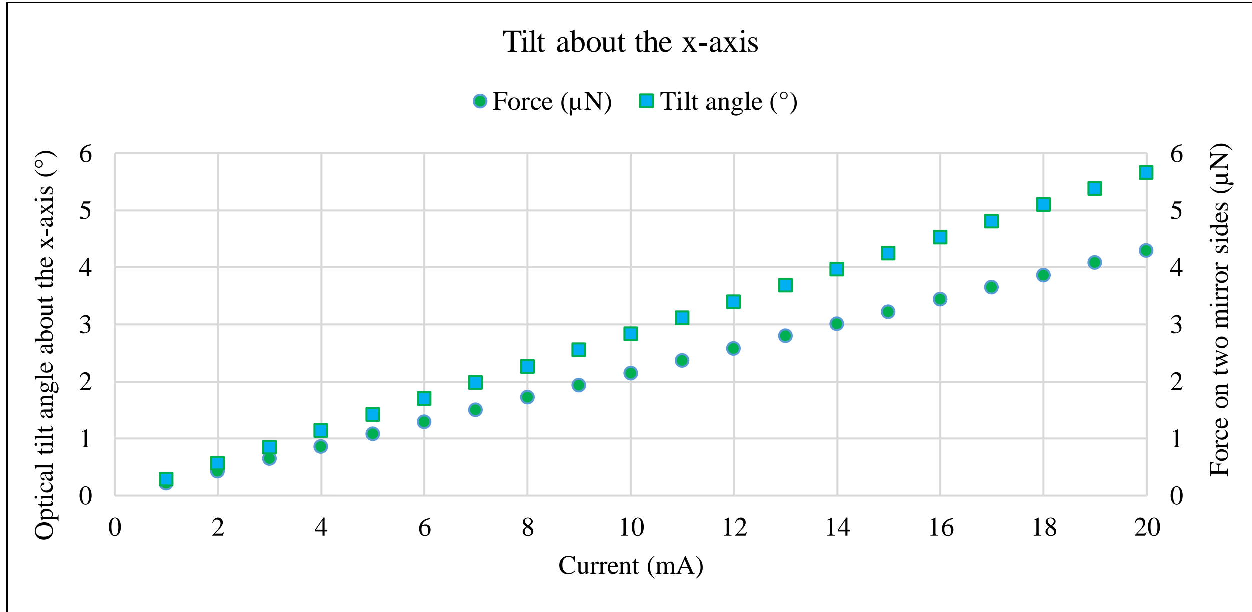

Fig. 4.3: FEM simulation of optical tilt angle about the *x-axis* vs. current.

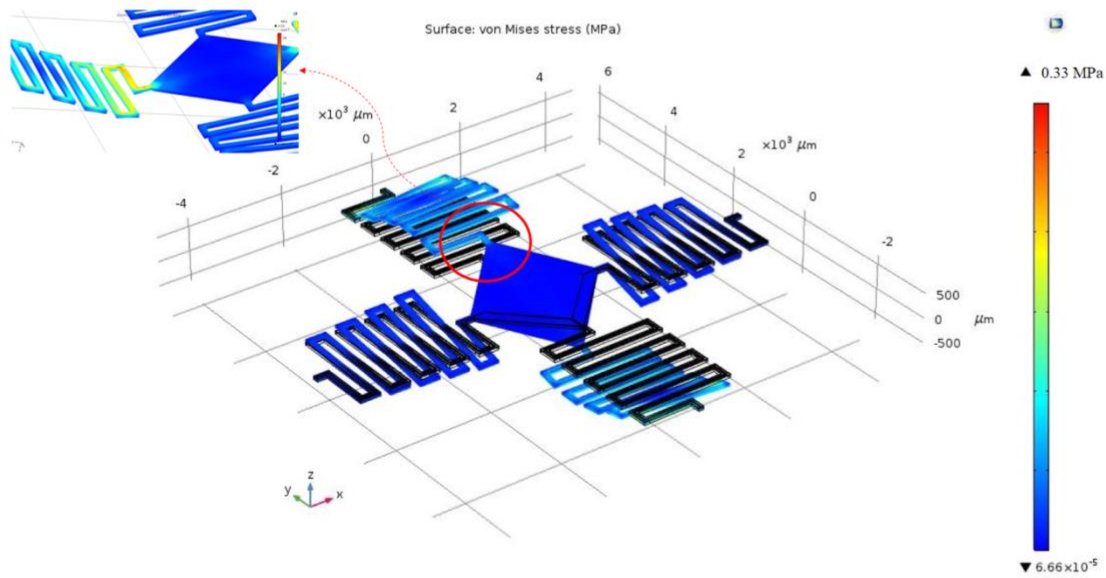

Fig. 4.4: A simulated picture of mirror tilting about the *x-axis*.

4.3.3 Translational motion along the *z-axis*

Setting of Table 3.4 was set to simulate the mechanical angle when the micro-mirror is moving in the *z-axis*. By sweeping the input dc current between 1 mA to 20 mA, the linear motion of the mirror along the *z-axis* was calculated. The graph of linear translation vs. current is shown in Fig. 4.5. For an input current of 20 mA, the displacement was 25 µm. A linear relationship between the tilt angle and the input current can be seen in the graph. The color diagram of Fig. 4.6 demonstrates the stress on the structure, and the stress value for a translational motion of 25 µm was 2.8 MPa.

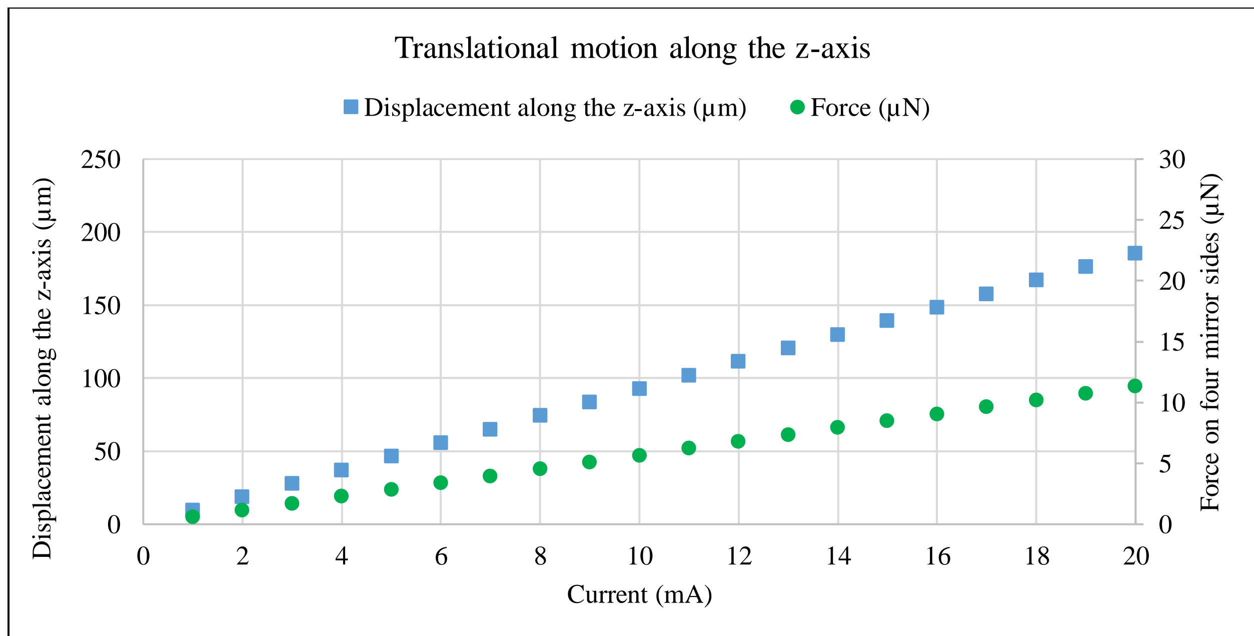

Fig. 4.5: FEM simulation of translational motion along the *z-axis* vs. current.

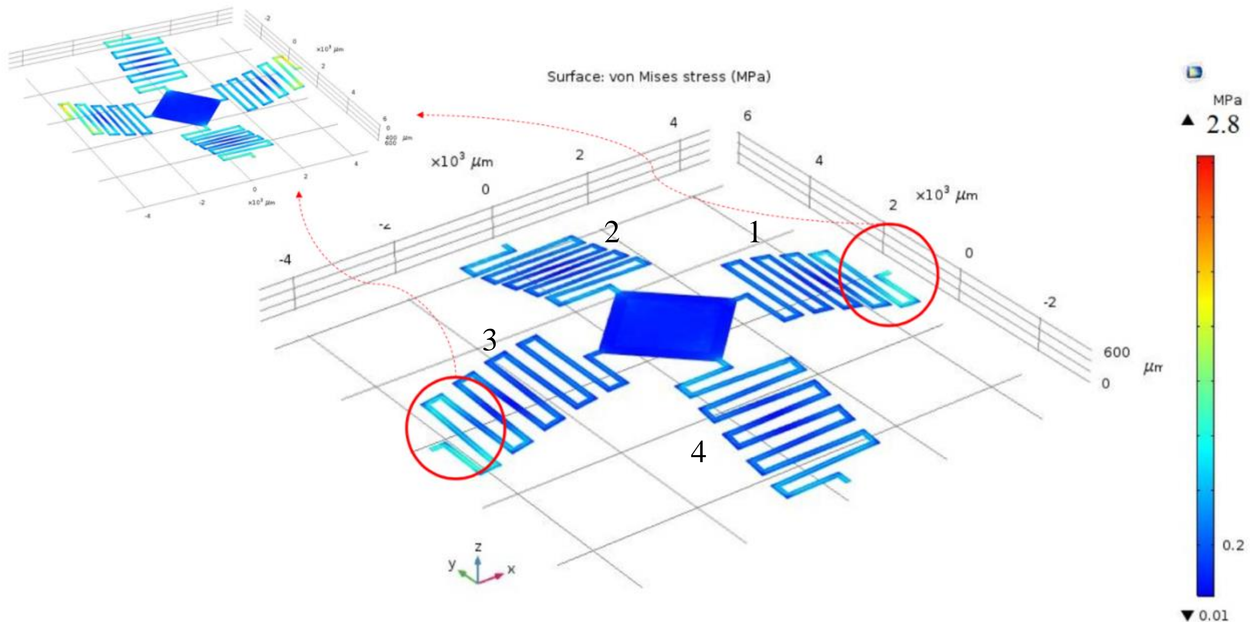

Fig. 4.6: A simulated picture of mirror moving along the *z-axis*.

When the mirror is translating along the *z-axis*, the Lorentz force exerts on all the four sides of the mirror and springs number 1 and 3. Since, there is no force on springs number 2 and 4, the corners connected to these two springs have a reduced motion. This fact can induce a tilting motion to the translational motion. In order to calculate the amount of this tilting, the displacement of the four corners and the center of the mirror were calculated using simulation. The displacements equaled less than 1° of tilting motion.

4.4 Serpentine spring parameters

Spring constant is defined as the resistivity of a spring to moving in a certain direction. It is calculated by the division of force to the displacement in the direction of the force. Spring constant is a determinative factor in static and dynamic motions and the resonance frequency of the system. Therefore, the spring constant of the flexures were found by finite element simulation method in COMSOL software using the *Solid Mechanics* physics and a *Stationary* study. In this structure, the springs have two types of displacement; bending and torsion. Simulation of the bending and torsional spring constants are described

below. The model includes the entire mirror and spring structure with geometrical dimensions matching the fabricated device and material properties shown earlier in Table 4.1.

4.4.1 Bending spring constant:

A load force equal to the Lorentz force created by 20 mA of current and 0.1 T magnetic field was applied on the spring and mirror sides as shown in Fig. 4.7a. The deflection angle was measured at the corner of the mirror shown by point 1 in Fig. 4.7b.

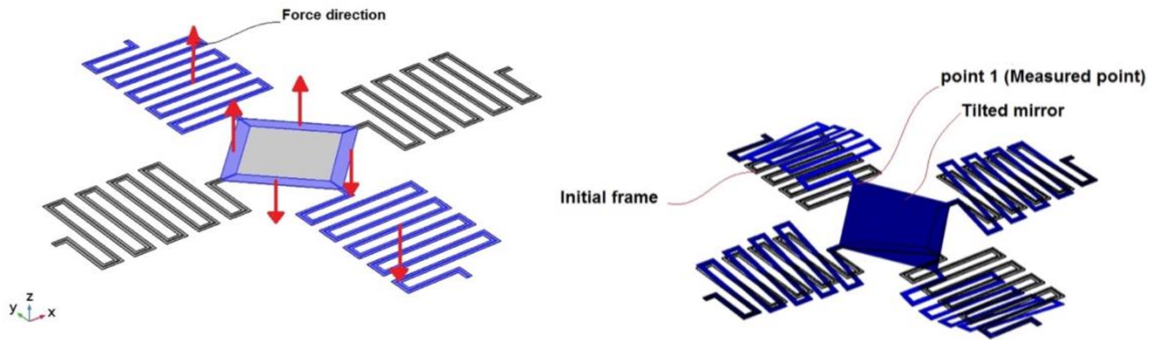

Fig. 4.7: Schematic of the structure. a) The blue path shows where the force was applied, and the red arrows show the direction of the force. b) Schematic of a tilted mirror, the deflection of point 1 was measured.

The bending spring constant at point 1 was calculated by dividing the applied torque to the deflection angle:

$$k_{my-\theta y} = k_{mx-\theta x} = \frac{F \cdot d}{\theta} = \frac{10\times10^{-6}(N)\cdot 3.3\ (mm)}{0.17\ (rad)} = 1.9 \times 10^{-4}\ (\frac{N\cdot m}{rad}) \tag{4.2}$$

In order to calculate the spring constant of the mirror in the z direction, a force (F) was applied in the direction of the *z-axis* to the wires on top of the spring. The angle of rotation (θ) and the *z-axis* displacement (u_z) were measured. Fig. 4.8 shows a closer view of a spring when bending up, as a result of applying a force in the z direction.

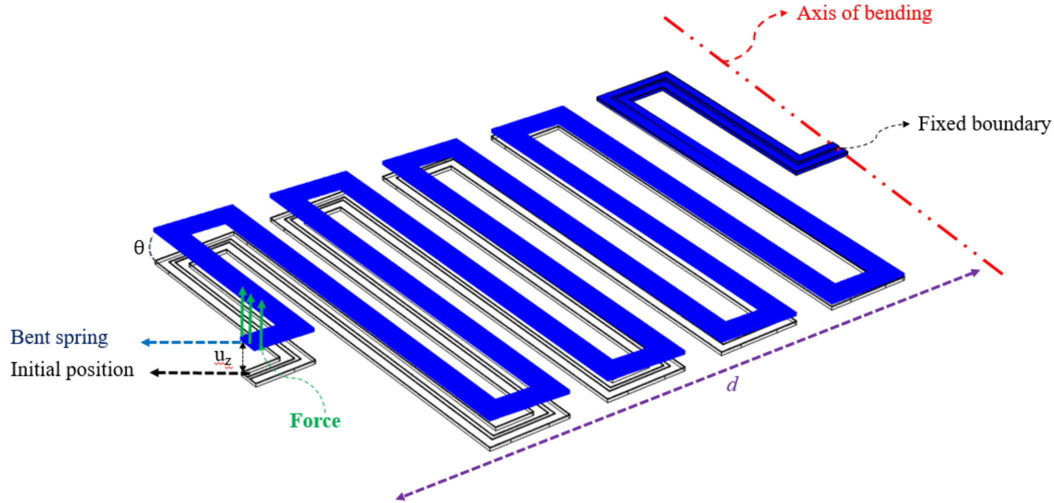

Fig. 4.8: Schematic of a bent spring. The green arrows show the direction of the force.

The spring constant in *z* direction, when a force in *z-axis* is applied to the spring is calculated to be:

$$K_{fz-uz} = \frac{F}{u_z} = \frac{10\times10^{-6}\,(N)}{166.6\,(\mu m)} = 0.06\,\left(\frac{N}{m}\right) \tag{4.3}$$

A force applied in *z*-direction also makes a bending motion about *x*- or *y-axis*. The bending spring constant of the mirror caused by a force in *z* direction is calculated to be:

$$K_{fz-\theta x} = k_{fz-\theta y} = \frac{F}{\theta} = \frac{10\times10^{-6}\,(N)}{0.12\,(rad)} = 8.2\ \times 10^{-5}\,(\frac{N}{rad}) \tag{4.4}$$

The spring constant values calculated in this section, are used in finding the transfer function and modal analysis of the micro-mirror which are reported in chapter 5.

4.4.2 Torsional spring constant:

Fig. 4.9 shows the close-view schematic of a twisted spring. A force (*F*) was applied on the wires in the *z-axis*. The force applied on the left side of the spring was in the positive direction of the *z-axis* and the force applied on the right side of the spring was in the negative direction of the *z-axis*. The twisting angle (θ) was measured and the torsional spring constant was calculated to be:

$$k_{torsional} = \frac{F\cdot d}{\theta} = 2.6\times 10^{-8}\,(\frac{N\cdot m}{rad}) \tag{4.5}$$

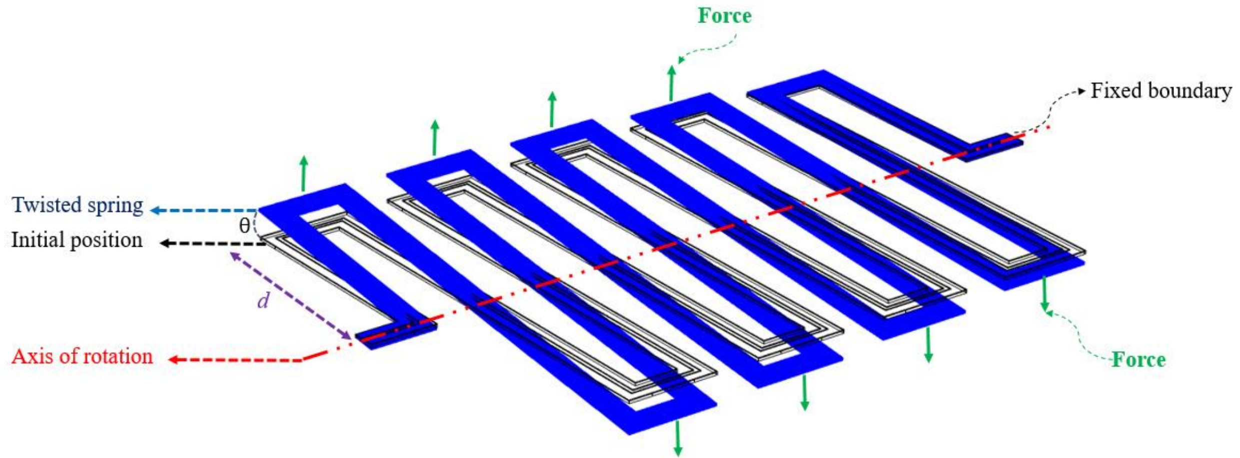

Fig. 4.9: Closer view of a twisted spring.

4.5 Thermal analysis

There are two sources of heat in this system. First, the heat generated by the current passing through the wires. Second, the heat generated by the laser shining onto the mirror. In the following discussion the effects of these two heat sources are calculated.

4.5.1 Joule heating

A current passing through the wires heats up the conductor. To measure the temperature rise on the wires, a FEM simulation was done using *Solid mechanics*, *Heat transfer in solids* and *Electric currents* physics. The colour graph of Fig. 4.10 shows the temperature rise on the structure. For this simulation, an electric current sweep from 0-20 mA was sent through all the wire paths (4 in total) to simulate maximum heating. The room temperature was set equal to 20 °C. The maximum temperature on the mirror was found to be 27.7°C which is equal to 7.7°C temperature rise on the mirror. This causes a curvature with a radius of 4.5 cm. The graph of Fig. 4.11 shows the maximum temperature rise versus applied current to the terminals.

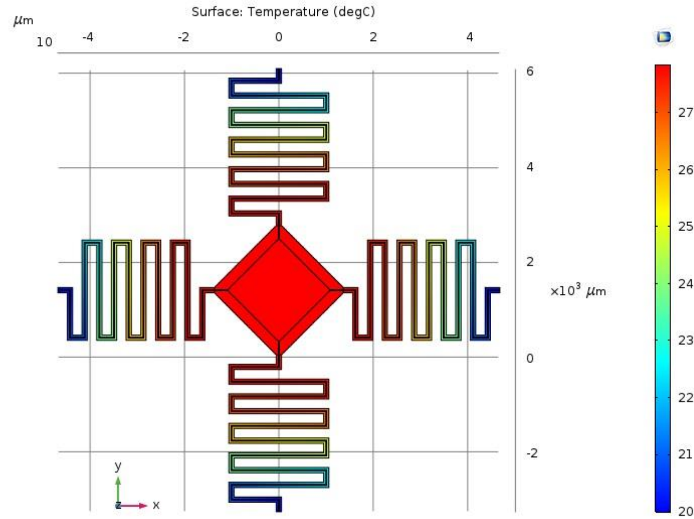

Fig. 4.10: Temperature rise on the mirror and flexures.

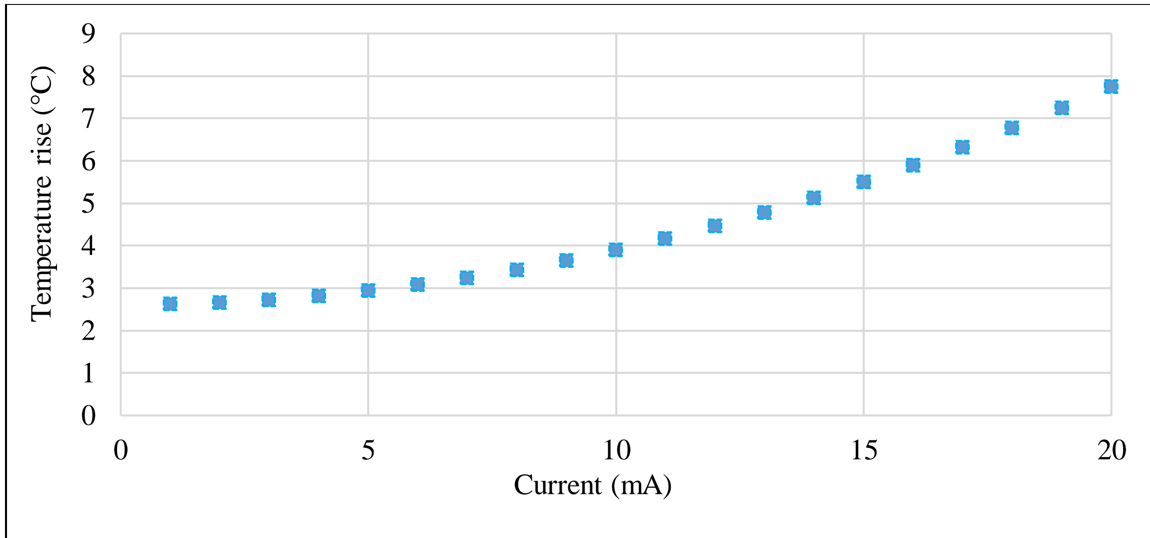

Fig. 4.11: Maximum temperature rise on the structure versus applied current

4.5.2 Laser heating

A 1mW, red laser with 635 nm wavelength was used for testing the micro-mirror. The laser shining onto the mirror could also increase the temperature of the mirror. The mirror is made of aluminum. Aluminum thin film reflects more than 90% of the incident light. Assuming the worst case, with the mirror absorbing 20% of the incident light, a power of 0.2 mW would be absorbed by the mirror. In a simulation

study, this amount of power was applied to the mirror to measure the temperature rise. A power of 0.2 mW causes a temperature increase of 1.6°C on the mirror surface. This amount of heat causes a negligible (<1%) deformation of the mirror surface.

4.6 Frequency domain analysis

In the past sections, a dc current was applied to the actuators and a *Stationary* study was run to explore the displacement, stress and temperature. In this section, resonance frequency of the micro-mirror is found using a *Frequency Domain* study. The physics of *Magnetic Fields, Electric Currents* and *Solid Mechanics* were run by a *Frequency Domain* study to find the frequency response of the system. An input current of 10 mA amplitude was applied to the actuators. The frequency of the input current was swept between 1 Hz to 500 Hz and the displacement was calculated at each frequency. Like the *Stationary* study, the *Frequency Domain* study was run for all the three types of motion including tilt about the *x-axis*, tilt about the *y-axis* and translational motion along the *z-axis*. The frequency response of the micro-mirror is shown in graphs of Fig. 4.12 for tilt-about-*x-axis*, Fig. 4.13 for tilt-about-*y-axis* and Fig. 4.14 for translation along the *z-axis* motion. These graphs show the normalized displacement of the mirror versus frequency of the input current. The resonance frequency is the frequency at which the displacement is maximum. According to the graphs, the resonance frequency of tilt about the *x-axis* motion is 294 Hz, the resonance frequency of tilt about the *y-axis* motion is 251 Hz and the resonance frequency of the *z-axis* translation is 165 Hz. These values will be compared with the experimental values in Chapter 7, section 7.3.1.

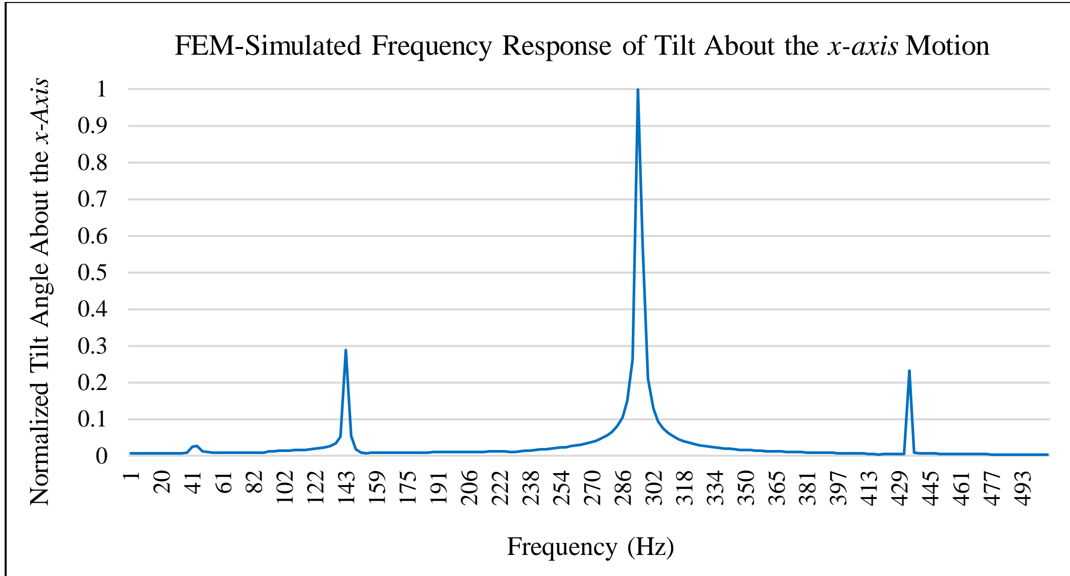

Fig. 4.12: FEM simulation of the frequency response of the micro-mirror tilting about the *x-axis*.

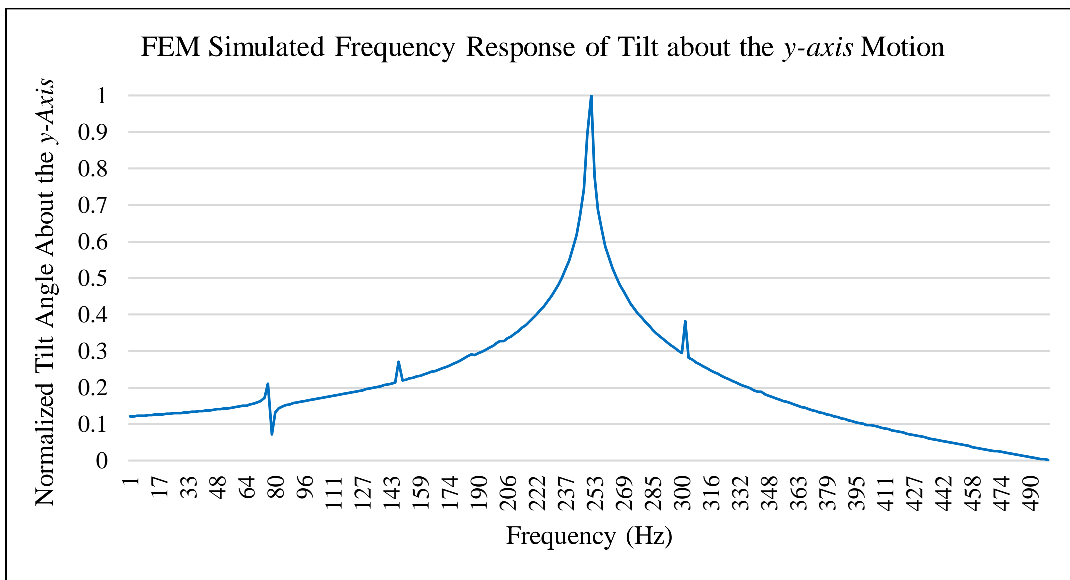

Fig. 4.13: FEM simulation of the frequency response of the micro-mirror tilting about the *y-axis*.

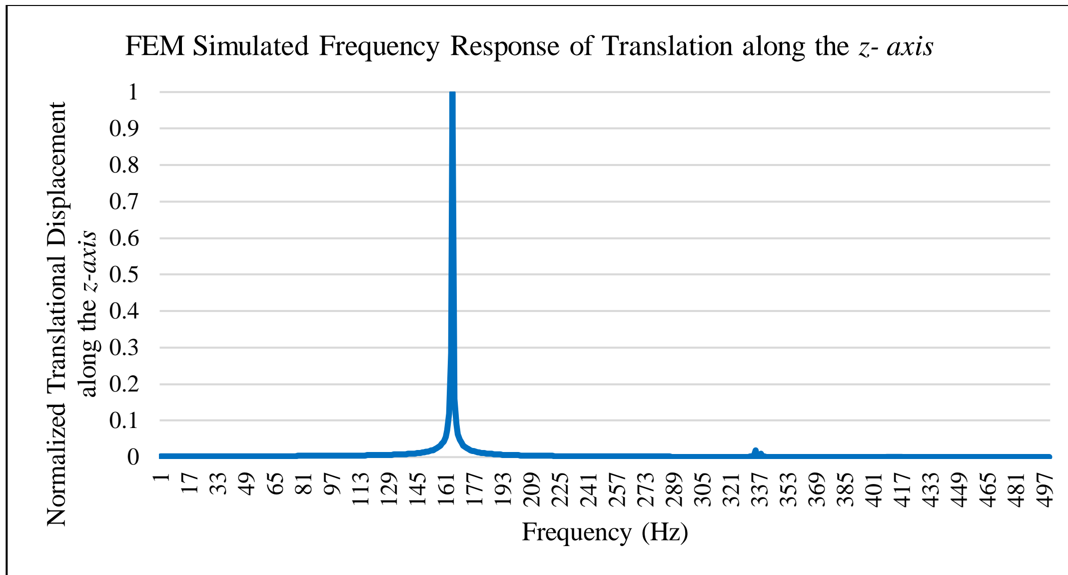

Fig. 4.14: FEM simulation of the frequency response of the micro-mirror moving along the *z-axis*.

4.7 Summary and conclusions

In this chapter, the performance parameters of the micro-mirror were explored using FEM simulations in COMSOL software. The factors that limit the input current of the micro-mirror including temperature rise and the electro-migration effect were discussed. A dc current was passed through the wires to make the 3 different types of motion. The amplitude of displacement by varying the input current from 1 mA to 20 mA was measured. For an input current of 20 mA, 5.6° tilting about the *x-axis*, 11° tilting about the *y-axis* and 23 µm translation motion along the *z-axis* were simulated. The amount of generated heat and the temperature rise on the flexures and mirror was explored to be 7.7°C for 20 mA of input current. The bending and torsional spring constants of the serpentine spring were calculated. Finally, a frequency domain analysis was run to find the resonance frequency of the system. The micro-mirror showed a resonance frequency of 251 Hz for tilting about the *y-axis*, 294 Hz for tilting about the *x-axis*, 165 Hz for translation in the *z-axis* motion.

5

Analytical Modeling of the MEMS Mirror

Contents

5.1 Introduction 48
5.2 Mass-Spring Model 49
5.2.1 Lumped Element Model 50
5.2.2 Transfer Function of the System 51
5.3 Frequency Domain Analysis 52
5.3.1 Euler-Lagrange's Equation 53
5.3.2 Resonance Frequency 56
5.3.3 Mode Coupling Effect 57
5.4 Summary and Conclusions 59

5.1 Introduction

This chapter discusses the mass-spring model, and the frequency domain analysis of the micro-mirror to explain the practical behaviour of the system. In Chapter 7 of this thesis, experimental results of the micro-mirror are presented. The analytical models of this chapter were developed to understand and explain the motion of the micro-mirror system. Therefore, in this chapter the spring constant values which were found in Chapter 4 using FEM simulations, were used in the developed analytical model, to explore

different parameters of the system (including transfer function and the dynamic frequency). The results of this model help explain the results presented in Chapter 7. The content of this chapter has been published in reference [58].

5.2 Mass-spring model

In this section, differential equations which describe the performance of the device are discussed. These equations are formed based on an equivalent circuit model for the mechanical mass-spring system. For this analysis, each type of motion is considered as a subsystem and analyzed individually. The equivalent circuit model would need to be recalculated for each type of motion separately. In this section, only the analysis of tilt about the *y-axis* is described assuming that there is no coupling between the motions. The other two modes would be calculated similarly and so are not shown.

Calculation of circuit model for tilt about the *y-axis*:

The mass-spring model of the device is shown in Fig. 5.1a and Fig. 5.1b. This model describes the device in tilting motion about the *y-axis*. The tilting axis is shown by a black-dashed line in Fig. 5.1a.

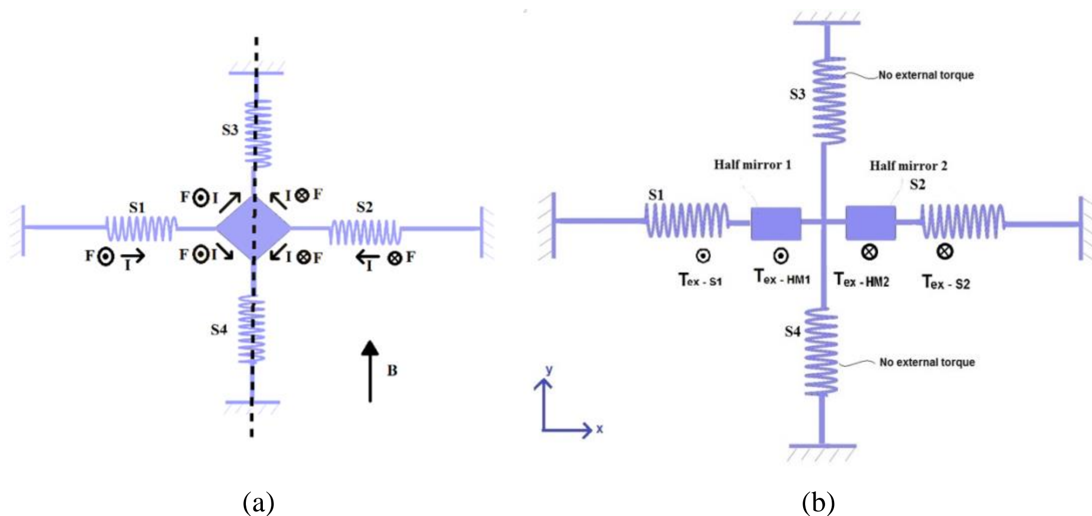

(a) (b)

Fig. 5.1: Mass-spring model of the structure. a) The current passing through the flexures and forces on the mirror sides. b) The torque on springs and mirror sides. HM: Half Mirror, T_{ex}: External Torque

Since the mirror is assumed to tilt about the *y-axis*, the mass of the mirror is split into two parts and shown by two masses in Fig. 5.1b. The serpentine springs are shown by spring symbol *S1-S4* in Fig. 5.1. T_{ex} shows the torque applied to the springs and half mirror caused by the Lorentz force.

5.2.1 Lumped Element Model

The equivalent electrical circuit of the mass-spring model for tilting about the *y-axis* is shown in Fig. 5.2. This model was made by representing the external torque as a voltage source, springs as capacitors and masses as inductors [59]. Since the mirror and springs move together and share the same speed, the equivalent electrical elements share the same current and were put in series.

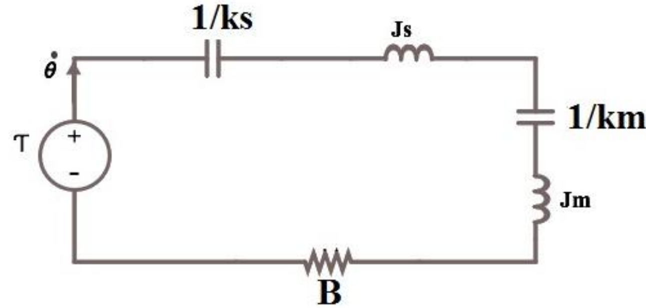

Fig. 5.2: Equivalent electrical circuit of the structure.

In Fig. 5.2 τ is the total external torque applied on half mirror and one flexure; k_s is the bending spring constant of one flexure; k_m is the bending spring constant of half of the mirror; J_m is the mass moment of inertia of half of the mirror; J_s is the mass moment of inertia of one flexure; B is the damping coefficient and θ is the tilt angle about the *y-axis*.

The spring constant (k_s, k_m) is defined as the resistivity of the object to move in a certain direction upon application of a force. For example, the bending spring constant of a spring is defined as how easy the spring bends when a bending moment is applied to it. In the same way, the torsional spring constant of a spring is defined as the resistivity of a spring to twisting, when a torsional force is applied to it.

Moment of inertia (J_s, J_m) is the equivalent of mass in the angular motions. The moment of inertia of an object defines how much torque is needed for a specific angular acceleration. Moment of inertia depends

on the mass and geometry of the object. In this structure, since the mass of the flexure is comparable to that of the mirror, the spring mass-moment-of-inertia was considered.

Damping coefficient (B) is the factor that determines how the stored energy in a system is dissipated. The dissipation of energy could occur due to the material damping, air friction, or some structural damping in the system.

The values of mass moment of inertia (J_s, J_m), spring constants (k_s, k_m) and damping coefficient (B) were calculated using finite element simulations and analytical calculations. The finite element simulations were explained in Chapter 4. The methods which were used to calculate these parameters are described in *Appendix A* (for the spring constants), *Appendix B* (for the moment of inertia) and *Appendix C* (for the damping coefficient). After the values were found, they were used to make the transfer function of the system.

The system was assumed to work in the linear regime. The equation of motion was written as follows [59]:

$$\tau = (k_s + k_m)\theta + B\dot{\theta} + (J_s + J_m)\ddot{\theta} \tag{5.1}$$

By applying a Laplace transformation on Equation 5.1, the transfer function of the system was derived as shown in Equation 5.2:

$$\frac{\theta}{\tau} = \frac{1}{(J_s + J_m)S^2 + BS + (k_s + k_m)} \tag{5.2}$$

5.2.2 Transfer function of the system

After finding the spring constants, mass moment of inertia and damping coefficient, the calculated values were substituted in 5.2, and the transfer function of the structure was calculated as below:

$$\frac{\theta}{\tau} = \frac{1}{1.8\times10^{-13}S^2 + 8.42\times10^{-11}S + 5.38\times10^{-7}} = \frac{5.5\times10^{12}}{S^2 + 468\,S + 2.98\times10^{6}} \tag{5.3}$$

From the transfer function, the following values can be calculated:

$$G(S) = \frac{1}{S^2+2\xi\omega_n S+\omega_n{}^2} \tag{5.4}$$

The natural frequency was calculated to be:

$$\omega_n = \sqrt{2.98 \times 10^6} = 1726.2\frac{rad}{s} = 274.5\ Hz \tag{5.5}$$

where ω_n is the resonance frequency of the micro-mirror when it is tilting about the *y-axis*.

The damping ratio ξ was calculated to be:

$$\xi = \frac{468}{2\times1726.2} = 0.13 \tag{5.6}$$

The value of ξ indicates that the system is underdamped. This means that by applying an input current of step function, the mirror will oscillate for a couple of ripples and then reaches its stationary position. The first peak of oscillations happens at time t_p calculated as below:

$$t_p = \frac{\pi}{\omega_n\sqrt{1-\xi^2}} = 1.8\ ms \tag{5.7}$$

The time that takes for the mirror to get within 2% of its stationary position is called the settling time and calculated as follows:

$$t_{s1} = \frac{4}{\xi_1\omega_n} = 17\ ms \tag{5.8}$$

These values will be evaluated with the values found by practical experiment in chapter 7.

5.3 Frequency Domain Analysis

The frequency response of the MEMS mirror is studied in this section. The purpose was to find the natural resonance frequencies and the corresponding pattern formed upon applying each frequency. This analysis is based on the overall kinetic and potential energy of the system. Therefore, it covers all the three types of motions and also calculates the coupling effect of motions on each other. The mechanical deformation of the system can be different for different input frequencies. Studying the dynamic response of the system enables choosing the right frequency of operation. Lagrange’s equations of motions were used to describe the motion of the system in the dynamic mode.

5.3.1 Euler-Lagrange's Equation

Lagrange's equation of a system basically uses the kinetic and potential energy of the system to describe its motion trajectory. The Lagrange's equation is written as below [60]:

$$\frac{d}{dt}\left(\frac{\partial L}{\partial \dot{q}_i}\right) - \frac{\partial L}{\partial q_i} = 0 \tag{5.9}$$

$$L = K - P$$

where K is the kinetic energy, P is the potential energy, q_i are generalized coordinates. Generalized coordinates (q_i) belong to a set of points that can define the position of a moving system. In this system, 4 points at the corners of the mirror were studied which can describe the 3 motions of the mirror including two tilting motions and one translational motion. q_i dotted are generalized velocities.

Kinetic Energy

The total kinetic energy is the sum of kinetic energies of three motions of the mirror:

$$K = \frac{1}{2}m(\dot{u}_z)^2 + \frac{1}{2}J_x(\dot{\theta}_x)^2 + \frac{1}{2}J_y(\dot{\theta}_y)^2 \tag{5.10}$$

where θ_x is the tilt angle about the *x-axis*, θ_y is the tilt angle about the *y-axis* and u_z is the translational displacement in the *z-axis*. $\dot{\theta}_x$, $\dot{\theta}_y$ and $\dot{u}_z$ are the angular and linear velocities of the system. m, J_x and J_y represent the mass, moment of inertia about the *x-axis* and moment of inertia about the *y-axis* of the system.

Potential Energy

In the three types of motions explained earlier, each spring can either have a bending or a torsional motion. For example, in tilting about *y-axis* motion, springs number 1 and 2 have a bending motion while springs number 3 and 4 have a torsional motion. The bending and torsional motions switch for the tilting about the *x-axis* motion. Therefore, potential energy consists of the energy stored in the four springs due to the bending or torsional motions. In the following, the bending and torsional potential energies are written separately. For writing the potential energy equations, the corners are labeled according to Fig. 5.3.

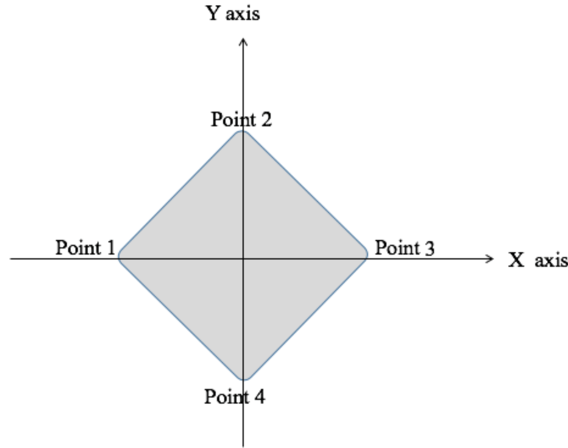

Fig. 5.3: Labelling of corners for potential energy.

The potential energy due to the bending is:

$$U_{bending} = \overbrace{\frac{1}{2}k_{f_z-u_z}u_{1z}{}^2}^{Point\#1\ tranlation\ in\ z\ axis} + \overbrace{\frac{1}{2}k_{M_y-\theta_y}\theta_y{}^2}^{Point\#1\ bending\ about\ y\ axis} + \overbrace{k_{f_z-\theta_y}u_{1z}\theta_y}^{Point\ \#1\ bending\ due\ to\ z\ force}$$
$$+ \overbrace{\frac{1}{2}k_{f_z-u_z}u_{3z}{}^2}^{Point\#2\ tranlation\ in\ z\ axis} + \overbrace{\frac{1}{2}k_{M_y-\theta_y}\theta_y{}^2}^{Point\#2\ bending\ about\ y\ axis} + \overbrace{k_{f_z-\theta_y}u_{3z}\theta_y}^{Point\ \#2\ bending\ due\ to\ z\ force}$$
$$+ \overbrace{\frac{1}{2}k_{f_z-u_z}u_{2z}{}^2}^{Point\#3\ tranlation\ in\ z\ axis} + \overbrace{\frac{1}{2}k_{M_x-\theta_x}\theta_x{}^2}^{Point\#3\ bending\ about\ x\ axis} + \overbrace{k_{f_z-\theta_x}u_{2z}\theta_x}^{Point\ \#3\ bending\ due\ to\ z\ force}$$
$$+ \overbrace{\frac{1}{2}k_{f_z-u_z}u_{4z}{}^2}^{Point\#4\ tranlation\ in\ z\ axis} + \overbrace{\frac{1}{2}k_{M_x-\theta_x}\theta_x{}^2}^{Point\#4\ bending\ about\ x\ axis} + \overbrace{k_{f_z-\theta_x}u_{4z}\theta_x}^{Point\ \#4\ bending\ due\ to\ z\ force} \quad (5.11)$$

The potential energy due to the torsion is:

$$U_{tor} = \overbrace{\frac{1}{2}k_{T_x-\theta_x}\theta_x{}^2}^{Point\#1\ twisting} + \overbrace{\frac{1}{2}k_{T_x-\theta_x}\theta_x{}^2}^{Point\#2\ twisting} + \overbrace{\frac{1}{2}k_{T_y-\theta_y}\theta_y{}^2}^{Point\#3\ twisting} + \overbrace{\frac{1}{2}k_{T_y-\theta_y}\theta_y{}^2}^{Point\#4\ twisting} \quad (5.12)$$

As mentioned earlier in this chapter, the spring constant is the resistivity of the spring to move in a certain direction upon an applied force. Variables denoted by $k_{xx\text{-}yy}$, are the spring constants in the *yy* direction upon applying the force or moment *xx*. The detailed explanation is given in Table 5.1.

Table 5.1: Values of the parameters used in the equations of bending and torsional potential energy.

$k_{f_z-u_z}$	Spring constant in *z*-direction when a force along the *z-axis* is applied to the spring.	0.06 N/m
$k_{M_y-\theta_y}$, $k_{M_x-\theta_x}$	Spring constant in tilting about *x*- or *y*- axes, when a moment of bending is applied to the spring.	$1.9\times10^{-4} \pm 2\%$ N·m/rad
$k_{f_z-\theta_x}$, $k_{f_z-\theta_y}$	Spring constant in tilting about *x*- or *y*- *axes*, when a force is applied to the spring in *z*- *axis*.	$8.2\times10^{-5} \pm 2\%$ N/rad
$k_{T_x-\theta_x}$, $k_{T_y-\theta_y}$	Spring constant in twisting about *x*- or *y*- axes, when a torsional force is applied to the spring in *z*-*axis*.	$2.6\times10^{-8} \pm 2\%$ N·m/rad
J_x, J_y	Mass moment of inertia of the system about *x*- or *y*- axes.	1.4×10^{-10} kg·m^2
m	Mass of the structure.	2×10^{-7} kg

These values were calculated using the finite element simulation that was explained in Chapter 4. To simplify the equations, the number of variables is reduced by re-writing the *z-axis* displacements of points 1 to 4 (u_{1z}, u_{2z}, u_{3z}, and u_{4z}) as a function of the center's displacement and the tilt angles.

$$u_{1z} = u_z - R\theta_y \tag{5.13}$$

$$u_{2z} = u_z + R\theta_x \tag{5.14}$$

$$u_{3z} = u_z + R\theta_y \tag{5.15}$$

$$u_{4z} = u_z - R\theta_x \tag{5.16}$$

where R is the distance between the center and corners which is equal to 1.4 mm.

By substituting the Equations 5.10, 5.11 and 5.12 in Equation 5.9, Lagrange's equation can be written as:

$$\frac{d^2\theta_x}{dt^2} = -\left(\frac{2R^2k_{f_z-u_z}+2k_{M_x-\theta_x}+2k_{T_x-\theta_x}}{J_x}\theta_x(t) + \frac{2K_{f_z-\theta_x}}{J_x}u_z(t)\right) \tag{5.17}$$

$$\frac{d^2\theta_y}{dt^2} = -\left(\frac{2R^2K_{f_z-u_z}+2k_{M_y-\theta_y}+2k_{T_y-\theta_y}}{J_y}\theta_y(t) + \frac{2K_{f_z-\theta_y}}{J_y}u_z(t)\right) \tag{5.18}$$

$$\frac{d^2u_z}{dt^2} = -(\frac{2k_{F_z-\theta_x}}{m}\theta_x(t) + \frac{2k_{F_z-\theta_y}}{m}\ \theta_y(t) + \frac{4k_{F_z-u_z}}{m}u_z(t)) \tag{5.19}$$

The matrix form of Lagrange's equation is written as below:

$$\underbrace{\begin{bmatrix} J_x & 0 & 0 \\ 0 & J_y & 0 \\ 0 & 0 & m \end{bmatrix}}_{[M]} \begin{bmatrix} \ddot{\theta}_x \\ \ddot{\theta}_y \\ \ddot{u}_z \end{bmatrix} + \underbrace{\begin{bmatrix} 2R^2k_{f_z-u_z} + 2k_{M_x-\theta_x} + 2k_{T_x-\theta_x} & 0 & 2k_{f_z-\theta_x} \\ 0 & 2R^2K_{f_z-u_z} + 2k_{M_y-\theta_y} + 2k_{T_y-\theta_y} & 2k_{f_z-\theta_y} \\ 2k_{F_z-\theta_x} & 2k_{F_z-\theta_y} & 4k_{F_z-u_z} \end{bmatrix}}_{[k]} \begin{bmatrix} \theta_x \\ \theta_y \\ u_z \end{bmatrix} = 0 \tag{5.20}$$

$$[M]\begin{Bmatrix} \ddot{\theta}_x \\ \ddot{\theta}_y \\ \ddot{u}_z \end{Bmatrix} + [k]\begin{Bmatrix} \theta_x \\ \theta_y \\ u_z \end{Bmatrix} = \begin{Bmatrix} 0 \\ 0 \\ 0 \end{Bmatrix} \tag{5.21}$$

where [M] is called the mass matrix and [*k*] is called the spring constant matrix.

The differential equations were solved using MATLAB. Since at the start time, the mirror is at a stable position with no tilting or linear displacement, the following initial conditions were applied to solve the equations:

$$\theta_x(0) = 0\ , \theta_y(0) = 0, u_z(0) = 0$$

Let's assume the mirror is tilting about the *x-axis* and there is no movement in the direction of θ_y or u_z. The equation of motion is as below:

$$\frac{d^2\theta_x}{dt^2} = -(\frac{2R^2k_{f_z-u_z} + 2k_{M_x-\theta_x} + 2k_{T_x-\theta_x}}{J_x}\theta_x(t)) \tag{5.22}$$

and $\theta_x(t)$ is:

$$\theta_x(t) = C_1 \sin\sqrt{\frac{2R^2k_{f_z-u_z} + 2k_{M_x-\theta_x} + 2k_{T_x-\theta_x}}{J_x}}\ t \tag{5.23}$$

where C_1 is a constant. This motion is expected to make a linear pattern of light on the screen.

5.3.2 Resonance frequency

By finding the eigenvalues of the matrix $[M]^{-1}[k]$ using MATLAB, the resonance frequency of different motions was calculated.

$$\det(-\lambda[I] + [D_s]) = 0 \tag{5.24}$$

$$\lambda = \omega^2$$

$$D_s = [M]^{-1}[k]$$

where:

$$[M] = \begin{bmatrix} J_x & 0 & 0 \\ 0 & J_y & 0 \\ 0 & 0 & m \end{bmatrix}$$

$$[k] = \begin{bmatrix} 2R^2k_{f_z-u_z} + 2k_{M_x-\theta_x} + 2k_{T_x-\theta_x} & 0 & 2k_{f_z-\theta_x} \\ 0 & 2R^2K_{f_z-u_z} + 2k_{M_y-\theta_y} + 2k_{T_y-\theta_y} & 2k_{f_z-\theta_y} \\ 2k_{F_z-\theta_x} & 2k_{F_z-\theta_y} & 4k_{F_z-u_z} \end{bmatrix}$$

The resonance frequency of the tilt-about-*y-axis* motion was found to be 244.4 Hz, and the resonance frequency of tilt-about-*x-axis* was found to be 287.6 Hz, and the resonance frequency of the *z-axis* translation was found to be174.3 Hz.

5.3.3 Mode coupling effect

From the Equations 5.17, 5.18 and 5.19 it can be seen that there is a coupling between the motions in the three axial directions. This means that a motion in any one axis contributes to the motions in the other axial directions. The contribution of other axial motions is not significant until the input frequency approaches the resonance frequency of one of the other axial motions. When the applied frequency to one axial motion, is close to the resonance frequency of the other axial motion, the motion in the other axial direction becomes significant. In this case, the mirror would move in more than one axial direction.

The motion functions $\theta_x(t)$, $\theta_y(t)$, and $u_z(t)$ were solved to find and understand the light patterns generated by the deflection shapes of the mirror. To solve the equations, an excitation was applied to one axial motion at time zero when the system was stable. This impulse function, which was applied at time zero, creates excitation at all frequencies. This enables studying the behavior of the system at all frequencies.

To create the plots of the motion functions, time was swept for 180 seconds with intervals of 0.1 s and the value of the motion functions was found at each time. Fig. 5.4 shows $\theta_y(t)$ plotted versus $\theta_x(t)$. At each time step, the dominant displacement is shown by a line. The traces show the displacement at various

time steps. The modes of horizontal motion (*x-axis* tilt, red dashed line), vertical motion (*y-axis* tilt, green dashed line), and an elliptical mode (*z-axis* translation, purple dashed line) are shown in the plot. The main resonance modes of the mirror are marked by three dashed lines in the Figure. The red dashed line corresponds to 287.6 Hz (*x-axis*), the green dashed line corresponds to 244.4 Hz (*y-axis*), the purple dashed line corresponds to 174.3 Hz (*z-axis*).

From the graph of Fig. 5.4, it can be expected that the pattern of light changes by sweeping the frequency of current applied to the actuator's terminals. In order to have a straight horizontal or vertical light pattern, the frequency of input current should match the resonance frequencies which were calculated above. When θ_x is actuated in a frequency which is not its natural frequency, the pattern of light can deviate from a straight horizontal line. This fact will be further explored in the experimental results of chapter 7.

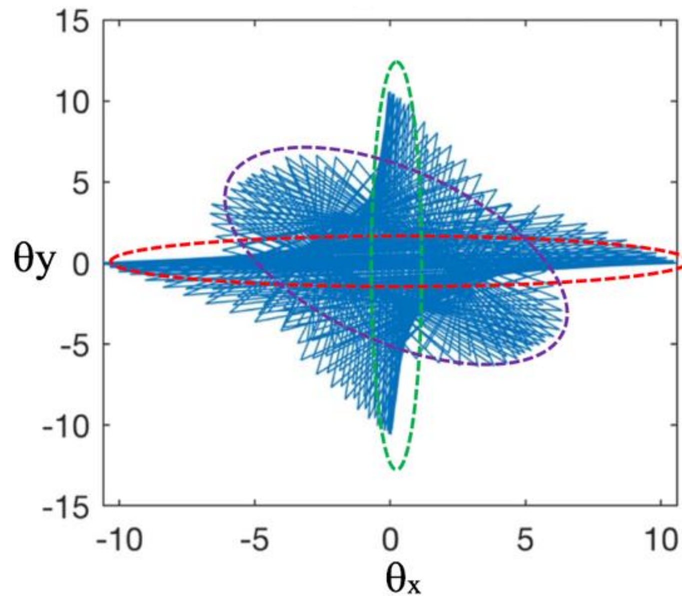

Fig. 5.4: Trajectory of the motion functions derived by solving Lagrange's equations. Mode shapes can be seen in this figure.

5.4 Summary and conclusions

In this chapter, an analytical model was developed to explore the motion of the micro-mirror system. The transfer function of the micro-mirror was presented using the mass-spring and Lumped-element modeling. A modal analysis was done by solving the Lagrange's equations for the system. This model can explain the dynamic behavior of the system. The expected light pattern at resonance modes of the *x-axis* and the *y-axis* motions were presented. Motion coupling between the modes was also explained. In Chapter 7, the experimental results of the micro-mirror are presented which shows the practical responses of the modeling results of this chapter.

6

Microfabrication

Contents

6.1 Introduction 60
6.2 Fabrication Process 62
6.3 Static Deformation of the Mirror 74
6.4 Summary and Conclusions 74

6.1 Introduction

In the previous chapters, the micro-mirror was designed and simulated. After finalizing the geometrical parameters of the micro-mirror, it was fabricated using bulk and surface microfabrication techniques. In this chapter, the fabrication process is explained. Graph of Fig. 6.1 shows a schematic chart of the fabrication steps. In summary, the fabrication process includes the following steps.

1. Choosing appropriate silicon wafer and cutting it down to small pieces
2. Wafer oxidation

3. Patterning oxide layer
4. Oxide etching
5. Silicon etching
6. Alignment marks opening
7. Oxide removal
8. Growing new oxide
9. Depositing titanium and aluminum
10. Patterning aluminum
11. Aluminum etching
12. Ti and SiO_2 etching
13. Removing photoresist
14. Covering the mirror and flexures with thick photoresist
15. Thinning the structure from front and backside
16. Releasing the structure
17. Removing photoresist

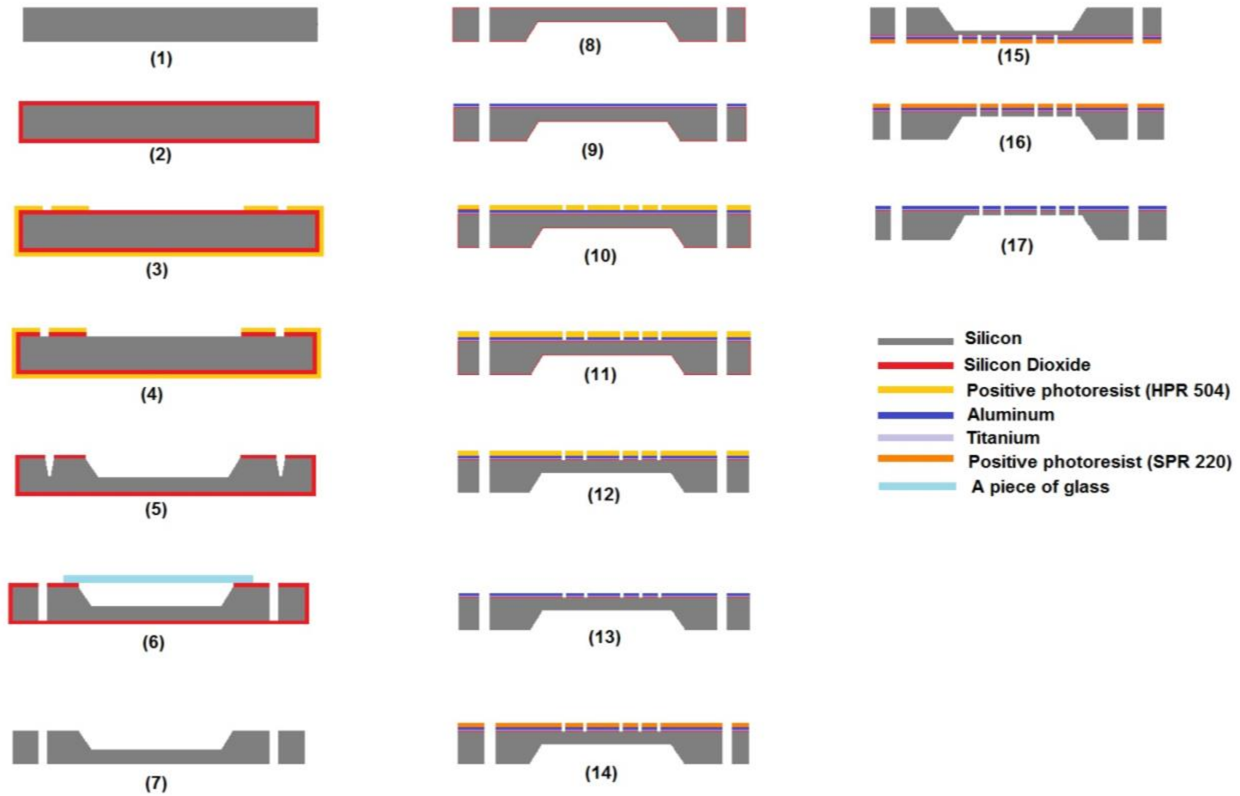

Fig. 6.1: Fabrication process steps diagram.

6.2 Fabrication process

In the following, every step is discussed in detail.

1. Wafer cutting and cleaning

A silicon wafer of 4 inches diameter, 300 μm thickness, P-type doping, <100> Orientation and double-side-polished was selected for this project.

Wafers were first diced into pieces of 4 cm × 4 cm and 2 cm × 2 cm using a wafer-saw. The cutting lines that are shown in Fig. 6.2, divide a 4-inch wafer into two pieces of 4 cm × 4 cm and six pieces of 2 cm × 2 cm samples. Samples of size 2 cm × 2 cm fit one micro-mirror and samples of size 4 cm × 4 cm fit four micro-mirrors.

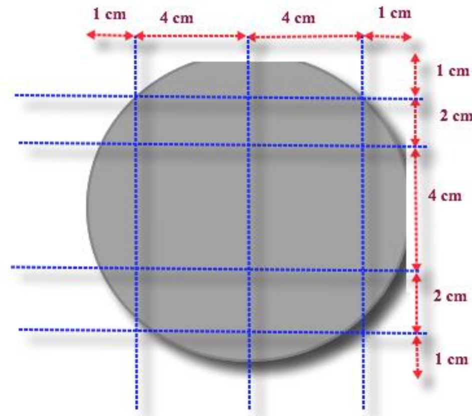

Fig. 6.2: Cutting lines of a 4-inch wafer.

After cutting the wafers by saw-machine, wafer pieces were contaminated by silicon particles. The wafer pieces were washed with acetone, rinsed with Isopropyl Alcohol (IPA) and dried with N_2. The next step of cleaning was washing the sample using piranha solution. Piranha is a solution of 1:4/ H_2O_2 (Hydrogen peroxide): H_2SO_4 (Sulfuric Acid) was made and samples were put in the solution for 7-10 minutes. Samples were rinsed with water and dried with N_2 gas. This process is done to remove organic contamination from the silicon surface. Next, samples were washed with Buffered-Oxide-Etch (BOE) solution for removing any native oxide on top of the silicon wafer. BOE solution is a mixture of Hydrofluoric acid and ammonium fluoride. Samples were put in the solution for 5 minutes and then rinsed with water and dried with N_2 gas.

2. Oxidization

A layer of silicon dioxide (SiO_2) was used as the mask layer for etching silicon in wet etch solution which will be discussed later in this chapter. Therefore, a layer of SiO_2 was needed to cover the top and bottom surfaces of the samples. SiO_2 was grown using a wet oxidation method. In this process, the samples were put in a high-temperature furnace and exposed to the water vapor. The temperature of the furnace was set at 1100°C and the samples were put in the surface for 14 hours. The oxide thickness was measured

using an ellipsometer (M-2000 J.A. Woolam). The average of three spots on the front side and back side of each sample was measured. The oxide thickness was measured to be 1.5 µm.

3. Oxide patterning-Lithography #1

At this step, the pattern of the membrane was made on the backside of the wafer, so that the oxide on the backside of the wafer, at the membrane location, could be etched away at the next step. All the patterns including the mirror and wires were transferred to the silicon surface using an optical lithography process. A lithography mask is a stencil which is used to transfer the pattern through a photosensitive resin. Before starting the fabrication process, two lithography masks were designed using Tanner L-Edit software. The masks were fabricated in the NanoFab at the University of Alberta. Four patterns each in two sizes of 2 cm × 2 cm and 4 cm × 4 cm pieces were included in the masks. The patterns were:

1) Backside etching
2) Aluminum patterning (wires and mirror)
3) Edge bead removal
4) Protection for releasing

Each pattern was used at a certain step of lithography. For the first lithography process, the backside of the wafer was supposed to be patterned to open a square, therefore, *backside etching* pattern of Fig. 6.3 was used.

After the wafers were oxidized, they were washed with acetone and rinsed with IPA solutions. A dehydration bake was done at 110ºC for 3 minutes. HMDS curing was done for 5 minutes at 150ºC to improve the adhesion of photoresist to SiO_2 surface. The samples were covered with HPR 504 photoresist by spin-on-coating process using Solitech spin coater machine. A vacuumed hot plate was used to bake the samples in 110°C for 90 s. The samples were aligned with the *backside etching* pattern and the photoresist was exposed to UV light with an intensity of 30 mW/cm^2 for 3s. The samples were then immersed in a

developer solution that removed the photoresist from the exposed area. At last, samples were baked in 110ºC for 6 min.to make the photoresist more durable for the etching process.

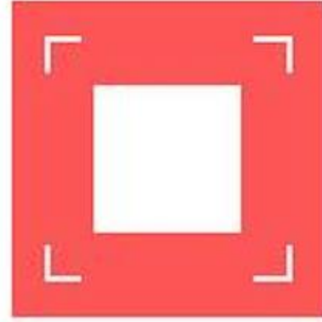

Fig. 6.3: Schematic of the *backside etching* pattern showing the backside opening and alignment marks.

4. Oxide etching

The oxide on the opened area was etched using a Buffered-Oxide-Etching (BOE) solution. BOE solution was made of ammonium fluoride (NH_4F), and hydrofluoric acid (HF) with a volume ratio of 6 to 1. The samples were put in BOE solution for 28 minutes to remove 1.5 µm of oxide. The samples were rinsed with water and dried with N_2. After this step, the samples were washed with acetone and rinsed with IPA to remove the photoresist from the other area.

5. Silicon etching-KOH

Potassium hydroxide (KOH) solution was used to etch the bulk silicon. The KOH 30% solution was made by dissolving 570 g of solid KOH in 1000 ml of water. To make a uniform etching, the sample was rotated upside-down and displaced from the front to the back of the container every hour. Etching was done at 80ºC for 4 hours and 35 minutes. The sample was carefully rinsed with low-pressure water and dried with low-pressure N_2. The final thickness of the membrane was 25 µm.

Fig. 6.4a shows a schematic of the side view of the etched sample including its dimensions. A slope of 54.7° was made at the edge borders of the silicon wafer. This slope is because of the angle between the

(100) and (111) crystal planes of the silicon. The lateral distance caused by this angle was considered in designing the mask. Fig. 6.4b shows a photo of an etched sample. The photo on the right side is the back side of the sample.

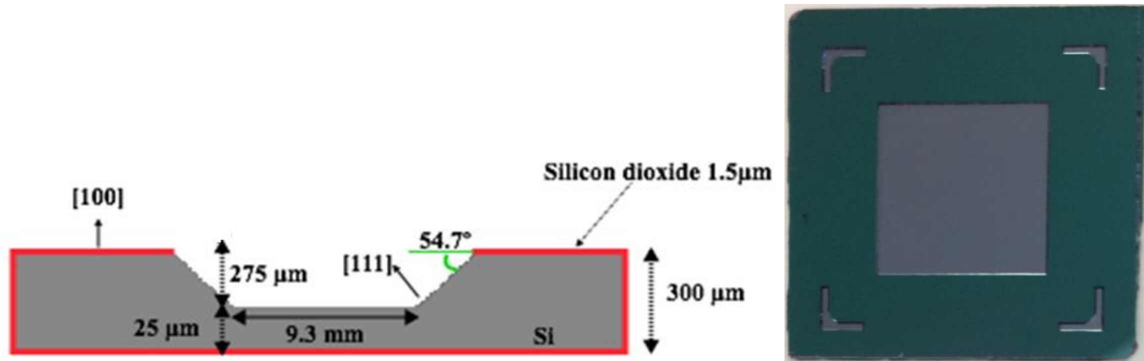

Fig. 6.4: a) Side view of the etched sample. b) Front view of a back-etched sample.

6. Alignment mark opening using anisotropic plasma etching

The device was fabricated within the location of the etched backside square, but now from the frontside of the sample. To align the lithography wiring pattern with the membrane location, some alignment marks were needed. For this purpose, an L-shaped mark was placed at each corner of the sample which can be seen in Fig. 6.4b. These marks were thinned in the KOH and released by plasma etching after KOH process. In this way, the location of the membrane could be determined from the frontside. The etched area was covered with a piece of glass and the alignment marks were etched using plasma etching technique. After about 60 minutes of plasma etching of the alignment marks they could be seen from the front side of the sample.

7. Oxide etching

After etching the silicon in KOH and opening the alignment marks, the wet oxide which was grown on the sample at step 2 was damaged. The oxide was removed by BOE solution. Samples were left in BOE for 30 minutes and all the oxide was removed. Samples were slowly rinsed and dried with N_2.

8. New layer of oxide growth

An electrically insulating layer was needed between the silicon substrate and aluminum wires. A layer of 100 nm silicon dioxide was thermally grown on the frontside of the silicon membrane.

9. Aluminum and Titanium deposition

Conductor wires were made of aluminum metal. Before depositing aluminum, in order to improve the adhesion of Al to SiO_2, a thin layer of 25 nm titanium was deposited on the SiO_2 layer using dc sputtering technique. Then, a layer of 1.5 µm aluminum was deposited on top of the Ti layer using thermal evaporation technique. Table 6.1 shows the properties of deposited Al layer. This film was deposited using three separate thermal evaporation runs, since each run can only get about 0.5 µm thickness.

Table 6.1: Properties of the deposited aluminum layer.

Deposition method	Thermal evaporation
Ave. Thickness	1.5 µm
Resistivity	0.518 Ω.cm
Average Surface roughness	139.4 Å
Optical reflection	~ 90%
Stress	42 MPa

10. Patterning aluminum - Lithography #2

After depositing aluminum, the samples were washed by acetone and rinsed by IPA and dried. At this step, the Al layer needed to be patterned to make the wires and the mirror pattern. For this purpose, the second mask (Fig. 6.5) was used. The alignment marks shown on the figure were used to align the pattern with the sample.

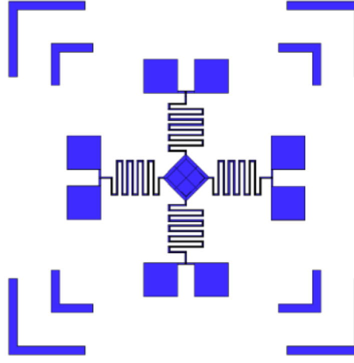

Fig. 6.5: The masking pattern of the aluminum wires and mirror.

The regular steps of optical lithography were done for patterning the aluminum. The steps included: dehydration baking, promoting adhesion using HMDS material; coating sample with photoresist using spin-on-coating technique; baking the sample with photoresist; aligning the pattern with the sample and exposing to UV light; developing the sample using a developer solution to remove photoresist from exposed area and baking the sample.

After performing the above-mentioned steps, the locations of wires and the mirror were covered with photoresist and the other locations were open. In this way, at the next step, the Al on all the open areas could be removed.

11. Aluminum etching

Aluminum etching was done to remove the Al on the areas which were not covered with photoresist. The Aluminum etchant solution was a mixture of 5% HNO_3, 80% H_3PO_4, 5% HAC and 10% DI water. A hot plate was used to heat up the solution to 50ºC with magnetic stirring of 300 rpm. At the temperature of 50ºC, the etch-rate of the solution was measured to be 517.2 nm/min and the Al was etched for 3 minutes. Samples were rinsed with DI water and dried with N_2.

12. SiO_2 and Ti etching

The oxide which was deposited at step 8, was needed to be etched at this step. Since the insulation layer is only required to disconnect aluminum wires from the silicon substrate, in the areas without aluminum wire, the oxide was etched. Etching oxide is important before releasing the structure, since at the final step, anisotropic plasma etching will be used for etching silicon, which does not etch the oxide. The sample was put in a BOE solution for 5 minutes to remove the silicon dioxide. This also helped to remove the metal oxide formed on the aluminum wires. The BOE solution also removed the thin Ti layer from the open areas of the sample.

13. Removing photoresist

After etching was done, the photoresist was removed by rinsing with acetone.

14. Covering the mirror and flexures with thick photoresist-Lithography #3

When the aluminum wires were made and the SiO_2 layer was removed, the last step was to etch away the silicon substrate to release the structure. For this purpose, the areas which were part of the final structure were covered with a thick layer of photoresist using a lithography process and the other area was uncovered to be exposed to the plasma etcher. The pattern shown in Fig. 6.6 was used for this lithography process. At this lithography process aligning was extremely important. Any misalignment between the mask and Al wires, would expose the aluminum to plasma etcher which would damage its surface and also etch away some part of the substrate which must be remained. The alignment was done under a microscope. First, the 4 alignment marks were matched, then all the 4 serpentine flexures were carefully aligned.

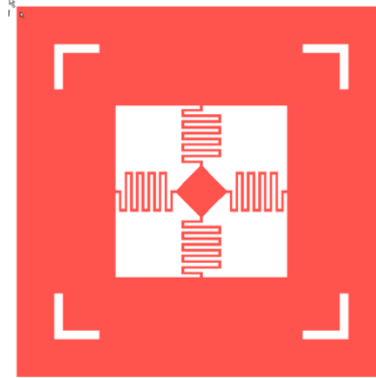

Fig. 6.6: Pattern used for covering the flexures and mirror. The red area will remain as part of the final structure.

The photoresist used for this process was SPR 220 which is a positive photoresist. This photoresist is denser than HPR 504 and can form a layer of up to 30 µm thickness. Therefore, it can protect the flexures and mirror against physical and chemical impacts in the plasma etching system. It also needs a longer UV exposing time, due to its large thickness. The regular lithography steps which were mentioned earlier were used to cover the mirror and flexures. A photo of a sample after this lithography process is shown in Fig. 6.7. The mirror and flexures were covered with photoresist and all the other areas were not covered.

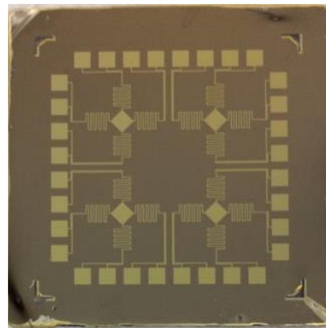

Fig. 6.7: Al pattern covered with SPR 220 photoresist.

15. Thinning the structure from the frontside

After covering the flexures and mirror with a dense photoresist SPR 220, the sample was ready for being etched in plasma etching system. At this step, the thickness of the membrane was 24 µm. This value was double checked by measuring the step height from the backside of the sample using alpha step profiler

before etching. Plasma etching was done in two steps. At the first step, an anisotropic plasma etching was done from the frontside to define the thickness of the membrane. At this step, silicon was etched for 5 µm from the frontside. The settings of Table 6.2 were used on Trion Phantom II plasma etching system:

Table 6.2: Anisotropic plasma etching properties used for thinning the silicon wafer.

Anisotropic Etching Recipe	
ICP power	254 W
RIE power	145 W
SF_6	15 SCCM
O_2	6 SCCM
CHF_3	17 SCCM
Pressure	66 mTorr
Si etch rate:	1.24 µm/min

After this 5 µm anisotropic etching, the thickness of silicon under the covered area was 25 µm, while the thickness of silicon at the uncovered area was 20 µm.

16. Releasing the structure

After doing anisotropic plasma etching for 5 µm, the sample was flipped over and the backside was exposed to the plasma etching gas. At this step, silicon was isotropically etched for 20 µm which totally removed the silicon at the uncovered areas and released the structure. For this purpose, the parameters of Table 6.3 were set on Trion plasma etching system.

Table 6.3: Isotropic plasma etching properties used for releasing the silicon wafer.

Isotropic Etching Recipe	
ICP power	203 W
RIE power	63 W
SF_6	58 SCCM
O_2	0
CHF_3	0
Pressure	302 mTorr
ICP RF reflected:	7 W
RIE RF reflected:	4 W
dc bias read	-10 V
Si etch rate	1.25 µm/min (Varies between 1 to 1.5 µm/min)

After this step, the sample was observed under a microscope to ensure that the flexures and mirror were released. Using the 100x objective, the thickness of the springs were measured at their two ends and the middle. The measured values of the thickness are shown in Fig. 6. 8. The average thickness was measured to be 5±2 µm.

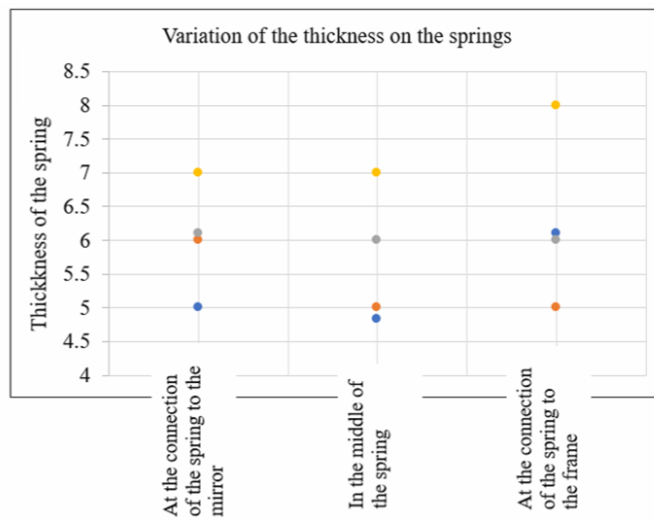

Fig. 6. 8: Variation of the thickness of the structure across the springs

17. Photoresist removal

After releasing the structure, the SPR 220 photoresist was removed using an oxygen plasma technique. The recipe of Table 6.4 was used on Trion plasma etching system. Oxygen plasma etching was done for about 1 hour until the photoresist was gone.

Table 6.4: properties of oxygen plasma etching process used for etching the thick layer of photoresist.

O_2 Plasma	
ICP	100 W
RIE	70 W
Pressure	100 mTorr
O_2	45 SCCM

Fig. 6.9a shows a photo of a sample after releasing. This sample was then mounted on a prototype board and the connector wires were soldiered as shown in Fig. 6.9b.

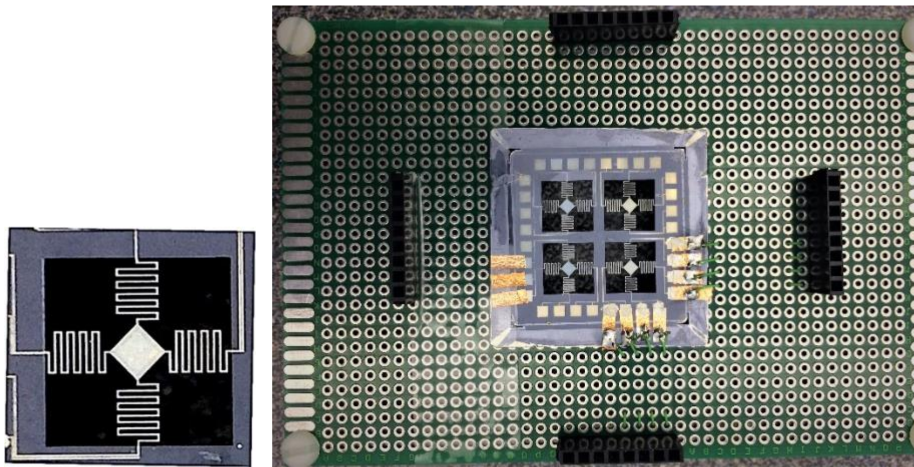

Fig. 6.9: a) Photo of a released sample. b) A sample mounted on a prototype board for testing.

The electrical resistivity of each path of Al wires, including the contact pads and the extension wires, was measured to be an average of 26.4Ω.

6.3 Static deformation of the mirror

To determine the flatness of the fabricated mirror, it was inspected under an optical microscope. First, the objective lens of the microscope was focused on the center of the mirror. Then, the mirror was moved and the lens was focused on one corner of the mirror. The displacement of the focal point of the center and the corner of the mirror was recorded. This value is equal to the vertical displacement of the stage of the microscope which was recorded by reading the amount that the knob was turned. After measuring the height difference between the center and the four corners of the mirror, the average value was calculated to be 9 μm. Comparing to the side length of the mirror which is 2 mm, this value equals 0.45% of the mirror side length and results in a radius of curvature (ROC) of 11 cm.

6.4 Summary and conclusions

In this chapter, the standard microfabrication techniques which were employed to fabricate the MEMS mirror were explained. At some steps of the process, the details of the technique were adjusted for the special requirements of this MEMS mirror. The recipes of these details were given in this chapter. After the MEMS mirror was fabricated, it was mounted on a board and the deformation of the mirror's surface was measured under an optical microscope. In the next chapter, the mirror is tested at different conditions and the results are reported.

7

Experiments and Results

Contents

7.1 Introduction 75
7.1.1 Variation of the Magnetic Field 76
7.1.2 Optical Angle Calculation 77
7.2 Static Response 79
7.2.1 Static Tilting 80
7.2.2 Step Response 82
7.3 Dynamic Response 84
7.3.1 Resonance Frequency 84
7.3.2 Dynamic Deformation of the Mirror 88
7.3.3 Mode Coupling Effect 90
7.3.4 Raster Scan 91
7.4 Comparison with Other Works 92
7.5 Summary and Conclusions 93

7.1 Introduction

In the previous chapter, the fabrication of the micro-mirror was described. The fabricated micro-mirror was then mounted on a prototype board as shown in Fig. 6.9b of chapter 6. To minimize the

environmental optical and mechanical noise, the device was placed inside a closed box and on a vibration isolation table during testing. The setup of Fig. 7.1 was used to test the device and includes:

- A PTI Technologies PM01 G3, 1 mW, 625 nm laser diode to shine light on the mirror
- An API SD380-23-21-051 photodetector was used to detect the reflected light.
- N42 (BY08Y0, K&J Magnetics) permanent magnet.

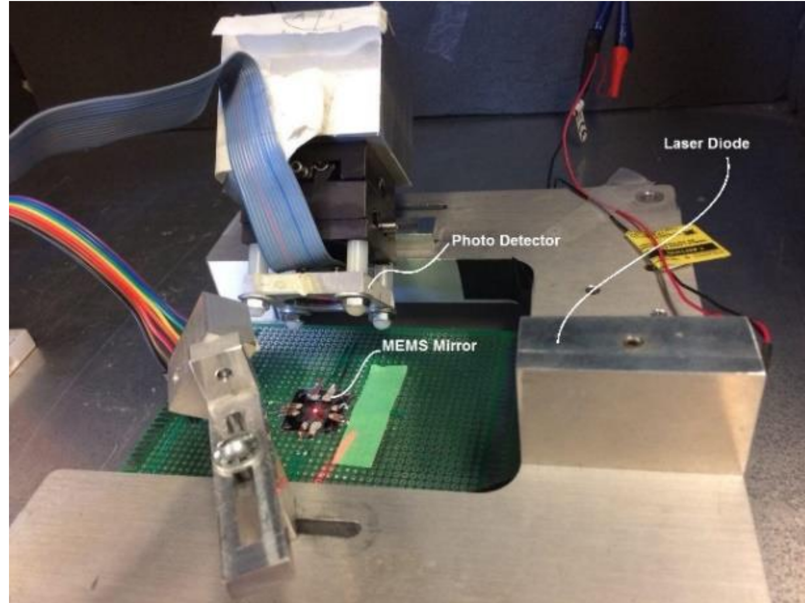

Fig. 7.1: Experimental setup used for characterizing the structure.

The results presented in this chapter has been published in [58].

7.1.1 Variation of the magnetic field

An AlphaLab gauss-meter model *G2* was used to measure the magnitude of the magnetic field. The magnetic field was measured to be 0.1 T at 1 cm over the center of the magnet where micro-mirror was located. However, when the micro-mirror is actuated, it lifts-up an additional 1 mm. In this section, some calculation is done to see the variation of the magnetic field along this axis due to the mirror lifting. The intensity of the magnetic field at the location of the mirror and springs was calculated as follows. Fig. 7.2 shows a schematic of the mirror located above the magnet at the distance z from it. At the location of the mirror and springs, the magnetic field is assumed to be uniform. This assumption was verified by calculating the strength of the magnetic field at different distances from the magnet using Equation 7.1 [61].

$$B_z = \frac{B_s}{\pi}\left(\tan^{-1}\left(\frac{LW}{2z(\sqrt{4z^2+L^2+W^2}}\right) - \tan^{-1}\left(\frac{LW}{2(z+T)\sqrt{4(z+T)^2+L^2+W^2}}\right)\right) \quad (7.1)$$

where B_s is equal to 1.3 T and denotes the maximum intensity of the magnetic field at the surface of the magnet (taken from the datasheet), L, W and T are the dimensions of the magnet shown in Fig. 7.2, z is the distance between the magnet and the mirror. Assuming that the mirror is located at a distance of 1 cm above the magnet center, the magnetic field is calculated to be 0.19 T. If the mirror is moved farther for 1 mm, the magnetic field at the new z distance (1.1 cm) is calculated to be 0.18 T. Therefore, the magnetic field strength has decreased for 4.5%. This change was ignored in this study.

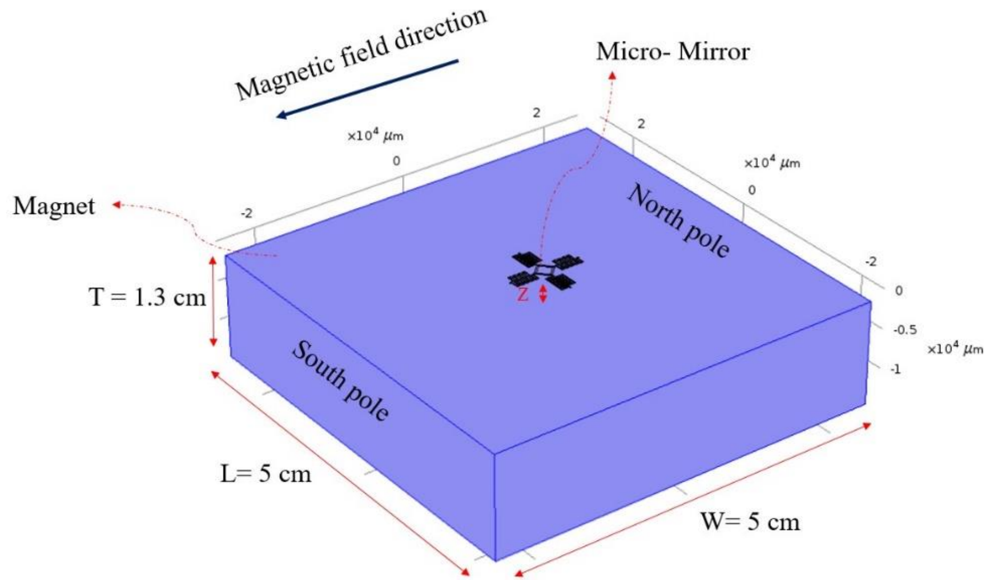

Fig. 7.2: Schematic of a magnet and the mirror on top of it, for calculating the magnetic field strength at different distances from the magnet surface.

7.1.2 Optical angle calculation

When a mirror tilts with a mechanical angle of θ_M, the light being reflected from it tilts with an optical angle θ_o. The optical angle can be measured by measuring the displacement of the laser spot on a screen. The schematic of the light rays reflected from a tilted mirror is shown in Fig. 7.3. The angle θ_i was the initial incident angle before the mirror tilts. In most of the experiments, it was set to be 45° with respect to the

normal to the substrate plane. When the mirror tilts, the normal to the substrate plane tilts with the same angle θ_M, therefore a new incident angle with respect to the mirror substrate is formed which is now equal to $\theta_M + \theta_i$. According to the reflection law, the reflection angle with respect to the mirror substrate is also $\theta_M + \theta_i$. Adding this value to the angle between the normal to the mirror surface and the normal to the substrate plane, a new reflection angle of $2\theta_M + \theta_i$ is obtained. In order to calculate the deflection amount of the laser beam, the difference between the tilted ($2\theta_M + \theta_i$) and un-tilted (θ_i) reflection angles was calculated which is equal to $2\theta_M$. Therefore, it can be concluded that the optical tilt angle is twice of the mechanical tilt angle of the mirror. In the results of this work, the optical tilt angle is presented.

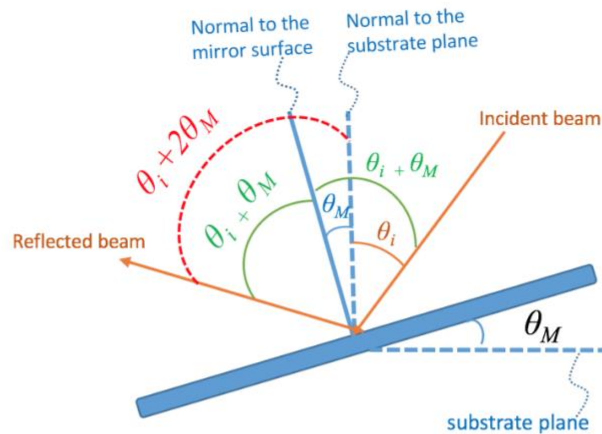

Fig. 7.3: Schematic of the light beams when the mirror is tilted.

Fig. 7.4 demonstrates how the optical angle was measured by measuring the displacement of the laser spot on the screen. Equation 7.2 was used to calculate the optical angle.

$$\theta_o = \tan^{-1}\frac{h_3}{d_2} - \tan^{-1}\frac{h_2}{d_2} \tag{7.2}$$

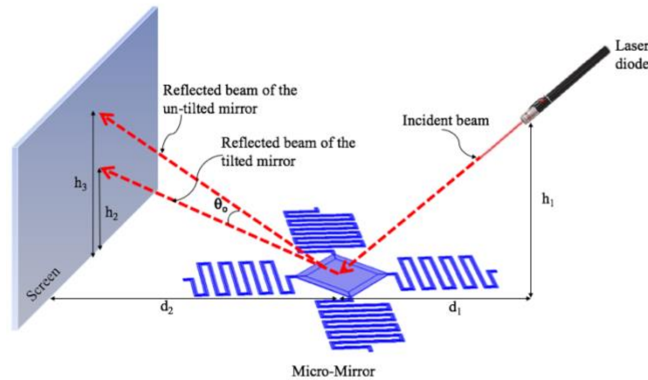

Fig. 7.4: Schematic of the setup for measuring the optical tilt angle.

7.2 Static response

In this section, the experimental behaviour of the mirror upon applying a dc current was explored. When the mirror is actuated by applying a dc current, the motion is of static type. On the other words, the mirror tilts and fixes at a certain angle. When the mirror tilts about the *y-axis*, laser spot moves vertically on the screen. In the same way, when the mirror tilts about the *x-axis*, the laser spot moves horizontally on the screen. By enabling different actuators, a variety of motions can be made.

To control and limit the current passing through the actuators a microcontroller system was used. A simple way of actuating the actuators was to connect a voltage, directly from a dc power supply to its terminals and control the current by changing the voltage. However, to simplify switching between the actuators, changing the direction of current and limiting the input current, a microcontroller system was designed and used. Block diagram of Fig. 7.5 shows the setup for applying dc current to the actuators.

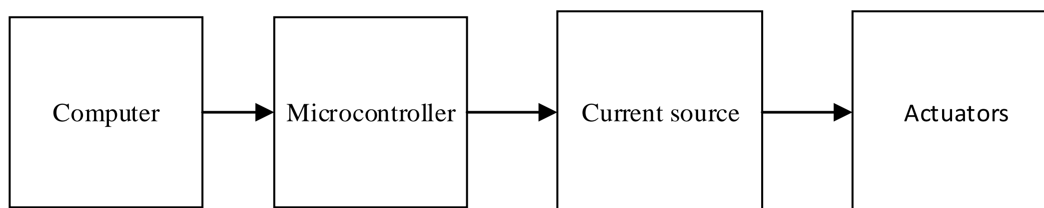

Fig. 7.5: Flowchart of actuating the mirror.

Fig. 7.6 shows the circuit schematic of the current driver. As shown in the figure, the system of current drivers consists of four parts including computer, microcontroller, current source, and actuators. The actuators to be enabled, and the direction of motion and the amount of current was set in the computer interface software and sent to the microcontroller using the serial port. The amplitude of current is controlled by changing the duty cycle of a Pulse-Width-Modulation (PWM) signal, generated by the microcontroller. The half-H driver (*SN7544*) receives the PWM signal from the microcontroller and provides bidirectional current for the actuators. Using this circuit, a current of 2 to 20 mA was applied to the mirror and the static tilt angle was measured.

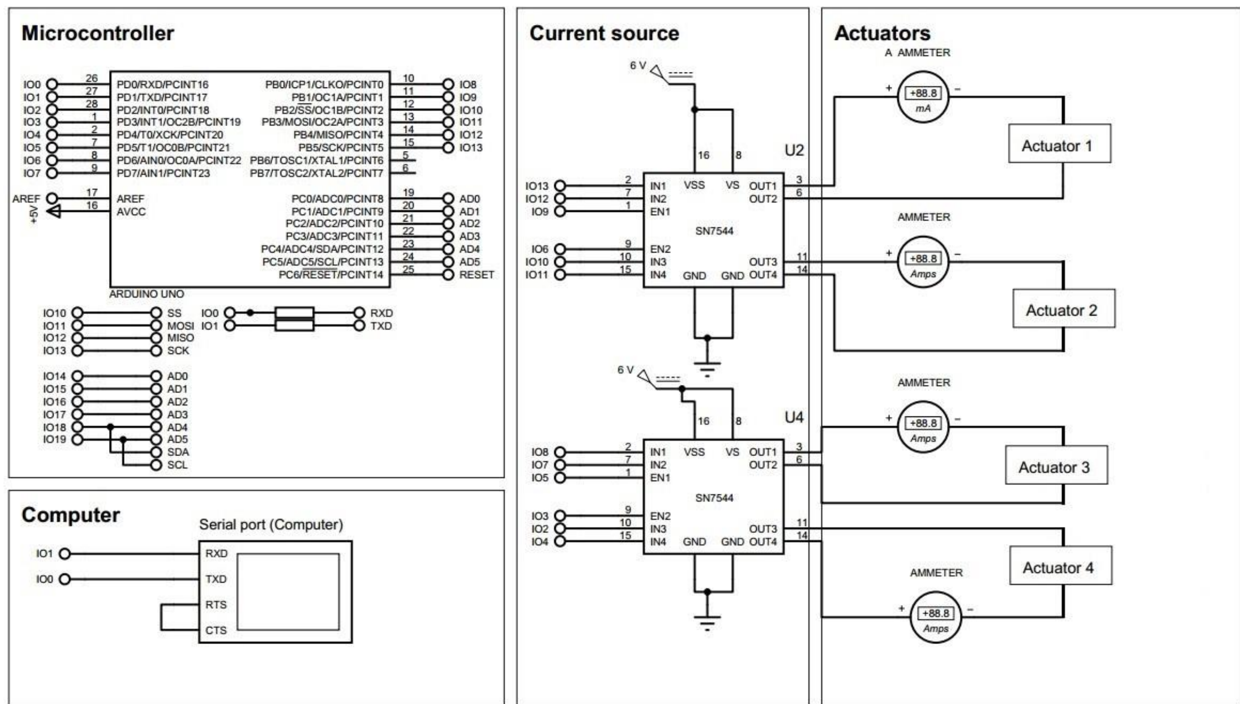

Fig. 7.6: Schematic of the setup used for generating dc current.

7.2.1 Static tilting

Fig 7.7 and Fig. 7.8 show the static tilt angles of the mirror about the *y*- and *x*-axes. From the graphs, it can be seen that for an input current of 18 mA, the static optical tilt angle about the *y-axis* was 12° and about the *x-axis* was 5.1°. To compare the experimental and simulated values, Fig. 7.7 and 7.8 also include

the FEM simulated values which were earlier demonstrated in section 4.3, Fig. 4.1 and Fig. 4.5. The increasing pattern of the tilt angle follows the simulated values, however, there are some differences. The reason of the difference between the simulated and experimental values will be discussed in section 7.3.1.

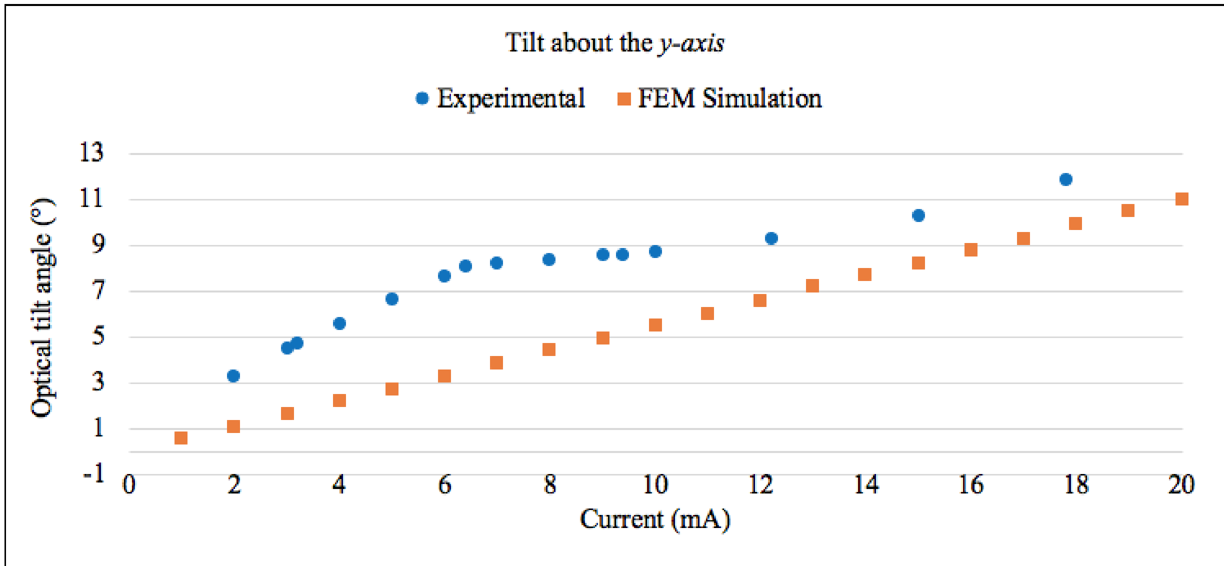

Fig. 7.7: Graph of the static optical tilt angle about the *y-axis* vs. applied current.

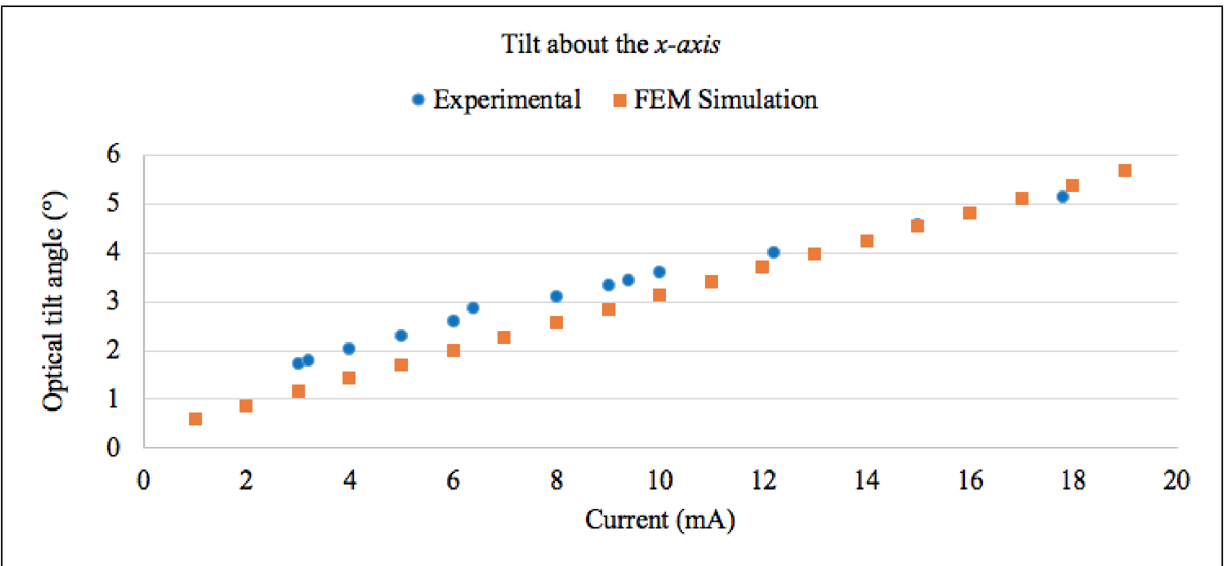

Fig. 7.8: Graph of the static optical tilt angle about the *x-axis* vs. applied current.

The *z-axis* translational motion was measured using an optical microscope. An objective lens of ×100 was focused on the center of the mirror. The mirror was actuated in the *z-axis*. While the mirror was lifted

up, the objective lens was focused again on the same point at the center. The change in the distance of the focal point is determined by the distance that the *z-axis* focus knob of the microscope stage is turned. This amount is equal to the height difference between these two points and recorded as the translational displacement in the *z-axis*. Fig. 7.9 shows the displacement versus applied current.

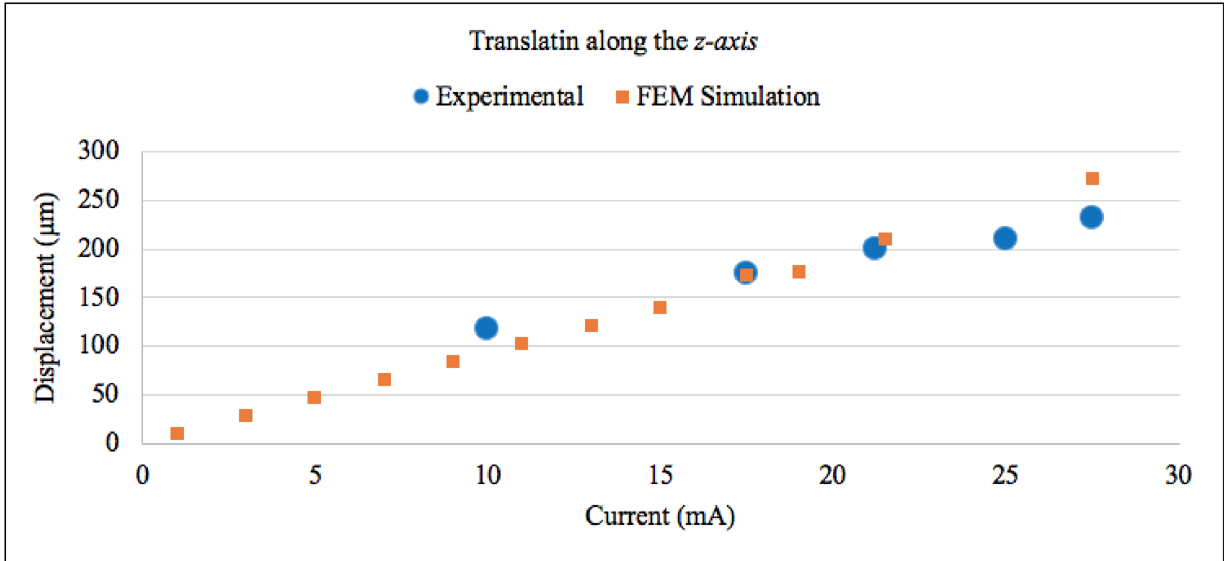

Fig. 7.9: Graph of the static optical tilt angle along the *z-axis* vs. applied current.

7.2.2 Step response

To measure the step response of the micro-mirror system, a current step-function rising from 0 to 34 mA was applied to the actuators when the mirror was tilting about *y-axis*. An oscilloscope was used to capture the output of the photodetector. The step response of the device while tilting about the *y-axis*, is shown in Fig. 7.10.

Earlier in Chapter 5, the transfer function of the system was found using a mass-spring model. From the graph of Fig. 7.10, it can be seen that the measured step response also demonstrates a second order system. Therefore, we can model the system accordingly. The transfer function of the system can be written as [59]:

$$G(S) = \frac{{\omega_n}^2}{S^2+2\xi\omega_n S+{\omega_n}^2} \tag{7.3}$$

where ω_n is the natural frequency and ξ is the damping ratio of the system. From the step response data of Fig. 7.10, the time between two peaks was read to be 4 ms. Therefore, the natural frequency is found to be:

$$\frac{2\pi}{\omega_n} = 4\,ms \rightarrow \ \omega_n = 1551.8\frac{rad}{s}\ or\ 247\ Hz \tag{7.4}$$

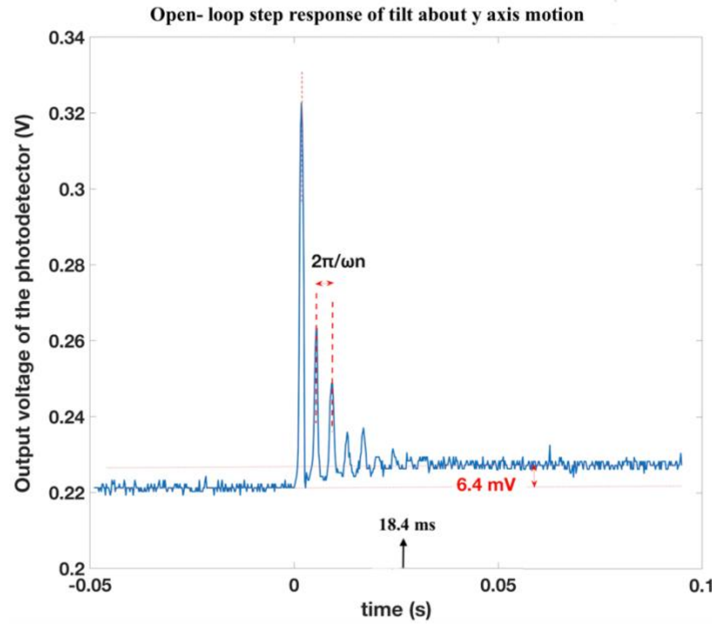

Fig. 7.10: Open-loop step response of the tilt about the *y-axis* motion.

The time when the first peak happens (the peak-time) was read to be 2 ms. The damping ratio or ξ of the system was calculated using the peak-time:

$$t_p = \frac{\pi}{\omega_n\sqrt{1-\xi^2}} \rightarrow \ \xi = 0.14 \tag{7.5}$$

The settling time was calculated using Equation 7.6:

$$t_s = \frac{4}{\xi_2\omega_n} = 18.4\ ms \tag{7.6}$$

Therefore, the transfer function of the system was written as Equation 7.7 for $\xi = 0.14$ and ω_n=1551.8 rad/s:

$$G(S) = \frac{(1551.8)^2}{S^2+434.5\ S+(1551.8)^2} \tag{7.7}$$

Earlier in Chapter 5, the values for some parameters of the system were calculated using a mass-spring model. Table 7.1 compares the values calculated using the mass-spring model and the values which

were experimentally measured. As can be seen in the table, the values are close to each other with a maximum difference of 11%, which validates the mass-spring model presented in Chapter 5.

Table 7.1: Comparing the calculated values with the experimentally measured values for the tilt-about-*y-axis* motion.

	Calculated values using the mass-spring model (presented in chapter 5)	Experimentally measured values	% difference
Resonant frequency	274.5 Hz	247 Hz	11%
Damping ratio	0.13	0.14	7%
Peak time	1.8 ms	2 ms	10%
Settling time	17 ms	18.4 ms	7.6%

7.3 Dynamic response

In the previous section, it was shown that when a dc current is applied to the actuators, the mirror tilts to a certain degree and the laser spot fixes on a point on the screen. In this section, the effect of applying an ac current to the actuators is studied. When an ac current is applied to the actuators, the laser spot on the screen dynamically moves.

7.3.1 Resonance frequency

The resonance frequency of the device was practically measured using the setup shown in Fig. 7.1. To measure the resonance frequency a sinusoidal wave of 50 mV_{p-p} amplitude was applied to the corresponding terminals of each motion. The frequency was swept between 1 Hz to 500 Hz. Fig. 7.11 shows a block diagram of the measurement setup.

The output of the photo diode's circuit was filtered using a lock-in amplifier (Stanford Research System SR830) to remove the noise of other frequencies. The output of lock-in amplifier was read using a digital multimeter (34461A Keysight Technologies).

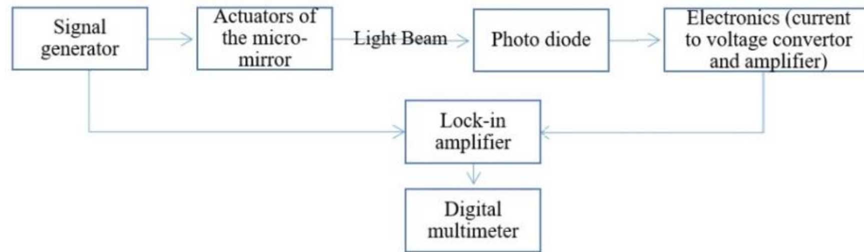

Fig. 7.11: Block diagram of the experimental setup for measuring the resonance frequency.

The resonance frequency of the *y-axis*, *x-axis* and *z-axis* motions were measured in three separate experiments. Fig. 7.12, Fig. 7.13 and Fig. 7.14 show the experimental resonance frequencies of the *y-axis* tilting motion. As shown in the graphs the resonance frequency occurred at 292.7 Hz for tilt about the *x-axis*, 247.5 Hz for tilt about the *y-axis* and 140 Hz for translation along the *z-axis*, where the mirror had the maximum displacement. The optical tilt angle at the resonance frequencies are summarized in Table 7.2.

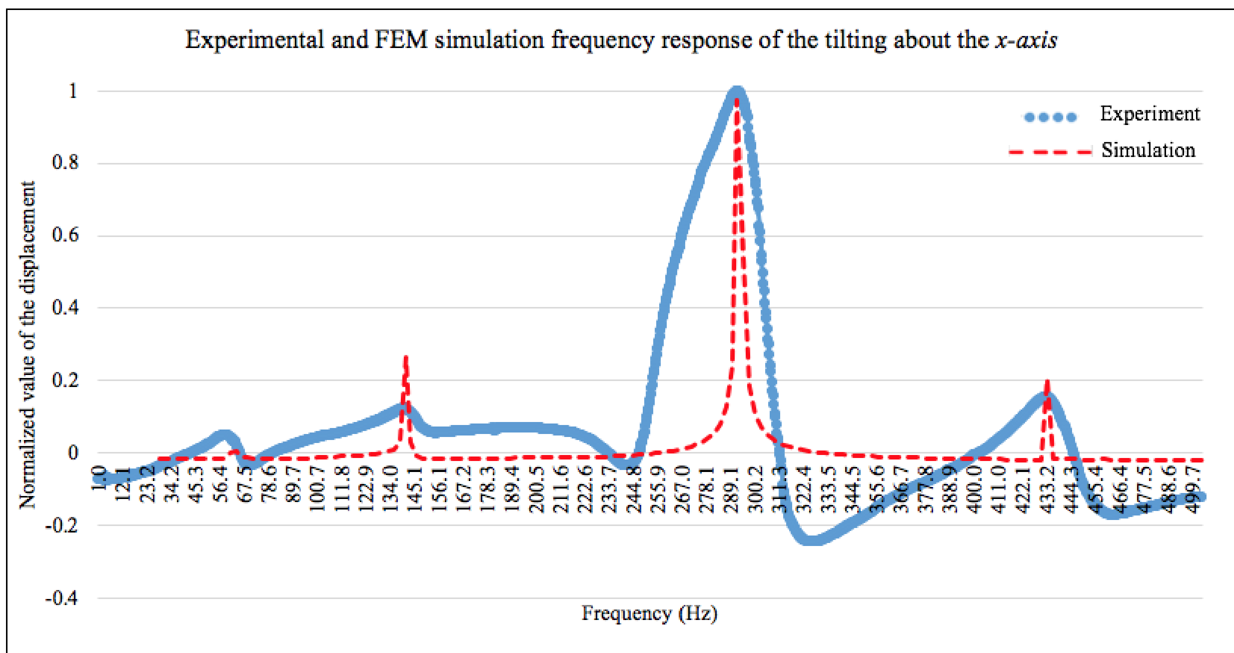

Fig. 7.12: Frequency response of the tilt about the *x-axis* motion. The experimental resonance frequency was at 292.7 Hz.

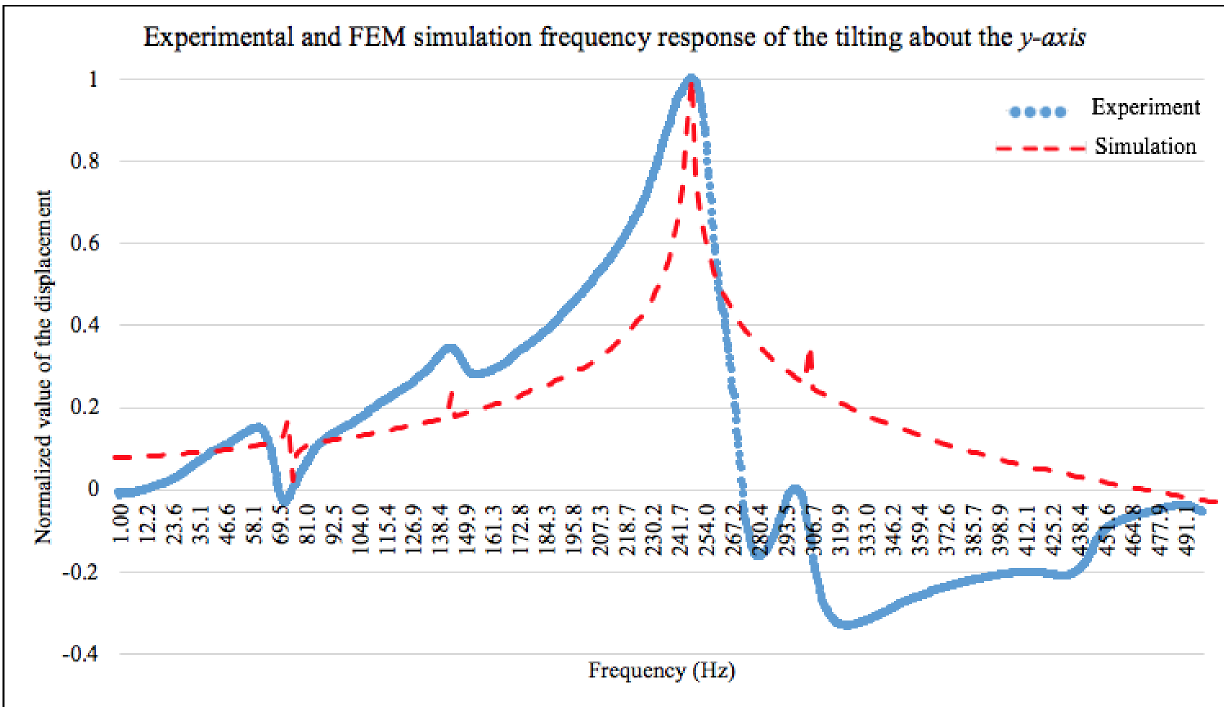

Fig. 7.13: Frequency response of the tilt about the *y-axis* motion. The experimental resonance frequency was at 247.5 Hz.

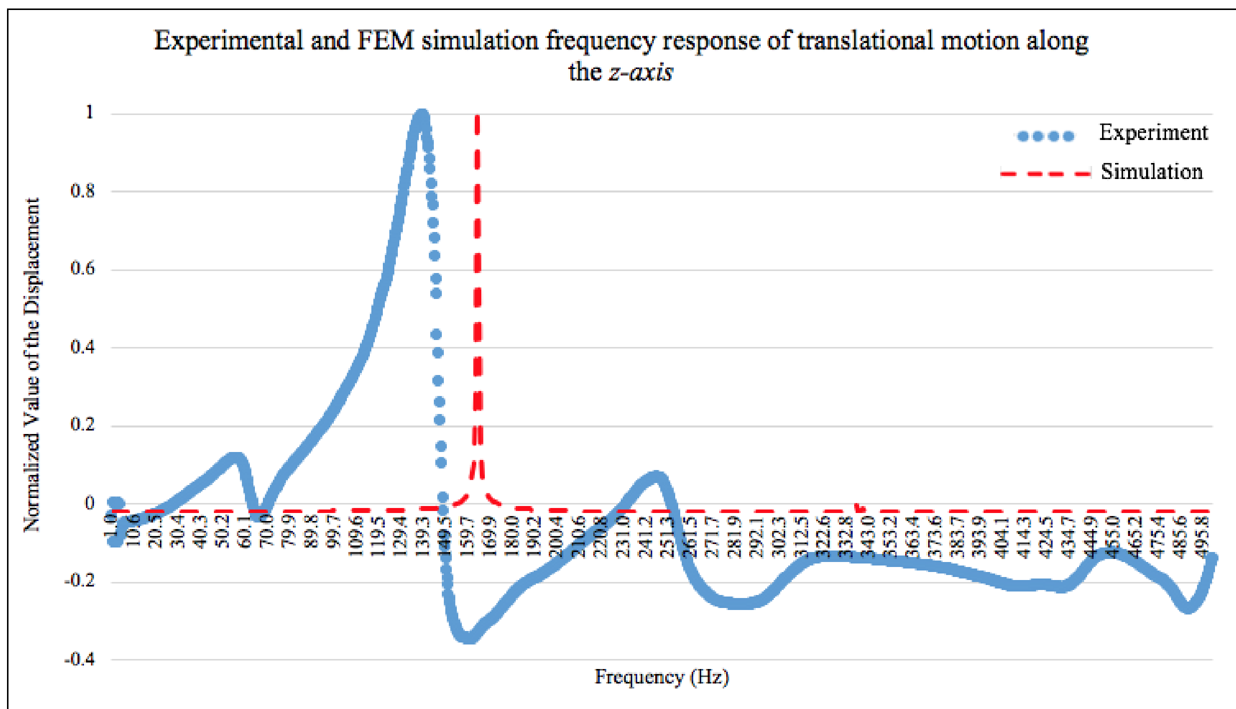

Fig. 7.14: Frequency response of the translational motion along the *z-axis*. The experimental resonance frequency was at 140 Hz.

The graphs of Fig. 7.12, Fig. 7.13 and Fig. 7.14 also include the FEM simulated graphs of the frequency response of the structure. The FEM simulated graphs which are shown with a red dashed line, were earlier demonstrated in Fig. 4.12, Fig. 4.13 and Fig. 4.14 of Chapter 4. From the graphs, it can be seen that the simulated values of the frequency peaks are close to the experimentally measured values, with a maximum difference of 16% which happens at the resonance frequency of the *z-axis*. The main reasons for the difference between the simulated and the experimental values in both static and dynamic experiments include:

1. *The uniformity of the magnetic field across the width of the magnet:* In the simulation the strength of the magnetic field is assumed to be uniform in the air. However, in reality, the strength of the magnetic field might vary across the length of the permanent magnet.
2. *The variation in the strength of the magnetic field along the z-axis:* In section 7.1.1 the variation of the strength of the magnetic field at 1 mm above the permanent magnet was discussed and calculated to be about 4.5%. This variation might also affect the amount of displacement, especially when moving along the z-axis. In the simulation, this variation has not been considered.
3. *The uniformity of the thickness of the silicon substrate:* At step 16 of the fabrication process, which was explained in Chapter 6, section 6.2, the silicon was etched to release the structure from the backside using an anisotropic plasma etching process. During the plasma etch process, the structure was rotated for a couple of times to have a uniform etch all over the surface. However, since the gas density might vary inside the etching chamber, the etch rate of silicon might be different. Therefore, the thickness of the silicon substrate might not be uniform across the structure. In simulation, this thickness is assumed to be uniform.
4. *The consistency of the Young's modulus of the material:* In the simulation, the Young's modulus of the silicon, aluminum and silicon dioxide are assumed to be constant in equilibrium condition. However, the real value of the Young's modulus of the fabricated material might be slightly different from the values used in the simulation. The Young's modulus can also vary with temperature as the structure heats up by joule heating.

The response of the tilting at the *x-axis* and the *y-axis* motions is shown in Figure 7.15. The light pattern on the screen was a vertical line for the *y-axis* tilt motion and a horizontal line for the *x-axis* tilting at the resonance frequencies shown in Table 7.2. Fig. 7.15 shows the light pattern when the mirror is tilting at its resonance about the *x-axis* (Fig. 7.15a) and about the *y-axis* (Fig. 7.15b).

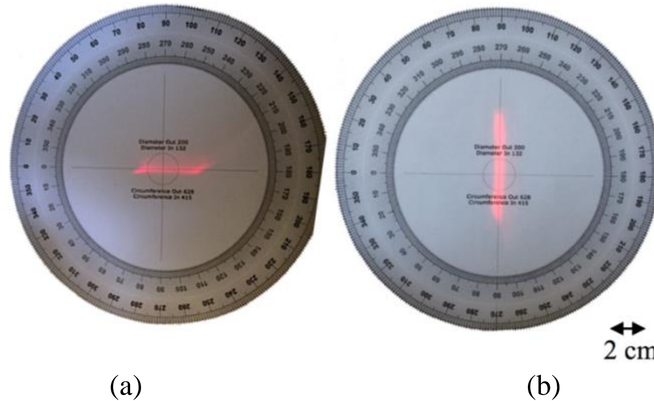

Fig. 7.15: The pattern of the reflected light from the mirror, when the mirror was tilting at its resonance frequency: a) 292.7 Hz for the *x-axis*. b) 247.5 Hz for the *y-axis*.

Table 7.2: Mechanical tilt angle and displacement of the *y-axis* and the *x-axis* tilt motions.

Motion type	Freq.	Power consumption / current (rms)	Amplitude of motion
Tilt about *y-axis (Vertical)*	247.5 Hz	2.6 mW/ 20 mA	22.8º
Tilt about *x-axis (Horizontal)*	292.7 Hz	2.6 mW/ 20 mA	13.3º

7.3.2 Dynamic deformation of the mirror

The propagation paths of the reflected rays from the mirror is affected by the flatness of the mirror surface. The light beam reflected from a deformed mirror is scattered, and so it travels in different directions. This phenomenon results in a blurry spot on the screen. Therefore, a mirror is desired to have the minimum deformation on its surface. The symmetrical geometry of the mirror and the fabrication process was developed in the way to avoid possible deformation on the mirror surface. However, the fabricated mirror is not perfectly flat. The static deformation of the mirror was earlier discussed in chapter 6. In this section, the dynamic deformation of the mirror is discussed below.

When the mirror is tilting with a high frequency, another type of deformation known as dynamic deformation might occur. In a tilt motion, there are alternating forces on both halves of the mirror. Due to these forces, an acceleration is applied to the mirror that might mechanically bend the mirror surface. To calculate the maximum dynamic deformation for a rectangular shaped mirror, Equation 7.8 was used [59, 61, 62].

$$\delta = \frac{0.288\,\rho\theta_0\omega^2 L^5}{Et^2} \tag{7. 8}$$

where δ is the dynamic deformation, L is the half-length of the mirror, ω is the tilting frequency, θ_0 is the mechanical tilt angle of the mirror, ρ is the material density, E is the Young's modulus of the mirror material and t is the thickness of mirror. δ is calculated to be:

$$\delta = \frac{0.288\left(2400\frac{kg}{m^3}\right)\left(11.4^\circ \times \frac{\pi}{180}\right)(2\pi \times 247.5\,Hz)^2(1.1\,mm)^5}{(1.44 \times 10^{11}\,Pa)\,(1.6 \times 10^{-6}\,m)^2} = 1.4 \times 10^{-6}\,\mu m$$

Therefore, for a mirror tilting about *y-axis* with a mechanical tilt angle of 11.4° at a frequency of 247.5 Hz, the dynamic deformation was calculated to be 1.4 µm. This amount is 0.07% of the mirror side length (2 mm).

To check if the value calculated for the dynamic deformation is reasonable, the resonance of the mirror and spring elements were compared. Using a COMSOL simulation, values for the resonance frequency of the mirror was found to be 2258 Hz, and the resonance frequency of the spring was found to be 214.5 Hz. The overall resonance frequency of the system tilting about the *y-axis* was experimentally measured to be 247.5 Hz. This experimentally measured value is close to the spring resonance frequency value. However, the resonance frequency of the mirror itself (2258 Hz) is almost 9 times higher than the experimental resonance frequency of the system (247.5 Hz). Therefore, the small dynamic deformation on the mirror is reasonable, since the mirror is resonating at a much lower frequency.

7.3.3 Mode coupling effect

When an ac current is applied to the actuators and the mirror is dynamically moving, the shape of the motion of the mirror plate and consequently the pattern of the laser spot on the screen strongly depends on the frequency of the input current. The theory of this fact was earlier discussed in chapter 5 (5.3.3) where we explored the light pattern can differ from a straight line to a complex pattern.

The forces applied to the mirror sides or the springs are intended to make a specific motion. For example, tilting about the *x-axis* is made by the force setting of Table 3.2. This motion happens when spring numbers 1 and 2 have out-of-plane motion in the *z-axis* and springs number 3 and 4 have torsional motion about the *x-axis*. However, in some specific frequencies, the springs number 3 and 4 might have different types of motion, with the same configuration of forces. It happens when the input frequency meets the harmonics of the resonance frequencies of those springs. This phenomenon results in some patterns of light on the screen.

An experiment was done to study the effect of the *y-axis* resonance frequency on the motion of the *x-axis*. In this experiment, the mirror was actuated to tilt about the *x-axis*, while the frequency of the input signal was set to the y-axis resonance frequency (247.5 Hz).

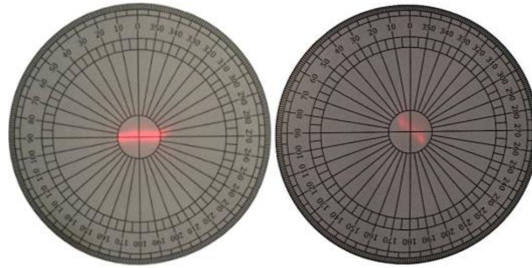

Fig. 7.16: (a) Pattern caused by driving θ_x at its resonance of 292.7 Hz. (b) Pattern caused by driving θ_x at θ_y's resonance of 247.5 Hz.

Fig. 7.16a shows the light pattern when the mirror is tilting about the *x-axis* at its resonance frequency of 292.7 Hz (*x-axis* resonance), while in Fig. 7.16b the input frequency is 247.5 Hz (*y-axis* resonance). The light pattern was approximately 40° tilted. Fig. 7.16b shows that the motion of *y-axis* is contributing in the motion of the *x-axis* when the frequency is close to the resonance frequency of the *y-axis*.

The harmonic of elliptical shape (purple dashed line) that can be seen in Fig 5.4, was experimentally demonstrated by driving the mirror to tilt about the *y-axis* in the resonance frequency of the *z-axis* which is 140 Hz. Fig. 7.17 shows this elliptical mode.

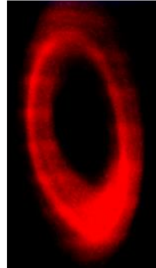

Fig. 7.17: Pattern caused by driving θ_y at 140 Hz.

The analytical results were compared with the practical results. An elliptical pattern of motion was also created as a result of the mode coupling between different types of motions which was discussed in this section. In conclusion, the mirror can scan horizontally or vertically when the θ_x or θ_y are actuated at their resonance frequencies respectively. The dominant motion at these frequencies results in the horizontal or vertical patterns on the screen. However, if an elliptical scanning pattern is desired, the mirror should be actuated in tilting about the *x*- or *y-axes* while in the resonance frequency of the *z-axis*.

7.3.4 Raster Scan

A raster scan was generated by driving one axis at resonance mode and the other axis at a lower frequency. A raster scan pattern is shown in Fig 7.18. This pattern was made by enabling vertical scanning (*y-axis* tilting) at 40 Hz and horizontal scanning (*x-axis* tilting) at its resonance frequency 292.7 Hz.

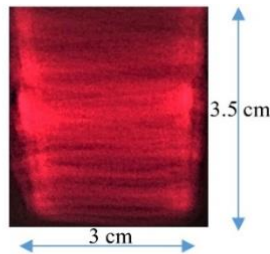

Fig. 7.18: Raster scan pattern generated by vertical axis tilting at 40 Hz and horizontal axis resonating at its resonance frequency 292.7 Hz.

7.4 Comparison with other works

Table 7.3 summarizes some electromagnetically actuated large-tilt-angle MEMS-mirrors published by other groups. The details of these works were earlier discussed in Chapter 2. From the Table, it can be seen that most of the electromagnetically actuated micro-mirrors are of 2 degrees of freedom. A 3-DOF micro-mirror was presented by Cho et al. [26], however, it requires greater power consumption. A figure of merit was defined as the ratio of the optical tilt angle to the consumed power which is shown in Table 7.3. The calculated FOM shows the high performance of this micro-mirror. The other works listed in Table 7.3 do not provide 3-DOF motion [51, 52].

Table 7.3: Comparing the characteristics of the electromagnetically actuated MEMS mirrors in the literature.

Ref. No.	Mirror size	Actuation force	DOF static / dynamic	Optical tilt angle / displacement	Power / current	FOM: $\frac{Opt.\ tilt\ angle(°)}{power\ (mW)}$
This work	2 mm × 2 mm	EM (MC) B = 0.1 T	3 S-D	22.8°, 13.3° at resonance z = 232 µm	2.6 mW / 20 mA 86.9 mW / 110 mA	8.7
Cho et al. [26]	900 µm × 900 µm	EM (MC) B = 0.16 T	3 S-D	±4.2°, ±9.2° z = ±42 µm	345-360 mW	0.03
Makishi et al. [49]	8 mm × 4 mm	EM (MM)	2 S-D	118°	250 mA	0.47
Yalcinkaya et al. [53]	1.5 mm	EM (MC)	2 D	65°, 53° at resonance	150 mA	0.43
Sung et al. [55]	~ 1 mm	EM (MM & MC)	2 D	20° at resonance	10 mW	2
Jeong et al. [54]	3 mm × 1.5 mm	EM (MC)	2 D	30° at resonance	60 mW	0.5
Ataman et al. [50]	4 mm × 4 mm	EM (MM)	2 S-D	±16°	5.12 W	0.003
Raboud et al. [52]	1 mm × 1 mm	EM (MC)	1 S-D	25° at resonance	10 mW	2.5
Ji et al. [51]	1.5 mm	EM (MC)	2 S-D	8.8°, 8.3° at resonance	16.7-26.3 mW	0.41

EM: Electromagnetic, **MC**: Moving coil, **MM**: Moving magnet, **DOF**: Degree of freedom, **S**: Static, **D**: Dynamic, frequency, **B**= Magnetic Field

To compare the performance of the micro-mirrors which are reported in Table 7.3, the graph of Fig. 7.19 was plotted. The axes are plotted in logarithmic scale. In order to show the smaller mirror size and the lower power consumption farther from the center, the values of power consumption and mirror size were

inverted. The micro-mirror developed in this thesis is shown by a red solid line in Fig. 7.19. Comparing to the other works, this micro-mirror provides displacement in 3 dimensions, while still offering a lower power consumption and a large tilt angle.

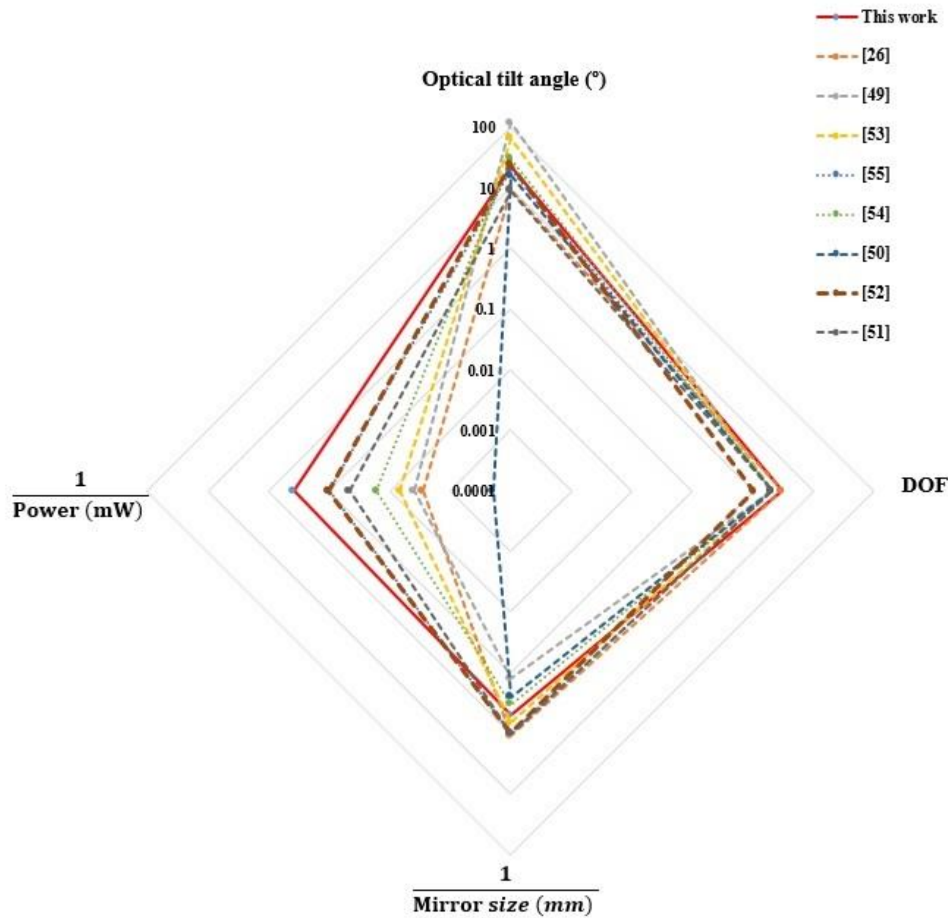

Fig. 7.19: Radar plot of the micro-mirrors reported in Table 7.3.

7.5 Summary and conclusions

In this chapter, the test results of the fabricated micro-mirror were presented. The micro-mirror was tested in the static (by applying a dc current) and dynamic (by applying an ac current with different frequencies) modes of operation. A large tilt angle with respect to the input power in 3 degrees of freedom was demonstrated. The step response and the frequency response of the device were analyzed. The

Lagrange's equations which were earlier solved for the micro-mirror system in Chapter 5, were used to describe the mode coupling and harmonics of the dynamic response. By actuating the micro-mirror in two axes, one at resonance and the other one at low-frequency motions, a raster scan was done. The results were compared with the other work and the advantages and disadvantages were discussed.

8

Fabrication Method for Distributed Bragg Reflectors

Contents

8.1 Introduction 95

8.2 Background of Depositing Materials with a Specific Refractive Index 97

8.3 Experimental Details 99

8.4 Statistical Model for Refractive Index Determination 103

8.4.1 Surface Fitting 104

8.4.2 Implementing the GA 107

8.4.3 Experimental Verification of the GA Results 111

8.5 Distributed Bragg Reflector 112

8.5.1 DBR Background and Design 112

8.5.2 DBR Fabrication by Reactive Sputtering of Silicon 114

8.6 Summary and Conclusions 117

8.1 Introduction

In some applications like solar cells and anti-reflection coatings, thin films with specific refractive index play an important role. However, fabricating films that possess a specific refractive index is not straight forward. In this chapter, an easy-to-implement method for fabricating films of SiO_x with a specific

refractive index is presented. The method includes a statistical model that can determine the reactive sputtering deposition parameters to get a specific refractive index. This method determines what should be the deposition pressure and the oxygen partial flow in order to deposit an SiO_x layer which has a specific refractive index. Three studies were undertaken for this work.

- First, several reactively sputtered SiO_x thin films were deposited from a silicon target at varying pressure and reactive gas flow. This was done to provide a suitable range of stoichiometry for statistical study. Three deposition pressure ranges (low range from 1.4 - 1.7 mTorr, medium range 8.5 - 10 mTorr, and high range 15 - 17 mTorr) were set and the oxygen partial flow was varied between 1% and 11% for all the three pressure ranges. The films deposited had a wide range of refractive index from 1.48 to 4.28.
- Second, after the data of pressure, oxygen partial flow and refractive index was collected, the statistical model was developed. The statistical model demonstrates how the two sputtering parameters (oxygen partial flow and pressure) affect the refractive index.
- Third, a genetic algorithm (GA) was developed to determine the required oxygen partial flow and pressure needed to deposit SiO_x layers with a specified refractive index.

The effectiveness of this statistical model method was demonstrated by calculating the required deposition conditions needed to fabricate a distributed Bragg reflector (DBR) from alternating layers of high and low refractive index SiO_x. A high reflection of 95% in the visible and near-infrared region from 730 nm - 1000 nm (270 nm band) was demonstrated by the fabricated DBR. The results of this study have been reported in reference [64]. A modified version of this method has also been employed to determine the deposition conditions for fabricating Indium-Tin-Oxide (ITO) thin films with specified refractive index while possessing acceptable electrical conductivity and optical transmittance [65].

8.2 Background of depositing materials with a specific refractive index

There are four common methods for fabricating materials with an arbitrary refractive index which do not inherently exist in nature. The first method is the co-deposition of two (or more) materials simultaneously, forming a material with new properties. The refractive index of the deposited film can be adjusted by the relative deposition rate of each material component. For example, SiO_2 and TiO_2 can be deposited using co-sputtering technique onto a substrate to make a thin film of a specific refractive index [29]. Molecular beam epitaxy is also used for such controlled co-deposition. The second method is to deposit a low-density version of a given material to reduce its refractive index. This can be done by various methods. Glancing Angle Deposition (GLAD) [30, 65, 66] is one such method, where a material is thermally evaporated at an oblique angle and the wafer is also rotating during deposition. The angle of incident vapour determines the porosity of the deposited film, and so its refractive index. The third method is depositing a structure which is composed of multi-stack layers. The layers are made of high and low refractive index materials. The thickness of each layer should be much less than the wavelength of the incident light. Therefore, the multi-stack layer can be considered as a single homogenous material. The optical thickness of each layer is used to calculate the equivalent refractive index of the material. By varying the thickness of each material, the equivalent refractive index can be controlled [67, 29].

The above co-deposition and multi-layer structure methods require two or more materials to make a film of arbitrary refractive index. The GLAD process requires a vacuum system of specific design, and is limited to materials that can be thermally evaporated. These require more specifically designed vacuum deposition systems.

The fourth method is the deposition of a single material combined with a reactive gas, in order to achieve a specific stoichiometry and so achieve a specific refractive index. This can be done by reactive sputtering [68, 69, 70, 71] or chemical vapor deposition (CVD) [73] methods. Unlike the other methods, in this method, the material with an arbitrary refractive index is made from a single source material. A wide range of refractive indices can also be created by this method.

S. Khodier et al. [74] compared the effect of deposition method on the refractive index of deposited silicon dioxide films. Three studies were conducted in which SiO_2 was deposited by electron beam evaporation, sputtering, and chemical vapor deposition methods. Among these methods, the sputtered films had the highest refractive index range, varying from 1.51 – 1.59. The formation of non-stoichiometric compounds could be one reason for the higher refractive index. For example, depositing silicon and oxygen together can result in a film that includes Si, SiO and SiO_2 compositions. The other advantage of reactive sputtering is that sputtering can be done at a lower temperature, in contrast to thermal evaporation (and GLAD method) and CVD techniques. A lower temperature deposition can result in deposited films with lower thermal stress.

Various groups have explored reactively sputtering of SiO_x films. However, depositing a thin film with a specific refractive index may need a significant effort. There are many process parameters that change the stoichiometry of the deposited material. Finding the relationship between those process parameters and the refractive index of the deposited film is challenging.

Wu et al. in [70] and Chichibu et al. in [71] separately studied the effect of oxygen partial flow on the refractive index of the sputtered SiO_2. These two studies reported different results on this effect. In the study reported by Wu et al.[70], SiO_2 was reactively sputtered from a silicon target and the effect of varying oxygen partial flow on the refractive index of the film was investigated. These experiments were done at a working pressure of 6 mTorr with an RF power of 100 W. The oxygen partial flow was varied from 10% to 20% which resulted in refractive index rising from 1.46 to 1.53 with increasing oxygen partial flow. In the study reported by Chichibu et al. [71], the result was contradicting. They found that the refractive index of the deposited film decreases with increasing the oxygen partial flow. These experiments were done at a working pressure of 1.5 mTorr with an RF power of 300 W. The oxygen partial flow was varied from 10% to 60% which resulted in refractive index decreasing from 1.47 to 1.46 with increasing oxygen partial flow.

From the above works, it can be concluded that it is challenging to predict the effect of a reactive sputtering parameter, in the refractive index of the final deposited SiO_x film. Mathematical modeling of the deposition process in the reactive sputtering system could be one solution for that. Various groups have

developed theoretical models for the reactive magnetron sputtering process [74,75,76,77]. However, specifically predicting the deposition parameters for a specific refractive index is still an issue. The model developed by Palmero et al. [75] included plasma chemistry models, electromagnetic models, electron kinetic equations, and sputtering models. They found a mathematical relationship between the deposition rate, deposited silicon oxide film stoichiometry and the sputtering parameters. These parametric models are of high complexity and can be used to find parameters like stoichiometry of the deposited film and deposition rate of the thin film. However, they cannot be used to specifically determine the deposition parameters for a specific refractive index.

These techniques can be augmented by employing in-situ monitoring of the refractive index of the film as it is being deposited. This can be implemented by mounting an ellipsometer in the vacuum system [79], which can be challenging. One difficulty of this method is with the beam alignment and calculating the refractive index. Since the thickness of the film is changing, the laser beam which is used to measure the refractive index can easily be misaligned. These issues make the in-situ monitoring of the refractive index practically challenging.

In the following sections, the details of a statistical model for determining the deposition parameters for fabricating films with a specific refractive index is presented.

8.3 Experimental details

Silicon wafers of p-type and (100) orientation were used as substrates for depositing SiO_x. The silicon wafers were cleaned by immersing in piranha solution (4:1; conc. H_2SO_4/H_2O_2) for 10 minutes to remove organic residues. After that, the wafers were immersed in a BOE solution (6:1; NH_4F/HF) for 2 minutes to remove the native oxide.

The SiO_x thin films were deposited using a 13.56 MHz RF magnetron sputtering system with an RF power of 200 W. A silicon target of 99.999% purity was placed above the substrate in a vertical distance of 6 cm. The base pressure of the sputtering chamber was 3.7×10^{-6} Torr before starting the deposition.

Plasma was generated using ionized argon gas and oxygen was used as the reactive gas. Two mass flow controllers were used to adjust the flow rate of high purity argon and oxygen gases introducing into the chamber. All the samples were deposited for 10 minutes.

SiO_x samples were deposited in a total of 18 experiments. These 18 experiments were done in 3 different groups of pressure: 6 samples were deposited at a low pressure range from 1.4 – 1.7 mTorr, 6 samples were deposited at a medium pressure range from 8.5 – 10 mTor and 6 samples were deposited at a high pressure range from 15 – 17 mTorr. At each pressure range, the oxygen partial flow was varied between 1% to 11%.

Table 8.1 shows a summary of deposition parameters and the measured refractive index for 18 samples. In order to cover a wide range of reasonable deposition conditions, the values for oxygen partial flow and the deposition pressure range were selected based on the values reported in [69, 70, 74, 79, 80, 81]. An ellipsometer (J. A. Woolam model M-2000D) was used to measure the refractive index of the films. The refractive index was measured at a reference wavelength of 632.8 nm, which is considered as a standard wavelength of refractive index measurement [83]. In all the experiments, the refractive index was measured at three different points of each sample, and the average value of the real parts was recorded. The optical losses were ignored in this study, since the imaginary part of the refractive index in dielectrics is almost zero because they have very low losses in near-infrared and optical wavelengths [28].

Table 8.1: Deposition parameters and the measured refractive index of sputtered SiO_x films for 18 different samples.

Pressure Range	Sample	Ar flow rate (sccm*)	O_2 flow rate (sccm)	$O_2/(O_2+Ar)$	Pressure (mTorr)	Refractive index
High	1	80	0.8	1%	15	1.51
	2	80	2.5	3%	16	1.52
	3	80	4.2	5%	16	1.53
	4	80	6.0	7%	16	1.49
	5	80	7.9	9%	17	1.48
	6	80	9.9	11%	17	1.49
Medium	7	50	0.5	1%	8.5	2.03
	8	50	1.5	3%	9	2.00
	9	50	2.6	5%	9.1	1.48
	10	50	3.8	7%	9.2	1.49
	11	50	4.9	9%	9.7	1.50
	12	50	6.2	11%	10	1.50
Low	13	20	0.2	1%	1.4	4.28
	14	20	0.6	3%	1.5	3.30
	15	20	1.1	5%	1.5	3.40
	16	20	1.5	7%	1.4	3.37
	17	20	2.0	9%	1.6	3.08
	18	20	2.5	11%	1.7	2.07

*sccm: standard cubic centimeters per minute

The graphs of Fig. 8.1 and Fig. 8.2 are plotted based on the values of Table 8.1. Fig. 8.1 shows how the refractive indices of the experimentally deposited SiO_x films change with the pressure for different oxygen partial flow rates. From the graphs of Fig. 8.1 it can be seen that the refractive index decreases by increasing the system pressure at a given oxygen partial flow. At high pressures, the mean free path of atoms is shorter than at low pressures, and so a large number of collisions happen between the gas molecules and target atoms. These collisions cause the deposited film to be more porous, which reduces the refractive index [69, 83]. For all oxygen partial flow levels from 1% to 11%, this trend was almost true.

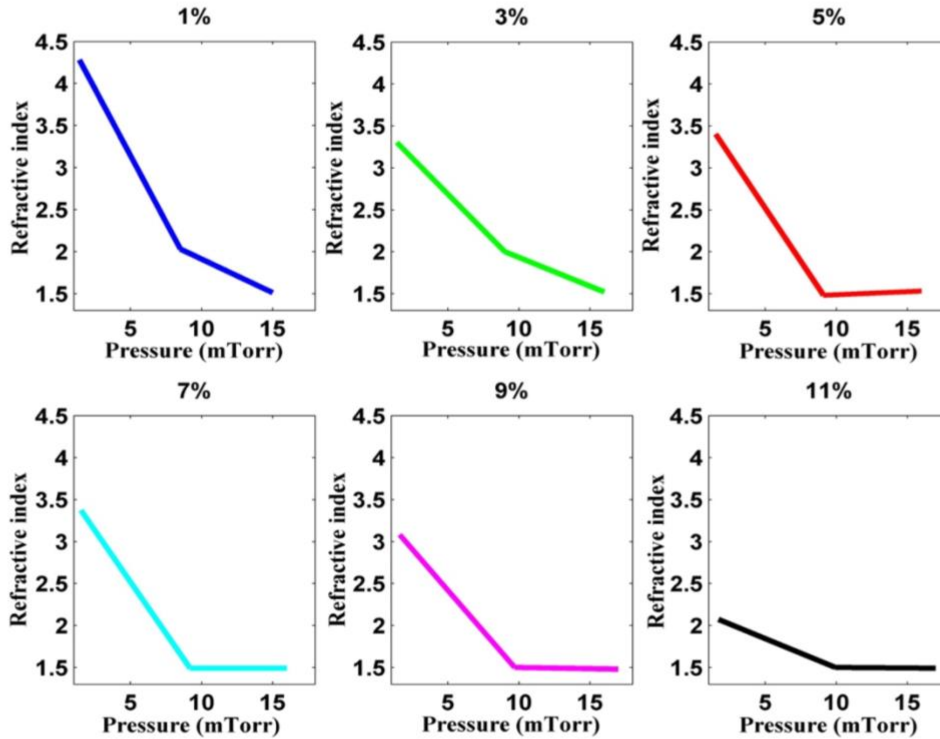

Fig. 8.1: Measured refractive index of the sputtered SiO_x versus deposition pressure for different oxygen partial flows (O_2/ (O_2+Ar) = 1% to 11%).

The variation of the refractive index of the deposited films versus oxygen partial flow, at three different pressures is shown in Fig. 8.2. Increasing the oxygen partial flow reduces the refractive index in low and medium system pressures. By increasing the oxygen partial flow more oxygen atoms are available to react with the silicon atoms. At lower deposition pressures, the effect of oxygen partial flow is very significant (Fig. 8.2a). At medium pressures, the slope is smoother (Fig. 8.2b). At higher deposition pressures (Fig. 8.2c), the slope is almost constant with small fluctuations. This happens because at high pressures, even small amounts of oxygen (O_2/ (O_2 + Ar) = 1%) results in a very low refractive index. These results also support the research reported by Wu et al. in [70].

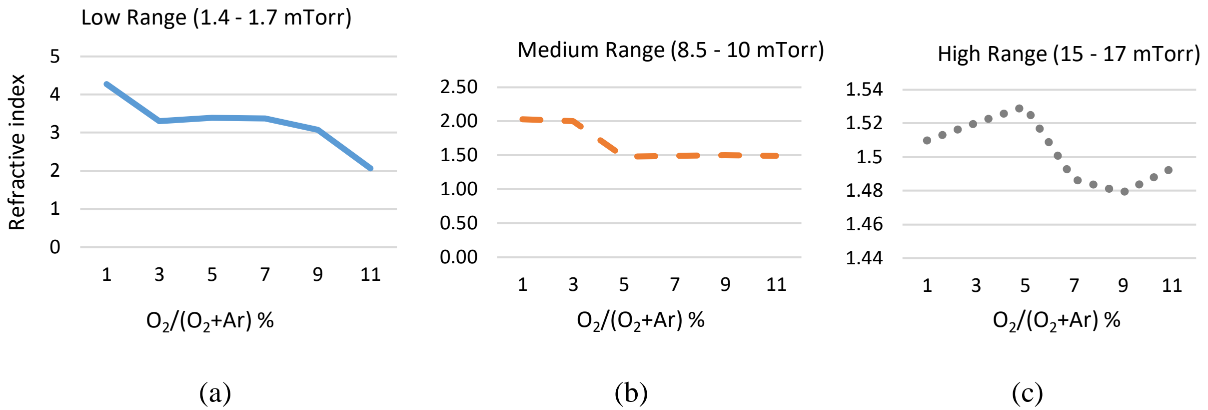

Fig. 8.2: Measured refractive index of the sputtered SiO_x versus oxygen partial flow in three different pressure levels.

8.4 Statistical model for refractive index determination

From Table 8.1 we can see that the process parameters of oxygen partial flow and pressure can change the refractive index of the deposited film in a wide range. In order to predict the process parameters for an arbitrary refractive index, a relationship between the refractive index and the deposition parameters needs to be established. Since we are relating the refractive index to two variables (oxygen partial flow and pressure), a 3D surface was applied to the data. In fact, the statistical model of knowledge gained from prior processes was made by this 3D surface.

A genetic algorithm (GA) was then developed to determine the deposition parameters for making a film with a new refractive index (not previously deposited) from the statistical model. A GA was used since it can calculate the process parameters in a short time and is an established method in finding optimized solutions. Various groups have used GA to optimize sputtering system process parameters for depositing different materials [84, 85, 86]. For example, in the study reported by Lin et al. [85], a GA was implemented to determine the sputtering power and nitrogen flow rate for fabricating films with specific absorption coefficient in solar cells. They have concluded that their proposed method is beneficial in saving energy and time in the process line of solar cell manufacturing. In this work, the process parameters of pressure

and oxygen partial flow are the ones that will be determined for depositing a thin film with a specified refractive index.

8.4.1 Surface fitting

A polynomial regression method was implemented in order to determine the 3D fitness function surface. It was assumed that a polynomial of degree 2 for both the process variables will suitably represent the surface. The accuracy of this assumption will be discussed later. The polynomial relation for the fitness function is shown in Equation 8.1.

$$\hat{z} = p_{00} + p_{10}x + p_{01}y + p_{20}x^2 + p_{11}xy + p_{02}y^2 \quad (8.1)$$

where y represents the pressure, x represents the oxygen partial flow, $\hat{z}$ represents the calculated refractive index, and p_{00}, p_{10}, p_{01}, p_{20}, p_{11}, p_{02} are the six coefficients of the polynomial terms.

A least square method was used to calculate the six coefficients of the fitness function. This method calculates the deviation between measured values (z_i) of the refractive index (for each data point in Table 8.1) and predicted ($\hat{z}_i$) refractive index value. This method was performed over all experimental data points of Table 8.1. Sum of Squared Errors (SSE) is as 8.2,

$$SSE = \sum_{i=1}^{n}(z_i - \hat{z}_i)^2 \quad (8.2)$$

where $\hat{z}_i$ is the predicted value (fitted value), z_i is the observed value of refractive indices (from Table 8.1), and n equal to 18 is the number of experiments in Table 8.1. Substituting $\hat{z}_i$ in the SSE we have (8.3):

$$SSE = \sum_{i=1}^{n}(z_i - (p_{00} + p_{10}x_i + p_{01}y_i + p_{20}{x_i}^2 + p_{11}x_iy_i + p_{02}{y_i}^2))^2 \quad (8.3)$$

By taking the partial derivative of the SSE equation with respect to each of the coefficients, and setting it to zero, the coefficients can be found. Equations 8.4 and 8.5 illustrate using least square method for calculating the first coefficient.

$$0 = \frac{\partial SSE}{\partial p_{00}} = \sum_{i=1}^{n}(-2)(z_i - p_{00} - p_{10}x_i - p_{01}y_i - p_{20}{x_i}^2 - p_{11}x_iy_i - p_{02}{y_i}^2) \quad (8.4)$$

Solving we obtain:

$$\sum_{i=1}^{n} z_i = np_{00} + p_{10}\sum_{i=1}^{n} x_i + p_{01}\sum_{i=1}^{n} y_i + p_{20}\sum_{i=1}^{n} {x_i}^2 + p_{11}\sum_{i=1}^{n} x_i y_i + p_{02}\sum_{i=1}^{n} {y_i}^2 \quad (8.5)$$

The partial derivatives of the other five coefficients can be found similarly.

$$\sum_{i=1}^{n} zx_i = p_{00}\sum_{i=1}^{n} x_i + p_{10}\sum_{i=1}^{n} {x_i}^2 + p_{01}\sum_{i=1}^{n} x_i y_i + p_{20}\sum_{i=1}^{n} {x_i}^3 + p_{11}\sum_{i=1}^{n} {x_i}^2 y_i + p_{02}\sum_{i=1}^{n} x_i {y_i}^2 \quad (8.6)$$

$$\sum_{i=1}^{n} z_i y_i = p_{00}\sum_{i=1}^{n} y_i + p_{10}\sum_{i=1}^{n} x_i\, y_i + p_{01}\sum_{i=1}^{n} {y_i}^2 + p_{20}\sum_{i=1}^{n} {x_i}^2 y_i + p_{11}\sum_{i=1}^{n} x_i {y_i}^2 + p_{02}\sum_{i=1}^{n} {y_i}^3 \quad (8.7)$$

$$\sum_{i=1}^{n} z_i {x_i}^2 = p_{00}\sum_{i=1}^{n} {x_i}^2 + p_{10}\sum_{i=1}^{n} {x_i}^3 + p_{01}\sum_{i=1}^{n} y_i {x_i}^2 + p_{20}\sum_{i=1}^{n} {x_i}^4 + p_{11}\sum_{i=1}^{n} {x_i}^3 y_i + p_{02}\sum_{i=1}^{n} {y_i}^2 {x_i}^2 \quad (8.8)$$

$$\sum_{i=1}^{n} z_i x_i y_i = p_{00}\sum_{i=1}^{n} x_i y_i + p_{10}\sum_{i=1}^{n} {x_i}^2 y_i + p_{01}\sum_{i=1}^{n} x_i {y_i}^2 + p_{20}\sum_{i=1}^{n} {x_i}^3\, y_i + p_{11}\sum_{i=1}^{n} {x_i}^2 {y_i}^2 + p_{02}\sum_{i=1}^{n} x_i {y_i}^3 \quad (8.9)$$

$$\sum_{i=1}^{n} z_i {y_i}^2 = p_{00}\sum_{i=1}^{n} {y_i}^2 + p_{10}\sum_{i=1}^{n} x_i {y_i}^2 + p_{01}\sum_{i=1}^{n} {y_i}^3 + p_{20}\sum_{i=1}^{n} {x_i}^2 {y_i}^2 + p_{11}\sum_{i=1}^{n} x_i {y_i}^3 + p_{02}\sum_{i=1}^{n} {y_i}^4 \quad (8.10)$$

The six coefficients can be found by solving these six equations. Table 8.2 shows the six coefficients obtained by solving Equations 8.5 to 8.10 in MATLAB.

Table 8.2: Coefficients of the polynomial of Equation 8.1, found by minimizing the sum of squared errors.

p_{00}	p_{10}	p_{01}	p_{20}	p_{11}	p_{02}
4.697	-0.2	-0.4	0.007	0.005	0.013

The final fitness function of Equation 8.11 was found by substituting the coefficients of Table 8.2 into 8.1. Equation 8.11 is plotted in Fig. 8.3.

$$\hat{z} = 4.697 - 0.2 * x - 0.4 * y + 0.007 * x^2 + 0.005 * xy + 0.013 * y^2 \quad (8.11)$$

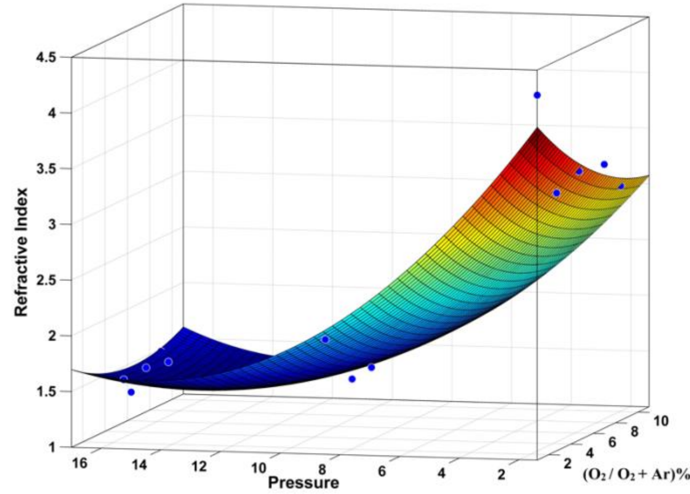

Fig. 8.3: Plotted fitness function of Equation 8.11. Blue dots show the experimental data points of Table 8.1.

At this step, the assumption that a polynomial of degree 2 fits the data, needs to be validated. In order to verify this assumption, the coefficient of determination R^2 of Equation 8.12 was calculated between the SSE for each refractive index data point on Table 8.1, and the total sum of the squared differences of each data point (in Table 8.1) compared to the mean of the data (TSS) (8.13 and 8.14).

$$R^2 = 1 - \frac{SSE}{TSS} \tag{8.12}$$

$$TSS = \sum_{i=1}^{n}(z_i - \bar{z})^2 \tag{8.13}$$

$$\bar{z} = \frac{1}{n}\sum_{i=1}^{n} z_i \tag{8.14}$$

where $\bar{z}$ is the mean of all observed data and z_i is each observed value from Table 8.1. The coefficient of determination (R^2) provides a measure of how much the found fitness function is close to the experimental data points. A higher R^2 means that the fitted surface is closer to the observed data.

Polynomials with different degrees (1 or 2) for *x* and *y* can also be explored by setting these respective coefficients to zero and resolving the fitness function polynomial. The calculated R^2 and SSE for the fitness function for the cases of polynomials with degrees of 1 and 2 considered for variables *x* (oxygen partial flow) and *y* (pressure) are shown in Table 8.3. From Table 8.3, it can be seen that the fitness function of order 2 for *x* and *y* provides the best fitness function with a high R^2 and low SSE, compared to lower order

polynomials. It should be mentioned, that higher order polynomials of degree 3 and 4 were also explored, however, it was found that the R^2 did not significantly change.

Table 8.3: The fitted models using polynomials of various degrees for oxygen partial flow (x) and pressure (y), showing the SSE and R^2.

x degree	*y* degree	SSE	R^2	Model
1	1	3.12	0.74	$z = p_{00} + p_{10}*x + p_{01}*y$
2	1	2.41	0.77	$z = p_{00} + p_{10}*x + p_{01}*y + p_{11}*x*y + p_{20}*x^2$
1	2	0.41	0.96	$z = p_{00} + p_{10}*x + p_{01}*y + p_{11}*x*y + p_{02}*y^2$
2	2	0.34	0.96	$z = p_{00} + p_{10}*x + p_{01}*y + p_{11}*x*y + p_{20}*x^2 + p_{02}*y^2$

In addition to polynomial regression, two other fitting methods including LOWESS and Interpolation were also considered. However, these methods were rejected for the following reasons. LOWESS (Locally Weighted Scatter Smooth), would result in a well-fitted curve, however, a single equation function (which would serve as a fitness function) cannot be obtained. This would make the implementation of the subsequent GA not straightforward. In case of interpolation, since the data has scattered (or non-predictable) error, this method was determined to be not appropriate for predicting the response of a new set of variables.

8.4.2 Implementing the GA

Equation 8.11 was used as the fitness function for implementing Genetic algorithm optimization. A desired refractive index is set to be our objective value ($n_{objective}$) and the GA works to find the local minimum of the fitness function $\hat{z}$ [87, 88]. The goal is to find the needed deposition parameters where 8.15 is met.

$$\hat{z} = n_{\text{objective}} \tag{8.15}$$

Equation 8.15 is re-written in the form of 8.16, and the GA works to evolve toward the solutions where $S = 0$.

$$S = \hat{z} - n_{objective} \tag{8.16}$$

First, a population (P) of members of size m is generated. Then, genes for pressure (y_i) and oxygen partial flow (x_i) are randomly selected from between the lower and upper bounds of the pressure (1 - 20 mTorr) and oxygen partial flow (1 - 11%) for each population member (P_i). This population group is the 0th generation. For all population members, the predicted refractive index $\hat{z}_i$ (fitness value) is calculated using Equation 8.11. Equation 8.16 is then calculated to find S for each population member to check how far the fitness value is from the objective value ($n_{objective}$). The value of S is the base of the ranking (scoring) system between population members. Next, the two highest ranking population members to the objective value (those with the smallest score or $|S|$) directly move to the next generation. These members were called elite members. The remaining members of the evolution population (p) which now has size $m-2$, are selected as parents for making children of the next generation by mutation or crossover methods. The mutation and crossover methods are performed to make children equal in number to 20% and 80% of the evolutionary sub-population, respectively. The selection of 20% and 80% is a common implementation ratio [89, 90].

8.4.2.1 Crossover method and selection for the next generation

In the crossover method, a pair of parents are used to generate children for the subsequent generations. The genes of parents are combined to effectively evolve genes toward superior children. Stochastic Universal Sampling (SUS) technique [88] was used for selection of members for crossover. SUS tends to favor selection of unique individuals. First, all the evolution population members (which number p_{m-2}) are placed along a line (see Fig. 8.4) based on their absolute value deviation ($|S_i|$) from the desired fitness value ($n_{objective}$). The first population member of this group (p_1) is spaced a distance $|S_1|$ from 0. The second evolutionary population member (p_2) is spaced a distance $|S_2|$ from member p_1, thus a total distance $|S_1| + |S_2|$ from 0, and so on, for all evolutionary population members. Along this line, each evolutionary

population member is given ownership to the line segment to its left. Next, a random position along the line of Fig. 8.4 is selected, and the member who owns the line segment of this position is designated as crossover parent A. The second parent is determined as follows. First, a random step size is selected and this is added to the position location of the first parent. The second parent is then found at this new location. If this location is beyond the position of the last evolutionary population member (p_{m-2}), the distance continues to be measured from 0. In essence, the line is a circle which wraps back upon itself. The crossover process continues until the number of parent pairs equals 80% of the evolutionary population size, or in other words, 0.8 * (*m*-*2*) times.

Fig. 8.4: The Stochastic Universal Sampling technique, for selecting the population members as crossover parents for the next generation.

Once the parent pairs are selected a child for the next generation is formed by mixing the parents genes. To generate a child, a weighted average of each gene (*x* and *y*) is calculated. The weighting is a randomly assigned value *W* from 0 to 1. Equations 8.17a and 8.17b show the relationship between the parents and the generated gene in the employed crossover method.

$$x_{new} = (1-W) * x_{parent\ 1} + W * x_{parent\ 2} \tag{8.17a}$$

$$y_{new} = (1-W) * y_{parent\ 1} + W * y_{parent\ 2} \tag{8.17 b}$$

8.4.2.2 Mutation method

In the mutation method, a single parent is mutated to create a new child. This is done by making a random change to both the genes *x* and *y* in a single parent. The random change is done by adding a random vector (*V*) from a Gaussian distribution within the boundaries of each variable *x* and *y*. The new genes are generated using 8.18a and 8.18b.

$$x_{new} = V + x_{parent\ 1} \tag{8.18a}$$

$$y_{new} = V + y_{parent\ 1} \quad (8.18b)$$

By doing so, this method seeks to randomly create new population members that might potentially have fitness values closer to the objective value. Then augments the crossover method by introducing new genes into the population.

8.4.2.3 GA convergence criteria

When the average deviations of fitness values between all members of the population from the objective value ($|S_i|$) is less than the tolerance, which was set to 10^{-4}, the GA evolutionary process terminates.

8.4.2.4 GA prediction results

An objective refractive index of $n_{objective}$ = 1.45 was set and the GA was run to determine the optimal deposition parameters. Table 8.4 shows the results for three population sizes of m = 10, 15 and 20, which were found to evolve to convergence in 7, 9 and 10 generations respectively. In Fig. 8.5a and Fig. 8.5b, the evolution trend of case 3 of Table 8.4 is illustrated as an example. Fig. 5 (a) shows the genes (x and y) of all population members in each generation. Fig. 8.5b shows the values of the fitness function for all population members, for each generation.

Table 8.4: GA parameters for three population size of 10, 15 and 20, with the objective being an SiO_x film with n = 1.45.

Case No.	Population size	Evolved generations	Predicted refractive index by GA	x (oxygen partial flow)	y (pressure)
1	10	7	1.45	8.52	15
2	15	9	1.45	8.55	17.36
3	20	10	1.45	8.53	15.08

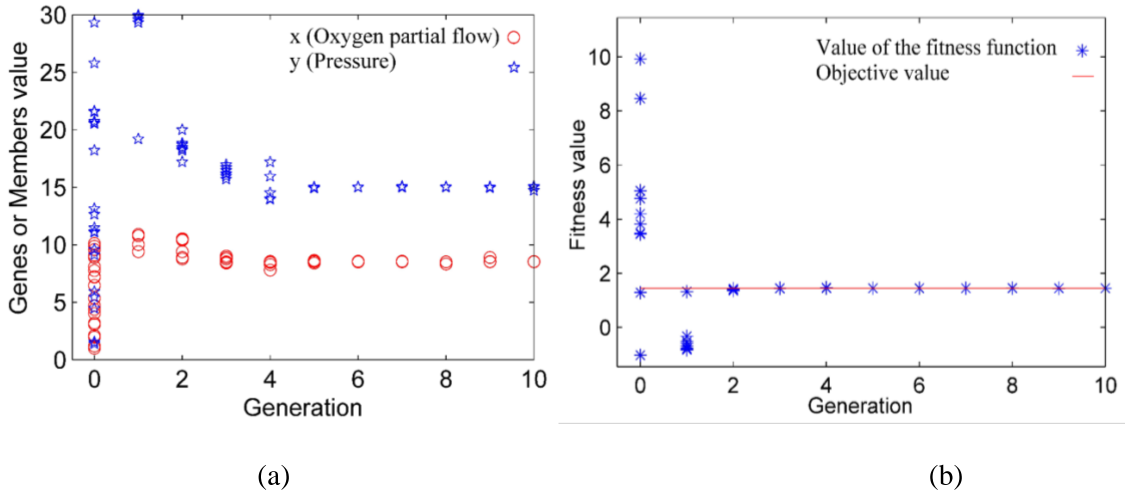

(a) (b)

Fig. 8.5:a) Genes of all population members at each generation. b) Evolution of the fitness value of population members through the generations for the population size of 20. Blue stars show the value of the fitness function of each member, converging to the objective value (red line).

8.4.3 Experimental verification of the GA results

New SiO_x thin film samples were reactively sputtered using the optimum values for *x* and *y,* of cases 1 and 2 of Table 8.4. Table 8.5 summarizes the deposition conditions as well as measured refractive index of the new samples. We can see that the measured refractive indices for the deposited films using the deposition conditions found by GA, of cases 1 and 2, show high correlation with the refractive index value of 1.45, used as the GA's objective value.

In the initial experiments reported in Table 8.1, no thin film was experimentally deposited with a refractive index below 1.48. Therefore, the results of Table 8.5 clearly show the potential of the GA to predict the needed deposition parameters to deposit a thin film with an objective refractive index outside of the initial data set of Table 8.1.

The GA's process prediction ability was further explored by running the algorithm to find the deposition parameters required to deposit a refractive index that was not experimentally found before. The objective refractive index of n = 2.5 was selected since it has not been previously deposited in Table 8.1 and since there are no nearby experimentally found refractive indices. A value of 10.2% for oxygen partial

flow and 1.7 mTorr pressure were predicted by the GA. Subsequently, the refractive index of the experimentally deposited film was measured 2.513 (see Table 8.5), which closely agrees with the objective value.

Table 8.5: Sputtering parameters and measured refractive index of deposited samples with GA predicted oxygen partial flow and pressure.

	$O_2/(O_2+Ar)$ %	Pressure (mTorr)	Predicted refractive index	Measured refractive index
Table 4 case 1	8.5	15	1.45	1.455
Table 4 case 2	8.5	17.3	1.45	1.44
n = 2.5 case	10.2	1.7	2.5	2.513

8.5 Distributed Bragg Reflector

In this section, the above method was used to fabricate a Distributed Bragg Reflector (DBR). The optical characteristics of a DBR were employed in this study to validate the ability of the reactive sputtering process to form reliable multi-layers of high and low SiO_x refractive index. Another reason for fabricating a DBR was that it can be used to replace the aluminum mirror fabricated on top of the micro-mirror which was described in the previous chapters. Compare to an aluminum mirror which is reflective in optical wavelengths, a DBR can be designed in the way to have a high reflectivity on a wider range of wavelengths.

8.5.1 DBR background and design

DBRs are highly reflective mirrors which usually reflect the light in a wide range of wavelengths. They are also known as one-dimensional photonic crystals. A DBR is composed of multi-layers of high and low refractive index (n) materials, where the optical thickness ($n \times thickness$) of each layer is a quarter of reflected wavelength λ_0 (Fig. 8.6). Several pairs of materials have been used for fabricating DBRs like TiO_2/SiO_2 [91, 92], Ta_2O_5/SiO_2 [93, 94], Si_3N_4/SiO_2 [96], AlN/GaN [93, 96], ZnS/CaF_2 [98]. The constituent material is usually determined by the application. The evaluation DBR of this work was

fabricated by alternately depositing layers of SiO_x with low and high refractive indices. The DBR consists of an odd number of layers (9 layers or 4.5 pairs) with the high refractive index layer as the top and bottom layers. This structure was designed based on the standard arrangement of reference [28].

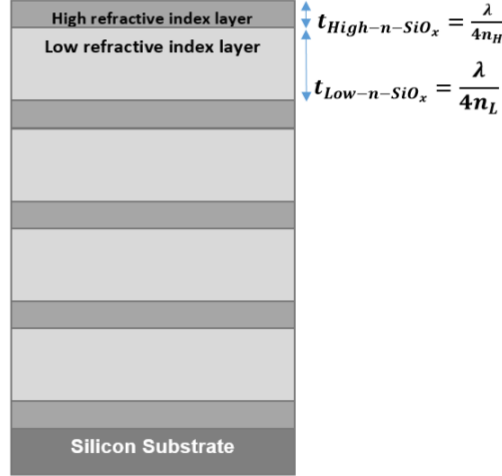

Fig. 8.6: Schematic of a distributed Bragg reflector consisting of a quarter-wavelength-thick of high and low refractive index SiO_x layers, λ is the central reflected wavelength.

The effect of the refractive index of each layer on the reflectivity and bandwidth of a DBR is explained in this section. Fresnel law of reflection describes the behaviour of light when it is incident on the boundary at which the refractive index changes. However, when a monochromatic plane wave is incident on a periodic media like DBR, according to Bloch's theorem, a Bloch wave is generated. The generated Bloch wave takes the periodicity form of the one-dimensional lattice. If the Bloch waves inside the photonic band structure of the periodic media are not placed in the bandgap of the lattice, they can pass through it. If the electromagnetic waves are placed in the bandgap, the field energy reflects back. Reflecting back of the field energy forms the high reflectivity band of a DBR [99]. Some applications of DBRs are to selectively reflect light in surface emitting lasers [94], and LEDs [100], or selecting a special wavelength in photodiodes [101]. The reflection response of a DBR is calculated by Equation 8.19 [28, 98].

$$\Gamma_1 = \frac{1-\left(\frac{n_H}{n_L}\right)^{2N} \frac{n_H^2}{n_a n_b}}{1+\left(\frac{n_H}{n_L}\right)^{2N} \frac{n_H^2}{n_a n_b}} \tag{8.19}$$

where Γ_1 is the reflectivity, N is the number of layers, n_H and n_L are the high and low refractive indices of the materials, and n_a and n_b are the refractive indices of incident medium and substrate respectively. The reflected bandwidth is calculated by Equation 8.20,

$$\frac{\Delta\lambda}{\lambda_0} = \frac{\pi}{2}\left[\frac{1}{cos^{-1}(\rho)} - \frac{1}{cos^{-1}(-\rho)}\right] \tag{8.20}$$

where $\rho = \cos(\frac{\delta_H+\delta_L}{2})$, $\delta_H = \frac{2\pi}{\lambda}n_H t_H$ and $\delta_L = \frac{2\pi}{\lambda}n_L t_L$ are the phase thicknesses of the high and low refractive index materials.

From Equations 8.19 and 8.20 it can be seen that for a certain number of layers, a high contrast between the low and high refractive index materials, would result in a higher reflection bandwidth as well as higher reflectivity. High reflection bandwidth and high reflectivity are two important characteristics of a DRB. For example, in solar cells it is necessary to tightly trap the incident light [102] therefore, achieving high reflectivity is very important.

8.5.2 DBR fabrication by reactive sputtering of silicon

The deposition conditions for a high refractive index of 2.5 and a low refractive index of 1.45 were determined by the above-described GA process. The GA was run for 100 times and the average value of the resulted data was recorded, in order to ensure that the predicted values of GA are robust for fabricating a DBR. Table 8.6 shows the deposition parameters which were calculated to fabricate layers of SiO_x with a high refractive index of 2.5 and a low refractive index of 1.45. A central reflection wavelength of 900 nm was selected. The thickness of each layer was calculated based on the quarter wavelength requirement for each layer. Using equations shown in Fig. 8.6, the thickness of the layers was calculated to be 155 nm for low refractive index (n = 1.45) SiO_x layer and 90 nm for high refractive index (n = 2.5) layer. The fabrication conditions are summarized in Table 8.6.

Table 8.6: Fabrication conditions of the DBR.

Layer material	Ar flow	O_2 flow	O_2 partial flow	Pressure	Refractive index
High refractive index SiO_x	34 sccm	2 sccm	5.5 %	3.9 mTorr	2.5
Low refractive index SiO_x	56.4 sccm	5.2 sccm	8.4 %	17.5 mTorr	1.455

An ellipsometer (J.A. Woollam model M-2000) operating as a spectrometer was used to measure the reflection profile of the DBR. The measured intensity was normalized by the source light intensity. Fig. 8.7 shows the measured and calculated normalized reflection coefficient of the DBR. The graph shows that the fabricated DBR demonstrates a high reflection of 95%, with the band of high refection wavelengths is extending from 730 - 1000 nm as measured. Theoretically, the high reflection band extends beyond the 1000 nm, however, we could not measure this with our spectrometer due to the wavelength limit of the spectrometer. In the measurement graph of Fig. 8.7 there are some fluctuations within the high reflection band. One reason could be the accuracy of the thickness of the deposited SiO_x layers. If the optical thickness of layers does not exactly match the quarter-wavelength law (Fig. 8.6), a portion of the electromagnetic energy at particular wavelengths will be dissipated.

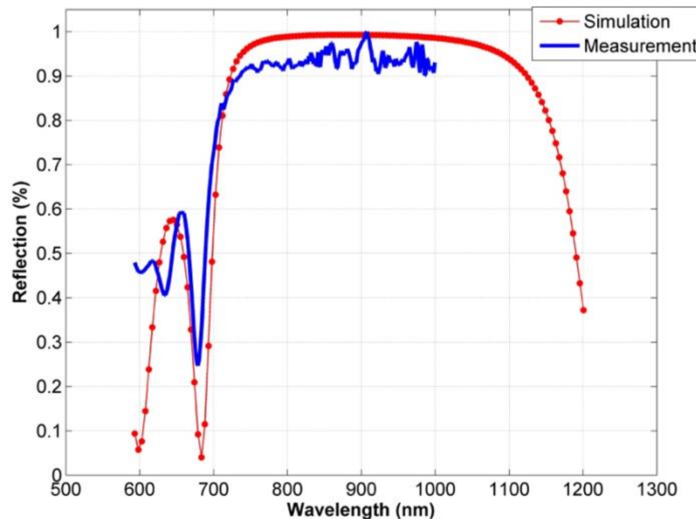

Fig. 8.7: Calculated (dotted) and measured (solid) spectrum of SiO_x DBR. The graph shows a reflectivity of 95 % in reflection-band of more than 270 nm.

Table 8.7 compares the features of the DBR fabricated in this work with other DBRs fabricated by the sputtering technique by other research groups. Comparing to the DBRs fabricated by [70, 91, and 102], no metal sources were used in the fabrication of the DBR of this work. Eliminating metal components is important in terms of reducing the losses due to the extinction coefficient. In the measured range, the extinction coefficient is almost zero [104] because the refractive index of SiO_x is a real number, and so the losses are negligible [28]. Another advantage of this method is that the reactive sputtering of silicon using oxygen is a continuous procedure. Therefore, the DBRs can be fabricated using a single material source by simply controlling the sputtering parameters to produce either silicon or SiO_x. A relatively similar DBR was reported by reference [105] which is made by reactively sputtering SiN_x layers from silicon target in the presence of nitrogen gas.

Table 8.7: Summary of DBR's characteristics fabricated by the sputtering method.

Publication	Materials	Fabrication Method	Refractive indices	Reflectivity	Reflection-Band
This work	SiO_x/SiO_x (4.5 pairs)	Reactive RF sputtering	2.5/1.455	> 95%	> 270nm
F. X. Kärtner, et al. [92]	TiO_2/SiO_2 (20 pairs)	Ion beam sputtering	2.5/1.5	> 95%	240 nm
S. Chichibu, et al. [71]	ZrO_2/SiO_2 (8 pairs)	Reactive RF sputtering	2.1/1.46	> 95%	82 nm
M. K. Anuar, et al. [103]	SiC/MgO (7 pairs)	RF sputtering	3.17/2.19	> 95%	180nm
C. Levallois, et al. [105]	a-Si/a-SiN_x (4.5 pairs)	Reactive RF sputtering	3.74/1.84	> 95%	800nm

8.6 Summary and conclusions

In this chapter, first, a process was developed in which a thin film with a specific refractive index can be deposited. This process included investigating the effect of depositing pressure and oxygen partial flow on the refractive index of SiO_x thin films deposited by RF reactive magnetron sputtering. Depositing thin films of SiO_x with a wide range of refractive indices from 1.48 to 4.28 was shown possible by varying pressure from 1.4 mTorr to 17 mTorr and oxygen partial flow from 1 to 11%. It was found that, for a given pressure, increasing the oxygen partial flow, reduced the refractive index of the deposited film. On the other hand, for a constant amount of oxygen partial flow, a lower refractive index was observed at the films deposited at the higher-pressure range. At lower pressures, this reduction was more significant. Experimental data showed that by only considering the pressure and oxygen partial flow the refractive index of the reactively sputtered SiO_x films could be modeled. Using experimental data a statistical model was developed to define a relationship, which was used as the fitness function of the genetic algorithm. The required deposition conditions needed to obtain arbitrary refractive indices that are different from the initial data set were determined by employing the genetic algorithm. The needed oxygen partial flow and process pressure to deposit SiO_x films with a high refractive index of 2.5 and lower index of 1.455 were correctly determined by GA. Then, a DBR was fabricated that contained 4.5 pairs of SiO_x layers with low and high refractive indices equal to n = 1.455 and n = 2.5 SiO_x processes. A high reflection of 95% over a large bandwidth of more than 270 nm was demonstrated by the fabricated DBR.

9

Conclusions & Future Work

Contents

9.1 Summary 118
9.2 Concluding Remarks 120
9.3 Future Works 121

9.1 Summary

In this thesis, the development of a 3 degree of freedom micro-mirror and a method for fabricating reactively sputtered thin films with specified refractive indices were presented.

3 DOF Micro-mirror:

The development steps of the micro-mirror including design, modeling, simulation, fabrication, and testing of the device were discussed in Chapters 2 to 7. In Chapter 2, various types of actuation forces and structures used for building micro-mirrors were discussed. It was concluded that a Lorentz force actuation with a gimbal-less structure is an appropriate choice for making a 3-dimensional, large-tilt-angle micro-mirror. The operating mechanism and enabling of each motion were explained in Chapter 3. The operation of the micro-mirror was simulated in Chapter 4 to calculate its displacement, frequency response, and

thermal properties. The bending and torsional spring constants of the serpentine springs were also explored. These values were later used in Chapter 5, where an analytical model of the micro-mirror was presented. This analytical model included a mass-spring model which was used to calculate the transfer function of the system. Lagrange's equations were also solved for the micro-mirror system to understand its dynamic response. The analytical models of Chapter 5 were developed to explain the experimental results which were later explored in Chapter 7. The fabrication details of the micro-mirror were explained in Chapter 6. In Chapter 7 the experiments which were done to test the performance of the micro-mirror and its results were described. The micro-mirror was tested in both static mode (by applying a dc current) and dynamic mode (by applying an ac current). The measured step response of the micro-mirror system showed a fair correlation with the values calculated in Chapter 5 using the mass-spring model. The mode coupling effect which happened by applying different frequencies to the system was also explained using Lagrange's equations. By actuating the horizontal motion at a fast frequency (292 Hz) and the vertical motion at a slow (40 Hz) frequency, a raster scan was made.

Reactively sputtered thin films with specified refractive index:

In Chapter 8 of the thesis, a method for fabricating materials with a specific refractive index was presented. This method employs reactive sputtering of SiO_x layers by varying oxygen partial flow and deposition pressure. First, several experiments were run to make a variety of oxygen partial flow and pressure data points. Then, some statistical studies were done to relate the refractive index of the deposited layer with the oxygen partial flow and deposition pressure of the system. Using that relationship, the deposition parameters for depositing a layer with a desired refractive index was calculated. The method was practically proved for several refractive indices. A DBR was fabricated whose refractive index of the constituent layers was determined by the presented method.

9.2 Concluding remarks

The developed micro-mirror demonstrated the following features:

- 3 degrees of freedom in motion

  Tilting about *x-axis* and *y-axis* and translational motion along *z-axis*.

- Large tilt angle and translational displacement

  With a magnetic field of 0.1 T, the MEMS mirror showed a *y-axis* tilt angle of 22.8º at 247.5 Hz, *x-axis* tilt of 13.3º at 292.7 Hz, and linear displacement of 232 μm.

- Low temperature rise

  The amount of temperature rise was simulated to be 7.7°C for 20 mA input current.

- Low input voltage

  The micro-mirror was actuated with an input voltage of 0.1 V.

- Low power consumption

  The consumed power for the above tilt motions was 2.6 mW at resonance.

- (Relatively) Simple micromachining process and material

  The micro-mirror was fabricated from a single crystal silicon wafer using common methods.

- Static and dynamic motions

  Both static (dc actuation) and dynamic (ac actuation) motions were shown to be possible.

The method developed for depositing films with a specified refractive index, features:

- One source of target material.
- Low-temperature deposition of material that can result in a film with lower thermal stress.
- A wide range of refractive indices were shown to be possible.
- The fabricated DBR showed a high reflection of 95% with 270 nm bandwidth.

9.3 Future work

The MEMS actuator presented in this work can be a platform for tunable optical components. For example, in this research a MEMS mirror and a DBR were fabricated separately. One improvement to this work can be combining these two components. By fabricating a DBR on top of the MEMS actuator presented in this work, a movable Bragg mirror can be produced. Employing a movable Bragg mirror can help simplify the alignment of the Bragg mirror inside a laser cavity. Using the algorithm presented in Chapter 8, DBRs with different ranges of reflection wavelengths can be fabricated.

Another optical component that can be implemented using this actuator, is a tunable Fresnel lens. The design and modeling of a MEMS-controllable linear motion Fresnel Zone Plate (FZP) has been reported by our group in reference [106]. In an FZP, the focal length is a function of incident wavelength. Using this principle for separating wavelengths, enables a spectrometer application. In reference [106] an FZP was designed on top of the MEMS actuator. Therefore, by linearly moving the actuator along the *z-axis*, the focal length of different wavelengths can be selected. The FZP of [106] was designed with 400 zones, which can focus UV wavelengths from 150 nm to 410 nm by moving a distance of 1 mm.

One potential improvement that could be made to this micro-mirror system for optical applications, is to add a position feedback mechanism. Adding a position feedback would require depositing and patterning a position sensor (such as a PZT material) on the mirror and the flexures. The displacement or the mechanical stress on the structure would be transduced to signal which could be used to determine the position of each flexure. Using this data a controller system can be designed to reduce the error of the displacement that helps focusing the laser spot on a specific point.

Depending on the application, the mechanical structure of the MEMS actuator can also be modified. For example, using an electromagnet instead of the permanent magnet can reduce the thickness of the final device and decrease magnetic interference. An array of micro-mirrors can also be fabricated and used to direct the light beam in a volume of space.

Another mechanical enhancement of the structure would be using a rib structure on the backside of the mirror plate. By using the ribbed structure to maintain stiffness while reducing overall mirror average thickness, the mass of the mirror will be reduced which would result in a higher resonance frequency. In addition, the ribs could make the mirror stiffer by resisting against the motion in specific directions. This fact could also improve the flatness of the mirror, since a stiffer mirror would deflect less under load (such as thermal expansion). Optimization of a ribbed structure to maximize stiffness while minimizing mass can be found by exploring the number of ribs, their height, and other parameters, and studying the effect on the resonance frequency and the flatness of the mirror.

Appendices

Appendix 1 - Calculation of the spring constants

When the micro-mirror is tilting about the *x*- or *y-axis*, the springs have two types of motion; bending and torsional motion. Therefore, two different spring constants including bending spring constant and torsional spring constant should be considered. In Chapter 4, these spring constants were calculated using an FEM simulation. In the following sections, the analytical methods which are used for calculating these values are described.

A.1.1 Calculation of the bending spring constant (k_s and k_m)

Spring constant of the flexure can be calculated using energy method [107]**.** First, the free-body-diagram of a flexure was drawn and the moments of bending, torsions and forces on the head and end of each beam were written.

$$M_i^C = M_0 - f_z(\xi + (i-1)l_C)\,, i = 1 \; to \; 11 \tag{A.1}$$

$$T_i^C = T_0 + (-1)^{i-1} f_z\left(\frac{l_S}{2} + \frac{(1-(-1)^i}{2} l_S\right), i = 2 \; to \; 10 \tag{A.2}$$

$$T_1^C = T_{11}^C = T_0$$

$$M_j^S = T_0 - f_z(\xi + \frac{l_S}{2} + \frac{(1-(-1)^j}{2} l_S)\,, j = 2 \; to \; 9 \tag{A.3}$$

$$M_0^S = M_{10}^S = T_0 - f_z\xi$$

$$T_j^S = M_0 - jf_z a \tag{A.4}$$

where M_0 and T_0 are the external moment of bending and torsion applied to guided-end of the first connector. M_i^C, and M_i^S are the moments of bending applied on each connector and span respectively; T_i^C, and T_i^S are the torsions applied on each connector and span respectively.

Then, the stored strain energy in each beam is calculated as follow:

$$U_i^C = \frac{{M_i^C}^2}{2E_{eq}I_{y,a}} + \frac{{T_i^C}^2}{2G_{eq}J}\,, i = 1 \; to \; 11 \tag{A.5}$$

$$U_i^S = \frac{M_j^{S^2}}{2E_{eq}I_{x,b}} + \frac{T_j^{S^2}}{2G_{eq}J} \ , j = 1 \ to \ 10 \tag{A.6}$$

where U_i^C and U_i^S are the strain energy in each connector and span respectively. $I_{y,a}$ is the moment of inertia of one connector bending about *y-axis* and $I_{x,b}$ is the moment of inertia for one span bending about *x-axis*.

$$I_{y,a} = \int_0^a \int_{-t/2}^{t/2} z^2 \, dx \, dz = \frac{at^3}{12} \tag{A.7}$$

$$I_{x,b} = \int_0^w \int_{-t/2}^{t/2} z^2 \, dx \, dz = \frac{wt^3}{12} \tag{A.8}$$

In Equations A.5 and A.6, E_{eq} represents the equivalent Young's modulus of the multilayer structure, G_{eq} represents the equivalent shear modulus of the multilayer structure and *J* represents torsion constant of the beams. G_{eq} was found to be 29.36 GPa using an FEM simulation in COMSOL. The calculation of equivalent Young's modulus and *J* are described in the following sections.

A.1.2 Calculating Equivalent Young's modulus

E_{eq} is the equal Young's modulus of the structure, which was calculated for a multilayer structure as below:

$$E = \frac{stress}{strain} = \frac{\sigma}{\varepsilon} = \frac{F/A}{\Delta L/L_0} = \frac{F \, L_0}{A \, \Delta L} \tag{A.9}$$

where *F* is the force applied to a beam of initial length *L* and area *A*. ΔL is the change in length caused by force *F*.

$$F = \frac{E \, A}{L_0} \Delta L \rightarrow F = K \, \Delta L \tag{A.10}$$

Comparing to Hooke's law:

$$K = \frac{E \, A}{L_0} \tag{A.11}$$

Using the laws of parallel springs and replacing the area with the product of width and thickness:

$$K_{eq} = K_1 + K_2 + K_3$$

$$K_{eq} = \frac{E_1 \, A_1}{L_{0,1}} + \frac{E_2 \, A_2}{L_{0,2}} + \frac{E_3 \, A_3}{L_{0,3}} = \frac{E_1 \, t_1 w_1}{L_{0,1}} + \frac{E_2 \, t_2 w_2}{L_{0,2}} + \frac{E_3 \, t_3 w_3}{L_{0,3}} \tag{A.12}$$

Assuming all the layers are of the equal width and length:

$$K_{eq} = \frac{E_1 t_1 w}{L_0} + \frac{E_2 t_2 w}{L_0} + \frac{E_3 t_3 w}{L_0} \tag{A.13}$$

$$\frac{K_{eq} L_0}{w} = E_1 t_1 + E_2 t_2 + E_3 t_3 \tag{A.14}$$

$$t_t = t_1 + t_2 + t_3$$

Dividing both sides of the equation to t_t:

$$\frac{K_{eq} L_0}{w t_t} = \frac{E_1 t_1}{t_t} + \frac{E_2 t_2}{t_t} + \frac{E_3 t_3}{t_t} \tag{A.15}$$

$$E_{eq} = \frac{E_1 t_1}{t_t} + \frac{E_2 t_2}{t_t} + \frac{E_3 t_3}{t_t} \tag{A.16}$$

After finding the E_{eq}, G_{eq}, J and $I_{x,b}$, the values were substituted in Equations A.5 and A.6. Next step is finding T_0 and M_0. According to Castigliano's theorem, the first partial derivation of strain energy with respect to the applied load is equal to the displacement at the point where the load is applied. In this serpentine spring, the angular displacements corresponding to the external bending moment and torsion are constrained to be zero by the guided-end and symmetry of the flexure:

$$\psi_0 = \frac{\partial U}{\partial M_0} = \sum_{i=1}^{11} \int_0^a \frac{\partial U_i^C}{\partial M_0}\, d\xi + \sum_{j=0}^{10} \int_0^b \frac{\partial U_j^S}{\partial M_0}\, d\xi = 0 \tag{A.17}$$

$$\phi_0 = \frac{\partial U}{\partial T_0} = \sum_{i=1}^{11} \int_0^a \frac{\partial U_i^C}{\partial T_0}\, d\xi + \sum_{j=1}^{10} \int_0^b \frac{\partial U_j^S}{\partial T_0}\, d\xi = 0 \tag{A.18}$$

We assumed that there is no bending and torsion at the guided-end on the beams. By solving $\psi_0 = 0$, M_0 is calculated as a function of f_z. In the same way, by solving $\phi_0 = 0$, T_0 is calculated as a function of f_z. After determining T_0 and M_0, they are substituted in the strain energy of A.5 and A.6. At this step, the only unknown parameter in the equations is f_z. Displacement in the z direction can be found by taking derivation of strain energy with respect to the force f_z.

$$\Delta x = \frac{\partial U}{\partial f_z} = \sum_{i=1}^{11} \int_0^a \frac{\partial U_i^C}{\partial f_z}\, d\xi + \sum_{j=0}^{10} \int_0^b \frac{\partial U_j^S}{\partial f_z}\, d\xi \tag{A.19}$$

Finally, the spring constant was calculated by dividing displacement to the force:

$$K_s = \frac{f_z}{\Delta x} \tag{A.20}$$

Appendix 2 - Calculation of moment of inertia (J_s and J_m)

Mass moment of inertia, is the equivalent of mass, in rotational motions. In the mass-spring model presented in Chapter 5, J_s and J_m represent the mass moment of inertia of the spring and mirror. The mass moments of inertia of the various elements are calculated below.

A.2.1 Mass moment of inertia of one flexure (J_s)

Equation A.21 calculates the mass moment of inertia for one flexure when rotating about the *y-axis*:

$$J_s = \rho \times \sum_1^n \int_0^w \int_0^l \int_0^t (x^2 + z^2)\, dx\, dy\, dz \tag{A.21}$$

where $n = 21$ is the number of beams in one flexure; w, l and t are the width, length and thickness of each beam, respectively; and ρ is the equivalent density of the material. By substituting $w = 110$ µm, $l_{span} = 2000$ µm, $l_{connector} = 200$ µm, $t = 6.7$ µm, and $\rho = 2403.6$ kg/m^3, J_s can be calculated.

A.2.2 Mass moment of inertia of half-mirror (J_m)

The mass moment of inertia of the half-mirror J_m was calculated as below:

$$J_m = \rho \left(\int_0^a \int_0^{b\left(-\frac{y}{a}+1\right)} \int_0^{t_t} (x^2 + z^2)\, dx\, dy\, dz + \int_{-a}^0 \int_0^{b\left(\frac{y}{a}+1\right)} \int_0^{t_t} (x^2 + z^2)\, dx\, dy\, dz\right) \tag{A.22}$$

By substituting a = b = 1414.21 µm and ρ = 2403.6 kg/m3, J_m can be calculated.

The total mass moment of inertia of the mirror-spring system was calculated to be 1.4×10^{-10} kg/m^2.

Appendix 3 - Calculation of damping coefficient (*B*)

The damping coefficient (*B*) was found using FEM simulation. A load force equal to the amount of Lorentz force was applied on flexures and mirror sides. The angular velocity at one corner of the mirror was measured. The damping coefficient was calculated by dividing the torque generated by the Lorentz force to the angular velocity:

$$B = \frac{\tau_a}{\omega} = \frac{f_a \times r}{\omega} \tag{A.23}$$

where τ_a is the torque caused by the Lorentz force, r is the distance from the corner of the mirror to its center which is the rotation axis, and ω is the angular speed of the tilting mirror. B was obtained to equal 8.42×10^{-11} N·m·s/rad.

Bibliography

[1] Y. Kamada *et al.*, "A low-cost, 30 NG/VHZ noise floor MEMS accelerometers for large sensor network," in *2018 IEEE Micro Electro Mechanical Systems (MEMS)*, 2018, pp. 936–939.

[2] P. Minotti *et al.*, "High Scale-Factor Stability Frequency-Modulated MEMS Gyroscope: 3-Axis Sensor and Integrated Electronics Design," *IEEE Trans. Ind. Electron.*, vol. 65, no. 6, pp. 5040–5050, 2018.

[3] Y. Ge, K. Cai, T. Wang, and J. Zhang, "MEMS pressure sensor based on optical Fabry–Perot interference," *Optik (Stuttg).*, vol. 165, pp. 35–40, 2018.

[4] A. H. Zahr *et al.*, "Long-term actuation demonstration of RF-MEMS switches for space applications," in *2018 Symposium on Design, Test, Integration & Packaging of MEMS and MOEMS (DTIP)*, 2018, pp. 1–4.

[5] J. Ma, "Advanced MEMS-based technologies and displays," *Displays*, vol. 37, pp. 2–10, 2015.

[6] Z. Qiu *et al.*, "MEMS based multi-spectral dual-axis confocal microendoscope for clinical applications (Conference Presentation)," 2018, vol. 10545, p. 105450N.

[7] N. Liverman, E. Delly, L. Haugabrook, T. Fregin, and N. C. Moore, "3D micro-mirror lithography for mass production," 2018, vol. 10584, p. 105840X–10584–9.

[8] B. Park, M. Li, S. Liyanage, and C. Shafai, "Lorentz force based resonant MEMS magnetic-field sensor with optical readout," *Sensors Actuators A Phys.*, vol. 241, pp. 12–18, 2016.

[9] C. Pollock, J. Morrison, M. Imboden, T. D. C. Little, and D. J. Bishop, "Beam shaping with tip-tilt varifocal mirror for indoor optical wireless communication," *Opt. Express*, vol. 25, no. 17, pp. 20274–20285, 2017.

[10] D. Dudley, W. M. Duncan, and J. Slaughter, "Emerging digital micromirror device (DMD) applications," 2003, vol. 4985, pp. 4912–4985.

[11] "DLP9000X DLP® 0.90 High Speed WQXGA Type A DMD | TI.com." [Online]. Available: http://www.ti.com/product/dlp9000x. [Accessed: 31-Dec-2018].

[12] S. Luo *et al.*, "Circumferential-scanning endoscopic optical coherence tomography probe based on a circular array of six 2-axis MEMS mirrors," *Biomed. Opt. Express*, vol. 9, no. 5, pp. 2104–2114, 2018.

[13] Y. Xu *et al.*, "MEMS-based non-rotatory circumferential scanning optical probe for endoscopic optical coherence tomography," 2007, vol. 6627, no., pp. 662711–662715.

[14] S. Kim, C. Lee, J. Y. Kim, G. Lim, J. Kim, and C. Kim, "A 2-axis Polydimethylsiloxane (PDMS) based electromagnetic MEMS scanning mirror for optical coherence tomography," 2016, vol. 9698, no., pp. 969812–969816.

[15] M. Strathman, Y. Liu, X. Li, and L. Y. Lin, “Dynamic focus-tracking MEMS scanning micromirror with low actuation voltages for endoscopic imaging,” *Opt. Express*, vol. 21, no. 20, pp. 23934–23941, 2013.

[16] A. Rissanen *et al.*, “MEMS Fabry-Perot Interferometer Based Spectral Sensors for Industrial Applications,” in *Imaging and Applied Optics 2017 (3D, AIO, COSI, IS, MATH, pcAOP)*, 2017, p. ATu1A.1.

[17] B. Saadany, H. Omran, M. Medhat, F. Marty, D. Khalil, and T. Bourouina, “MEMS tunable Michelson interferometer with robust beam splitting architecture,” in *2009 IEEE/LEOS International Conference on Optical MEMS and Nanophotonics*, 2009, pp. 49–50.

[18] K. Yu, D. Lee, U. Krishnamoorthy, N. Park, and O. Solgaard, “Micromachined Fourier transform spectrometer on silicon optical bench platform,” *Sensors Actuators A Phys.*, vol. 130–131, pp. 523–530, 2006.

[19] R. Hokari and K. Hane, “Micro-mirror laser scanner combined with a varifocal mirror,” *Microsyst. Technol.*, vol. 18, no. 4, pp. 475–480, 2012.

[20] L. Persano, A. Camposeo, P. Del Carro, E. Mele, R. Cingolani, and D. Pisignano, “Very high-quality distributed Bragg reflectors for organic lasing applications by reactive electron-beam deposition,” *Opt. Express*, vol. 14, no. 5, pp. 1951–1956, 2006.

[21] A. C.-L. Hung, H. Y.-H. Lai, T.-W. Lin, S.-G. Fu, and M. S.-C. Lu, “An electrostatically driven 2D micro-scanning mirror with capacitive sensing for projection display,” *Sensors Actuators A Phys.*, vol. 222, pp. 122–129, 2015.

[22] T. K. and J. T. and R. Maeda, “Fabrication of Optical Micro Scanner Driven by PZT Actuators,” *Jpn. J. Appl. Phys.*, vol. 44, no. 9S, p. 7078, 2005.

[23] J. Morrison, M. Imboden, T. D. C. Little, and D. J. Bishop, “Electrothermally actuated tip-tilt-piston micromirror with integrated varifocal capability,” *Opt. Express*, vol. 23, no. 7, pp. 9555–9566, 2015.

[24] M. Lara-Castro *et al.*, “Design and Modeling of Polysilicon Electrothermal Actuators for a MEMS Mirror with Low Power Consumption,” *Micromachines* , vol. 8, no. 7. 2017.

[25] A. R. Cho *et al.*, “Electromagnetic biaxial microscanner with mechanical amplification at resonance,” *Opt. Express*, vol. 23, no. 13, pp. 16792–16802, 2015.

[26] I.-J. C. and E. Yoon, “A low-voltage three-axis electromagnetically actuated micromirror for fine alignment among optical devices,” *J. Micromechanics Microengineering*, vol. 19, no. 8, p. 85007, 2009.

[27] J. W. Judy and R. S. Muller, “Magnetically actuated, addressable microstructures,” *J. Microelectromechanical Syst.*, vol. 6, no. 3, pp. 249–256, 1997.

[28] S. J. Orfanidis, “Electromagnetic waves and antennas,” 2002.

[29] M. F. Schubert, F. W. Mont, S. Chhajed, D. J. Poxson, J. K. Kim, and E. F. Schubert, “Design of multilayer antireflection coatings made from co-sputtered and low-refractive-index materials by genetic algorithm,” *Opt. Express*, vol. 16, no. 8, pp. 5290–5298, 2008.

[30] K. Robbie and M. J. Brett, "Sculptured thin films and glancing angle deposition: Growth mechanics and applications," *J. Vac. Sci. Technol. A Vacuum, Surfaces, Film.*, vol. 15, no. 3, pp. 1460–1465, 1997.

[31] K. E. Petersen, "Silicon Torsional Scanning Mirror," *IBM J. Res. Dev.*, vol. 24, no. 5, pp. 631–637, 1980.

[32] Q. Control, S. Measurement, and A. Lighting, "DLP9000 Family of 0 . 9 WQXGA Type A DMDs," 2016.

[33] "DLP2010 DLP® 0.2 WVGA DMD | TI.com." [Online]. Available: http://www.ti.com/product/dlp2010. [Accessed: 31-Dec-2018].

[34] N. Lobontiu and E. Garcia, *Mechanics of microelectromechanical systems*. Springer Science & Business Media, 2004.

[35] Z. Yang, B. Jeong, A. Vakakis, and S. Kim, "A tip-tilt-piston micromirror with an elastomeric universal joint fabricated via micromasonry," *J. Microelectromechanical Syst.*, vol. 24, no. 2, pp. 262–264, 2015.

[36] I. W. Jung, U. Krishnamoorthy, and O. Solgaard, "High fill-factor two-axis gimbaled tip-tilt-piston micromirror array actuated by self-aligned vertical electrostatic combdrives," *J. Microelectromechanical Syst.*, vol. 15, no. 3, pp. 563–571, 2006.

[37] "Advanced Light Control - Overview | DLP Products | TI.com." [Online]. Available: http://www.ti.com/dlp-chip/advanced-light-control/overview.html. [Accessed: 31-Dec-2018].

[38] V. Milanovic, G. A. Matus, and D. T. McCormick, "Gimbal-less monolithic silicon actuators for tip-tilt-piston micromirror applications," *IEEE J. Sel. Top. quantum Electron.*, vol. 10, no. 3, pp. 462–471, 2004.

[39] V. A. Aksyuk *et al.*, "Beam-steering micromirrors for large optical cross-connects," *J. Light. Technol.*, vol. 21, no. 3, pp. 634–642, 2003.

[40] L. Y. Lin, E. L. Goldstein, and R. W. Tkach, "Free-space micromachined optical switches with submillisecond switching time for large-scale optical crossconnects," *IEEE Photonics Technol. Lett.*, vol. 10, no. 4, pp. 525–527, 1998.

[41] H. Li, X. Duan, G. Li, R. K. Oldham, and D. T. Wang, "An Electrostatic MEMS Translational Scanner with Large Out-of-Plane Stroke for Remote Axial-Scanning in Multi-Photon Microscopy," *Micromachines* , vol. 8, no. 5. 2017.

[42] D. A. Skoog, F. J. Holler, and S. R. Crouch, *Principles of instrumental analysis*. Cengage learning, 2017.

[43] U. Baran *et al.*, "Resonant PZT MEMS scanner for high-resolution displays," *J. microelectromechanical Syst.*, vol. 21, no. 6, pp. 1303–1310, 2012.

[44] S. Gu-Stoppel, J. Janes, D. Kaden, H. J. Quenzer, U. Hofmann, and W. Benecke, "Piezoelectric resonant micromirror with high frequency and large deflection applying mechanical leverage amplification," in *Micromachining and Microfabrication Process Technology XVIII*, 2013, vol.

8612, p. 86120I.

[45] D. O. Popa, B. H. Kang, J. T. Wen, H. E. Stephanou, G. Skidmore, and A. Geisberger, “Dynamic modeling and input shaping of thermal bimorph MEMS actuators,” in *Robotics and Automation, 2003. Proceedings. ICRA’03. IEEE International Conference on*, 2003, vol. 1, pp. 1470–1475.

[46] D. Torres, T. Wang, J. Zhang, S. Dooley, X. Tan, and N. Sepúlveda, “Experimental Characterization of the Dynamics of VO2-Based MEMS Mirrors,” no. 50480. p. V001T02A005, 2016.

[47] F. Han, W. Wang, X. Zhang, and H. Xie, “Modeling and control of a large-stroke electrothermal MEMS mirror for Fourier transform microspectrometers,” *J. Microelectromechanical Syst.*, vol. 25, no. 4, pp. 750–760, 2016.

[48] K. Jia, S. R. Samuelson, and H. Xie, “High-fill-factor micromirror array with hidden bimorph actuators and tip–tilt-piston capability,” *J. Microelectromechanical Syst.*, vol. 20, no. 3, pp. 573–582, 2011.

[49] W. Makishi, Y. Kawai, and M. Esashi, “Magnetic torque driving 2D micro scanner with a non-resonant large scan angle,” in *TRANSDUCERS 2009 - 2009 International Solid-State Sensors, Actuators and Microsystems Conference*, 2009, pp. 904–907.

[50] Ç. A. and S. L. and W. N. and N. de Rooij, “A dual-axis pointing mirror with moving-magnet actuation,” *J. Micromechanics Microengineering*, vol. 23, no. 2, p. 25002, 2013.

[51] C. Ji, M. Choi, S. Kim, K. Song, J. Bu, and H. Nam, “Electromagnetic Two-Dimensional Scanner Using Radial Magnetic Field,” *J. Microelectromechanical Syst.*, vol. 16, no. 4, pp. 989–996, 2007.

[52] D. Raboud *et al.*, “MEMS based color-VGA micro-projector system,” *Procedia Eng.*, vol. 5, pp. 260–263, 2010.

[53] A. D. Yalcinkaya, H. Urey, D. Brown, T. Montague, and R. Sprague, “Two-axis electromagnetic microscanner for high resolution displays,” *J. Microelectromechanical Syst.*, vol. 15, no. 4, pp. 786–794, 2006.

[54] H.-M. Jeong *et al.*, “Slow scanning electromagnetic scanner for laser display,” vol. 7, pp. 43003–43013, 2008.

[55] W. Sung *et al.*, “Lorentz force torsional actuator with embedded nickel structures,” in *SENSORS, 2012 IEEE*, 2012, pp. 1–4.

[56] J. N. Reddy, *An introduction to the finite element method*, vol. 2, no. 2.2. McGraw-hill New York, 1993.

[57] J. R. Black, “Electromigration failure modes in aluminum metallization for semiconductor devices,” *Proc. IEEE*, vol. 57, no. 9, pp. 1587–1594, 1969.

[58] E. Afsharipour, R. Soltanzadeh, B. Park, D. Chrusch, and C. Shafai, “Low-power three-degree-of-freedom Lorentz force microelectromechanical system mirror for optical applications,” *J. Micro/Nanolithography, MEMS, MOEMS*, vol. 18, no. 1, pp. 1–11, Jan. 2019.

[59] R. C. Dorf and R. H. Bishop, *Modern control systems*. Pearson, 2011.

[60] N. Lobontiu, *Dynamics of microelectromechanical systems*, vol. 17. Springer Science & Business Media, 2014.

[61] "Calculate magnetic flux density with formula - supermagnete." [Online]. Available: https://www.supermagnete.de/eng/faq/How-do-you-calculate-the-magnetic-flux-density. [Accessed: 31-Dec-2018].

[62] R. A. Conant, J. T. Nee, K. Y. Lau, and R. S. Muller, "Dynamic deformation of scanning mirrors," in *2000 IEEE/LEOS International Conference on Optical MEMS (Cat. No.00EX399)*, 2000, pp. 49–50.

[63] P. J. Brosens, "Dynamic Mirror Distortions in Optical Scanning," *Appl. Opt.*, vol. 11, no. 12, pp. 2987–2989, 1972.

[64] E. Afsharipour, B. Park, and C. Shafai, "Determination of Reactive RF-Sputtering Parameters for Fabrication of SiOx Films With Specified Refractive Index, for Highly Reflective SiOx Distributed Bragg Reflector," *IEEE Photonics J.*, vol. 9, no. 1, pp. 1–16, 2017.

[65] E. A. Pour and C. Shafai, "Tailoring the refractive index of ITO thin films by genetic algorithm optimization of the reactive DC-sputtering parameters," in *Oxide-based Materials and Devices VIII, International Society for Optics and Photonics,* 2017, vol. 10105, p. 101050I–10105–7.

[66] M. F. Schubert, J.-Q. Xi, J. K. Kim, and E. F. Schubert, "Distributed Bragg reflector consisting of high-and low-refractive-index thin film layers made of the same material," *Appl. Phys. Lett.*, vol. 90, no. 14, p. 141115, 2007.

[67] S. Tripathi, S. M. Haque, J. S. Misal, D. D. Shinde, K. D. Rao, and N. K. Sahoo, "Refractive index tailoring of morphology engineered SiO2 thin films by collimated glancing angle RF magnetron sputtering," in *AIP Conference Proceedings*, 2015, vol. 1665, no. 1, p. 80046.

[68] W. H. Southwell, "Coating design using very thin high-and low-index layers," *Appl. Opt.*, vol. 24, no. 4, pp. 457–460, 1985.

[69] E. Hacker, U. Katenkamp, and H. Fischer, "Rf-sputtered SiO2 films for optical applications," *Thin Solid Films*, vol. 97, no. 2, pp. 145–152, 1982.

[70] W.-F. Wu and B.-S. Chiou, "Optical and mechanical properties of reactively sputtered silicon dioxide films," *Semicond. Sci. Technol.*, vol. 11, no. 9, p. 1317, 1996.

[71] S. F. Chichibu, T. Ohmori, N. Shibata, and T. Koyama, "Dielectric Si O 2/Zr O 2 distributed Bragg reflectors for ZnO microcavities prepared by the reactive helicon-wave-excited-plasma sputtering method," *Appl. Phys. Lett.*, vol. 88, no. 16, p. 161914, 2006.

[72] V. Bhatt and S. Chandra, "Silicon dioxide films by RF sputtering for microelectronic and MEMS applications," *J. micromechanics microengineering*, vol. 17, no. 5, p. 1066, 2007.

[73] W. Qiu, Y. M. Kang, and L. L. Goddard, "Quasicontinuous refractive index tailoring of SiN x and SiO x N y for broadband antireflective coatings," *Appl. Phys. Lett.*, vol. 96, no. 14, p. 141116, 2010.

[74] S. A. Khodier and H. M. Sidki, "The effect of the deposition method on the optical properties of SiO 2 thin films," *J. Mater. Sci. Mater. Electron.*, vol. 12, no. 2, pp. 107–109, 2001.

[75] A. Palmero, N. Tomozeiu, A. M. Vredenberg, W. M. Arnoldbik, and F. Habraken, "On the deposition process of silicon suboxides by a RF magnetron reactive sputtering in Ar–O2 mixtures: theoretical and experimental approach," *Surf. Coatings Technol.*, vol. 177, pp. 215–221, 2004.

[76] S. Maniv and W. D. Westwood, "Oxidation of an aluminum magnetron sputtering target in Ar/O2 mixtures," *J. Appl. Phys.*, vol. 51, no. 1, pp. 718–725, 1980.

[77] H. Bartzsch and P. Frach, "Modeling the stability of reactive sputtering processes," *Surf. Coatings Technol.*, vol. 142, pp. 192–200, 2001.

[78] T. Kubart, O. Kappertz, T. Nyberg, and S. Berg, "Dynamic behaviour of the reactive sputtering process," *Thin Solid Films*, vol. 515, no. 2, pp. 421–424, 2006.

[79] O. Auciello and A. R. Krauss, *In situ real-time characterization of thin films*. John Wiley & Sons, 2001.

[80] N. Tomozeiu, J. J. Van Hapert, E. E. Van Faassen, W. Arnoldbik, A. M. Vredenberg, and F. Habraken, "Structural properties of a-SiOx layers deposited by reactive sputtering technique," *J. Optoelectron. Adv. Mater.*, vol. 4, pp. 513–521, 2002.

[81] E. D. Van Hattum, A. Palmero, W. M. Arnoldbik, and F. Habraken, "Experimental characterization of the deposition of silicon suboxide films in a radiofrequency magnetron reactive sputtering system," *Surf. Coatings Technol.*, vol. 188, pp. 399–403, 2004.

[82] L.-N. He and J. Xu, "Properties of amorphous SiO2 films prepared by reactive RF magnetron sputtering method," *Vacuum*, vol. 68, no. 2, pp. 197–202, 2002.

[83] H. Fujiwara, *Spectroscopic ellipsometry: principles and applications*. John Wiley & Sons, 2007.

[84] R. M. Valletta, J. A. Perri, and J. Riseman, "Reactively sputtered silicon dioxide films," *Electrochem Technol*, vol. 4, no. 7, pp. 402–406, 1966.

[85] H.-C. Lin, C.-T. Su, C.-C. Wang, B.-H. Chang, and R.-C. Juang, "Parameter optimization of continuous sputtering process based on Taguchi methods, neural networks, desirability function, and genetic algorithms," *Expert Syst. Appl.*, vol. 39, no. 17, pp. 12918–12925, 2012.

[86] W.-H. Ho, J.-T. Tsai, G.-M. Hsu, and J.-H. Chou, "Process parameters optimization: A design study for TiO $ _ {2} $ thin film of vacuum sputtering process," *IEEE Trans. Autom. Sci. Eng.*, vol. 7, no. 1, pp. 143–146, 2010.

[87] M. Sivapragash, P. Kumaradhas, B. S. J. Retnam, X. F. Joseph, and U. T. S. Pillai, "Taguchi based genetic approach for optimizing the PVD process parameter for coating ZrN on AZ91D magnesium alloy," *Mater. Des.*, vol. 90, pp. 713–722, 2016.

[88] C. R. Houck, J. Joines, and M. G. Kay, "A genetic algorithm for function optimization: a Matlab implementation," *Ncsu-ie tr*, vol. 95, no. 09, pp. 1–10, 1995.

[89] K. Deb, "An efficient constraint handling method for genetic algorithms," *Comput. Methods Appl. Mech. Eng.*, vol. 186, no. 2–4, pp. 311–338, 2000.

[90] J. J. Grefenstette, "Optimization of control parameters for genetic algorithms," *IEEE Trans. Syst.*

Man. Cybern., vol. 16, no. 1, pp. 122–128, 1986.

[91] J. Schaffer, "A study of control parameters affecting online performance of genetic algorithms for function optimization," *San Meteo, Calif.*, 1989.

[92] F. X. Kärtner *et al.*, "Design and fabrication of double-chirped mirrors," *Opt. Lett.*, vol. 22, no. 11, pp. 831–833, 1997.

[93] S. Valligatla *et al.*, "High quality factor 1-D Er 3+-activated dielectric microcavity fabricated by RF-sputtering," *Opt. Express*, vol. 20, no. 19, pp. 21214–21222, 2012.

[94] C.-C. Kao *et al.*, "Fabrication and performance of blue GaN-based vertical-cavity surface emitting laser employing AlN∕GaN and Ta 2 O 5∕SiO 2 distributed Bragg reflector," *Appl. Phys. Lett.*, vol. 87, no. 8, p. 81105, 2005.

[95] R.-H. Horng, W.-K. Wang, S.-Y. Huang, and D.-S. Wuu, "Effect of resonant cavity in wafer-bonded green InGaN LED with dielectric and silver mirrors," *IEEE photonics Technol. Lett.*, vol. 18, no. 3, pp. 457–459, 2006.

[96] H. J. Lee, "Techniques for fabricating Bragg reflectors on SiO 2–Si 3 N 4–SiO 2 rib waveguides on Si," *Appl. Opt.*, vol. 27, no. 6, pp. 1199–1202, 1988.

[97] H. H. Yao, C. F. Lin, H. C. Kuo, and S. C. Wang, "MOCVD growth of AlN/GaN DBR structures under various ambient conditions," *J. Cryst. Growth*, vol. 262, no. 1–4, pp. 151–156, 2004.

[98] M. Muallem, A. Palatnik, G. D. Nessim, and Y. R. Tischler, "Room temperature fabrication of dielectric bragg reflectors composed of a caf2/zns multilayered coating," *ACS Appl. Mater. Interfaces*, vol. 7, no. 1, pp. 474–481, 2014.

[99] P. Yeh, *Optical waves in layered media*, vol. 61. Wiley-Interscience, 2005.

[100] T. Kato *et al.*, "GaAs/GaAlAs surface emitting IR LED with Bragg reflector grown by MOCVD," *J. Cryst. Growth*, vol. 107, no. 1–4, pp. 832–835, 1991.

[101] J. Dai *et al.*, "Design and fabrication of UV band-pass filters based on SiO2/Si3N4 dielectric distributed bragg reflectors," *Appl. Surf. Sci.*, vol. 364, pp. 886–891, 2016.

[102] L. Zeng *et al.*, "Efficiency enhancement in Si solar cells by textured photonic crystal back reflector," *Appl. Phys. Lett.*, vol. 89, no. 11, p. 111111, 2006.

[103] M. S. K. Anuar *et al.*, "Development of SiC/MgO distributed Bragg reflector using RF magnetron sputtering technique," in *2006 IEEE International Conference on Semiconductor Electronics*, 2006, pp. 378–381.

[104] E. D. Palik and G. Ghosh, *Electronic handbook of optical constants of solids: User Guide*. Academic Press, 1999.

[105] C. Levallois *et al.*, "Design and Fabrication of GaInAsP/InP VCSEL with two a-Si/a-SiNx Bragg reflectors," *Opt. quantum Electron.*, vol. 38, no. 4–6, pp. 281–291, 2006.

[106] E. Afsharipour, P. Glowacki, and C. Shafai, "A MEMS-Controllable Fresnel Zone Plate for

Miniaturized UV Spectrometer," in *Multidisciplinary Digital Publishing Institute Proceedings, Eurosensors - European Conference on Solid-State Sensors*, vol. 1, no. 4, p.563, 2017.

[107] G. K. Fedder, "Simulation of microelectromechanical systems." Doctoral dissertation, University of California, Berkeley, 1994.